SINGLE-MODE OPERATION IN A SINGLE-LOBED BEAM PATTERN FROM SURFACE-EMITTING 2nd-ORDER DISTRIBUTED FEEDBACK LASER WITH CENTRAL π-PHSESHIFT GRATING

by

Gunawan Witjaksono

A dissertation submitted in partial fulfillment of

the requirement for the degree of

Doctor of Philosophy

(Electrical Engineering)

at the

UNIVERSITY OF WISCONSIN-MADISON

2002

UMI Number: 3060517

UMI®

ProQuest Information and Learning Company
300 North Zeeb Road
P.O. Box 1346
Ann Arbor, MI 48106-1346

A dissertation entitled

SINGLE-MODE OPERATION IN A SINGLE-LOBED BEAM PATTERN FROM SURFACE-EMITTING 2nd-ORDER DISTRIBUTED FEEDBACK LASER WITH CENTRAL π-PHSESHIFT GRATING

submitted to the Graduate School of the
University of Wisconsin-Madison
in partial fulfillment of the requirements for the
degree of Doctor of Philosophy

by

Gunawan Witjaksono

Date of Final Oral Examination: May 31, 2002

Month & Year Degree to be awarded: **December** **May** **August** 2002

****

Approval Signatures of Dissertation Committee

Signature, Dean of Graduate School

Martin Cadwallader/EH

Committee's Page. This page is not to be hand-written except for the signatures

Abstract

Surface-emitting distributed feedback (SEDFB) semiconductor lasers have been studied for almost 3 decades due to their inherent reliability, scalability and packaging advantages over edge-emitting diode lasers. However, horizontal-cavity, surface-emitting (SE) devices, incorporating a 2^{nd}-order distributed feedback grating, have been found both theoretically and experimentally to favor lasing in an antisymmetric mode (i.e. double-lobed farfield radiation pattern). Furthermore, such devices have a strongly nonuniform guided-field pattern, which inevitably makes them susceptible to multimode operation via spatial hole burning.

This dissertation presents a novel concept as well as its implementation for fundamentally obtaining symmetric-mode lasing as well as a excellent guided-field uniformity from distributed-reflector devices: the incorporation of a central phaseshift, $\Delta\phi$, of around π, in an active-DFB region surrounded by passive distributed Bragg (end) reflectors (DBRs). Theoretically, it is shown that one can fundamentally achieve a single-lobe, orthonormal surface-emitting beam with high external differential quantum efficiency and good uniformity of the guided-field profile. The investigation of these novel surface-emitting DFB devices involves the study of the threshold gains and field profiles for different values of the central phaseshift as well as for different duty-cycle values of the grating. The optimal design provides single-mode operation with a single lobed beam, with an external differential quantum efficiency in excess of 60%

A fabrication technique for 2nd-order gratings with central π-phaseshift has been developed by using interferometric photolithography (holographic system). More specifically the technique involves obtaining a central π-phaseshift by using a single photoresist via the image reversal method (i.e. side-by-side negative and positive resist).

Surface-emitting, single-mode operation with a single-lobed beam from single-element (i.e. ridge-guide) 2nd-order DFB/DBR laser has been successfully demonstrated. Thus the experimental results confirm the theoretical predictions for single-lobe operation. The effectiveness of the central grating π-phaseshift is not limited to single-element devices. This concept can be extended to array structures (in the lateral direction) to provide high-power, single-mode operation from two-dimensional surface emitters.

Acknowledgement

This thesis would not have been possible without the support and assistance of a large group of people; each of the people mentioned below contributed to my education in important ways, and I thank them all sincerely. First and foremost, I would like to thank my advisor, Professor Dan Botez for both giving me valuable help when I needed it and for allowing me the freedom necessary to try new ideas and complete work.

I also thank Prof. Luke Mawst for many insight suggestions and assistance for the crystal growths. I also thank to Dr. Jens Buus, UK, Dr. Steve Macomber, OptoPower, and Dr. Winston Chan, David Sarnoff Research Group, for valuable discussions.

I would like to thank to members of our research group; Nelson and Jaejin for the help of crystal growths, Delai, Shuang, David, Ling, Nam for discussion on the device fabrication and testing.

Finally, I would like to thank to my family for always support me even when it seemed like I would never finish. I would like to thank to my wife and best friend, Inne for caring our daughter for the long days I had to work and for always being there for me when I got home. I would like to thank my two-year-old angel, Latisha for giving me the unquestioning love and devotion only a daughter can give. I also thanks to my mother and sisters for always be there for me. You have all inspired me to succeed and I thank you.

I would like to dedicate this thesis to the memory of my loving father who passed away in my third year of graduate school. I credit al that I have achieved to his influence.

Contents

List of Figures

List of Tables

Preface

Surface-emitting devices are preferred over edge-emitting ones for generating high ($\geq$ 0.5W) CW coherent powers primarily because complete passivation of the emitting area, for reliable operation is not needed, scalability at the wafer level becomes possible, and packaging is significantly simplified. Currently, the only practical surface-emitting diode lasers are of the vertical-cavity type (so called VCSELs). Conventional (index-guided) VCSELs are useful for many applications, but are fundamentally limited to low single-mode powers ($\leq$ 7mW), which prevents their use for many applications that require high coherent powers emitted from the chip surface.

Horizontal-cavity, surface-emitting (SE) devices incorporating 2nd-order distributed-feedback (DFB) grating have been studied since the early 1970s, and invariably found both theoretically and experimentally to favor lasing in an antisymmetric mode (i.e. two-lobed beam pattern), since such a mode has the least radiation losses and subsequently it is the one favored to lase. Furthermore, such devices, due to strongly nonuniform guided-field profiles, readily becomes multimode with increasing drive above threshold via longitudinal gain spatial hole burning (GSHB).

In this dissertation a novel type of surface-emitting device is proposed. It is a composite DFB/DBRs (distributed Bragg reflectors) laser with central (grating) phaseshift of around π, which fundamentally favors lasing in a symmetric, orthonormal, single-lobe beam, over a wide range in central-phaseshift values, at *no penalty* in device efficiency. External differential quantum efficiencies in excess of 60% can be obtained, and the guided-field profile is substantially uniform, thus insuring single-mode operation to potentially high-power levels: $\geq$ 200mW CW from single-element (e.g. ridge-guide) devices, and $\geq$ 2W CW from parallel-coupled phase-locked arrays (in the lateral dimension).

The dissertation is organized as follows: Chapter 1 presents a brief history of horizontal-cavity surface emitters and the potential applications of surface-emitting lasers, which provide the motivation for pursuing surface-emitting (SE) distributed feedback devices. The goals of the research are presented and the achievements are described. Chapter 2 describes the fundamentals of distributed-feedback and conventional surface-emitting DFB lasing. Chapter 3 discusses the theoretical approaches developed for device simulation of surface-emitting, 2^{nd}-order DFB lasers. The theoretical models include the use of the coupled-mode theory and the transfer-matrix. Chapter 4 describes the simulation results obtained from the theoretical analysis of the proposed surface emitter. The simulation results ultimately show how the novel design proposed fundamentally provides single-mode operation in a single lobed beam pattern at no penalty in device efficiency. Due to the high intermodal discrimination as well as the uniformity of the guided-field profile, single-mode operation can be achieved to high power levels. Chapter 5 outlines the fabrication method to pattern 2^{nd}-order gratings with central π-phaseshift. Chapter 6 discusses the fabrication of single-element (i.e. ridge-guide) 2^{nd}-order DFB surface emitters and presents the experimental results. Finally, Chapter 7 presents concluding remarks and plans for future work. The appendices discuss in detail the fabrication steps to obtained central π-phaseshifted gratings, single-element (i.e. ridge guide) surface-emitting distributed feedback lasers, and the MathCad code for device simulation.

Chapter 1

INTRODUCTION

This dissertation describes a theoretical study and the experimental demonstration of obtaining single-mode operation with single-lobed beam pattern from surface-emitting (SE) second-order distributed feedback lasers. The work involves a novel feature: central π-phaseshift grating; for fundamentally obataining single-mode surface emission in an orthonormal beam, which is single-lobed at no penalty in the efficiency. This invention opens the way for the realization of two-dimensional surface-emitters with potential for providing output power greater than 2W CW in a stable, single-lobed beam.

1.1 Overview

Currently, the only practical surface-emitting diode lasers are of the vertical-cavity type (so called VCSELs). VCSELs are quite useful for many applications, but are fundamentally limited to low single-mode powers (< 7mW) [1], which prevents their use for many new exciting upcoming applications that require high coherent powers (> 500 mW) emitted from the chip surface.

The other major means for obtaining single-mode surface emission is a distributed feedback (DFB) laser with a 2^{nd}-order grating. There is steadily increasing motivation to realize distributed feedback (DFB) lasers which emit light from their surface, for the following reasons: a) significantly improved reliability, since distributing the emitting power output over a large area reduces the power density at the emission aperture, as well as avoids emission from cleaved facets, which are known to limit the reliability of edge emitters; b) an increased 2-D emission area can give narrow beams in both dimensions, which will be useful for applications such as free-space optical communications; c) surface emitters can readily be arranged in two-dimensional arrays which could be useful for optical-data switching and processing: and d) scalability at the wafer level could provide ten of watts of coherent power.

1.2 Horizontal-Cavity, Surface-Emitting 2^{nd}-Order DFB lasers

The realization of coherent CW watt-range, stable, single-mode sources will, for the first time, enable exciting developments such as: room-temperature CW mid-IR (λ = 3-5 μm) coherent-light generation (via frequency downconversion) for a vast array of noninvasive medical diagnostics (e.g. breath analysis and fluid analysis), and for IR countermeasures; the generation of hundreds of mWs of blue light via harmonic conversion for many applications in biotechnology (e.g. flow cytometry) and for laser-projection systems: high-power low-noise, high-fidelity RF optical links; and coherent, free-space optical communications.

Due to their potential for producing high coherent powers, surface-emitting, second-order DFB lasers have been studied for the last 3 decades. The first conventional DFB laser was proposed and analyzed by Kogelnik and Shank using the coupled-wave theory in 1972 [2]. The theory followed the first demonstrations of laser action from periodic structures [3,4]. The first demonstration of surface-emitting lasing from periodic structures was realized by Zory [5], followed shortly by theory predicting such behavior [6]. The first DFB semiconductor laser operating at room temperature in the continuous wave (CW) mode was built in 1975 [7], but not until the mid 1980's were surface-emitting, distributed-feedback semiconductor lasers demonstrated [8-11]. However, conventional devices inherently prefer oscillation in an antisymmetric mode (i.e. two-lobe pattern and highly nonuniform guided-field pattern), which, in turn it is not only impractical, but also favors easy excitation of high-order modes via gain spatial hole burning (GSHB). Therefore, although SEDFB lasers have been studied for almost 3 decades, conventional surface-emitting (SE) second-order distributed feedback devices have proven unusable.

1.3 Previous Work for Single-Lobed Operation

The lasing mode preferred in index-coupled surface-emitting (SE) DFB lasers is the antisymmetric mode (A). This mode has a nonuniform guided-field profile and its farfield pattern has a double-lobed beam pattern, which makes this device unreliable and impractical. Several methods for obtaining single-lobed farfield patterns from index-coupled SEDFB lasers have been proposed.

The first method utilized a π-phase-shifting film on one half of the aperture [12]. The phase profile became uniform along the grating and the farfield was then a single-lobed beam. However, this was not a monolithic device and did not solve the guided-field nonuniformity problem. The second method, which has been experimentally demonstrated, was to selectively pump the grating region [13]. The wavelength of the symmetric mode was made to coincide with the maximum reflectivity of the passive-DBR reflectors; thereby making it favored to lase. However, this device used a low coupling coefficient and its operation depended on the injected carriers, which made it potentially unreliable. Moreover, the low coupling coefficient gave a low efficiency. The third method involved chirping the grating, a technique that demonstrated good results, but produces an off-normal farfield profile [14].

Another method, that was proposed in UW-Madison, was to use absorption loss in the grating (i.e. complex-coupled 2^{nd}-order DFB grating) [15]. The reason the antisymmetric mode is favored for index-coupled DFB lasers is that the amount of surface radiation of this mode is lower than for the symmetric mode (S). By periodically placing absorption loss in the grating, it has been shown that the antisymmetric mode can experience more loss than the symmetric mode [15]. By designing the absorptive grating, so that the difference in absorption loss between modes A and S is larger than the difference in their radiation losses, the symmetric mode is fundamentally favored to lase. However the metal grating used in this approach absorbs a significant amount of light, which causes the device to have relatively low efficiencies ($\leq$ 25%).

All the aforementioned approaches for obtaining the single-lobed farfield have thus proven either unreliable or impractical.

1.4 Research Goals and Achievements

An asymmetrically coated SEDFB laser with Au/air grating has been shown to produce a single DFB longitudinal mode as well as single-lobe operation [16]. However the resulting longitudinal guided-field pattern was still nonuniform. The output power and the efficiency were too small to measure. Furthermore the phaseshift at the both ends of grating cannot be controlled because of the random nature involved in the mirror-facet cleaving.

The purpose of this study has been to design, analyze, and implement a SEDFB laser using a novel technique for achieving single-mode surface emission in a beam, which is single-lobed and normal to the chip surface, with no penalty in the efficiency. The results achieved are summarized below:

- Designed and analyzed a surface-emitter with central phaseshift grating. Devices with central π-phaseshift grating in the active-DFB region, passive-DBR reflectors and AR coatings at the ends were found to provide a single-lobe farfield pattern with high differential external quantum efficiency (in excess of 60%), a uniform guided-field profile as well as relatively low gain threshold values (22 cm^{-1}) [17-19].
- Developed and fabricated a GaAs second-order grating with central π-phaseshift using interferometric lithography (holographic system) by employing the image reversal method. [19]
- Developed the new surface-emitting, single-lobe devices based on Au/GaAs grating with central π-phaseshift, distributed end reflectors and a ridge guide for lateral mode control. The novel concept was successfully demonstrated. [20,21]

1.5 Proposed Structure

Fig. 1.1 schematically depicts the longitudinal cross section of the proposed 2^{nd}-order grating surface-emitting device. Antireflection (AR) coatings are assumed at the ends of the passive (i.e. DBR) sections. The device has an Al-free structure, which allows for easy preferential etching and regrowth needed for structures with advanced means for lateral-mode control. The structure has a GaAs buffer layer, followed by an n-doped 1μm-thick n-InGaP-cladding layer and a 100nm-thick InGaAsP lower optical-confinement layer. Two 7nm-thick InGaAs quantum wells separated by a 20nm-thick InGaAsP(1.6eV) barrier layer form the active region. Next are: a 100nm-thick InGaAsP upper optical-confinement layer, a 300nm-thick p-InGaP cladding layer, and a p^+-GaAs grating layer of 3000Å period and incorporating a central phaseshift, $\Delta\phi$. SiO_2 is then deposited and etched to create the DBR regions. Such fabrication reduces any phase differences at the interfaces between the active (i.e. DFB) and the passive (i.e. DBR) regions. Au is then deposited by e-beam evaporation to form electrical contact to the DFB region. The GaAs/Au grating not only provides high coupling coefficient, κ, but also insures that all first-order diffracted light is collected. Absorbing InGaAs regions can then be regrown (not shown) at the ends of the DBR regions, to insure virtually zero reflections. The light is emitted through a window in the n-side metallization of the GaAs substrate.

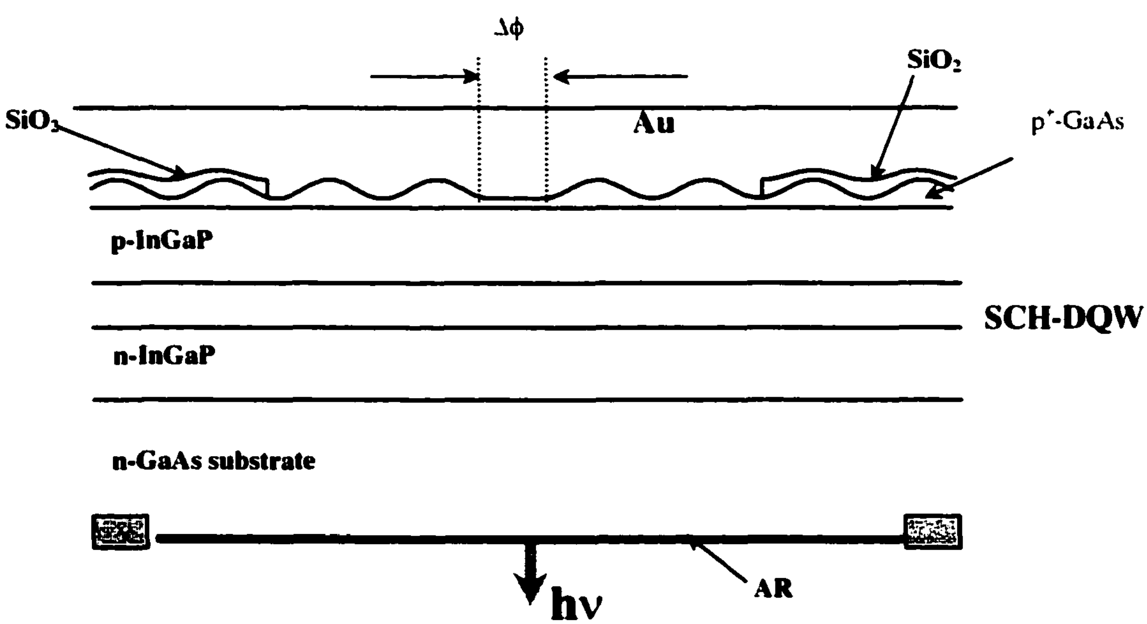

Fig. 1.1 The cross view section of the surface-emitting 2^{nd}-order DFB laser with central grating phaseshift.

Chapter 1 References

[1] D. Zhou, PhD dissertation, Electrical and Computer Engineering, University of Wisconsin – Madison, March 2002.

[2] H. Kogelnik and C.V. Shank, "Coupled-Wave Theory of Distributred Feedback Lasers," J. Appl. Phys. **43** (5), 2327 (1972).

[3] H. Kogelnik and C.V. Shank, "Stimulated Emission in Periodic Structures," Appl. Phys. Lett. **18**, 152 (1971).

[4] C.V. Shank, J.E. Bjorkholm, and H. Kogelnik, "Tunable Distributed-Feedback Dye Laser," Appl. Phys. Lett. **18**, 395 (1971).

[5] P. Zory, Technical Digest Topical Meeting on Integrated Optics-Guided Waves, Materials, and Devices, Las Vegas, Nevada, 7-10 February 1972, Paper ThA2

[6] R.F. Kazarinov and R.A. Suris, Surf. Sci. 6, 1189 (1973).

[7] H.C. Casey, S. Somekh, and M. Ilegems,"Room Temperature Operation of Low-Threshold Separate Confinement Distributed Feedback Lasers," Appl. Phys. Lett. **27**, 142 (1975).

[8] C. H. Henry, R.F. Kazarinov, R.A. Logan, R. Yen, "Observation of destructive interference in the radiation loss of second-order distributed feedback lasers," IEEE J. Quantum Electron. **QE-21**, 151 (1985).

[9] K. Mitsunaga, M. Kameya, K. Kojima, S. Noda, K. Kyuma, K. Hamanaka, and T. Nakayama, "CW surface-emitting grating coupled GaAs/AlGaAs distributed Feedback Lasers with narrow beam divergence", Appl. Phys. Lett. **50**, 1788 (1987).

[10] S.H. Macomber, J.S. Mott, R.J. Noll, G.M. Gallatin, E.J. Gratix, S.L. O'Dwyer, and S. A. Lambert, "Surface-Emitting Distributed Feedback Semiconductor Laser," Appl. Phys. Lett. **51**, 472 (1987).

[11] S.H. Macomber, J.S. Mott, R.J. Noll, G.M. Gallatin, E.J. Gratix, S.L. O'Dwyer, and S. A. Lambert, "AlGaAs Surface-Emitting Distributed Feedback Laser," Proc. SPIE vol. **893**, 188 (1988).

[12] S.H. Macomber, J.S. Mott, H.F. Chung, and T.L. Parli, "Recent Development in Surface Emitting Distributed Feedback Arrays," Proc. SPIE **1219**, 228 (1990).

[13] N.W. Carlson, S.K. Liew, R. Amantea, D.P. Bour, G.A. Evans, and E.A.Vangieson, "Mode discrimination in Distributed Feedback Grating Surface Emitting Lasers Containing a Buried Second-Order Grating," IEEE J. of Quantum Electron. **27** (6), 1746 (1991).

[14] S.H. Macomber, "Nonlinear Analysis of Surface-Emitting Distributed Feedback Lasers," IEEE J. of Quantum Electron. **26** (12), 2065 (1990).

[15] M. Kasraian and D. Botez, "Metal-Grating-Outcoupled, Surface-emitting, Distributed-Feedback Lasers," Appl. Phys. Lett. **69** (19), 2795 (1996).

[16] J. Lopez, G. Witjaksono, and D. Botez, "Single-Mode, Single-Lobe Operation of Surface-Emitting, Second-Order Distributed Feedback Lasers," Appl. Phys. Lett, **75** (7), 885 (1999).

[17] G. Witjaksono and D. Botez, "Surface-Emitting, Single-Lobe Operation from 2nd-order DFB/DBR Lasers with Central Grating Phaseshift," Proc. 2000 IEEE 17th ISLC, 35 (2000).

[18] G. Witjaksono and D. Botez, "Surface-Emitting, Single-Lobe Operation from 2nd-Order Distributed-Reflector Lasers with Central Grating Phaseshift," *Appl. Phys. Lett.*, **78**, 4088-4090 (2001)

[19] G. Witjaksono, S. Li, and D. Botez, "High-efficiency, Single-lobe Surface-Emitting DFB/DBR Lasers", Paper TuA3 at the 14th IEEE LEOS Annual Meeting, 12-15 Nov. 2001, San Diego, CA.

[20] G. Witjaksono, S. Li and D. Botez, "Single-Mode Operation Single-Lobed Beam from 2nd-Order Distributed-Reflector Lasers with Central Grating Phaseshift," *Appl. Phys. Lett.*, in progress (2002)

[21] G. Witjaksono, S. Li and D. Botez, "Single-lobe, Orthonormal-Beam Surface Emission from 2nd-order DFB/DBR Lasers with Half-Wave Grating Phaseshift," *submitted* to IEEE 18th International Semiconductor Laser Conference, Germany (2002)

Chapter 2

Fundamentals of Distributed Feedback (DFB) Lasing

Distributed feedback lasers have been the focus of interest in the research and practical applications due to their frequency-selection capability. This chapter outlines the background on the distributed feedback mechanisms and a technique to break degeneracy in edge-emitter DFB lasers. Then the fundamentals of surface emission from second-order distributed-feedback devices are discussed. For horizontal-cavity surface emitters, coherence is obtained along the longitudinal direction by using a 2nd-order grating with a DFB region for gain, partial feedback and outcoupling: and DBR regions for strong frequency-selective feedback (Fig.2.1).

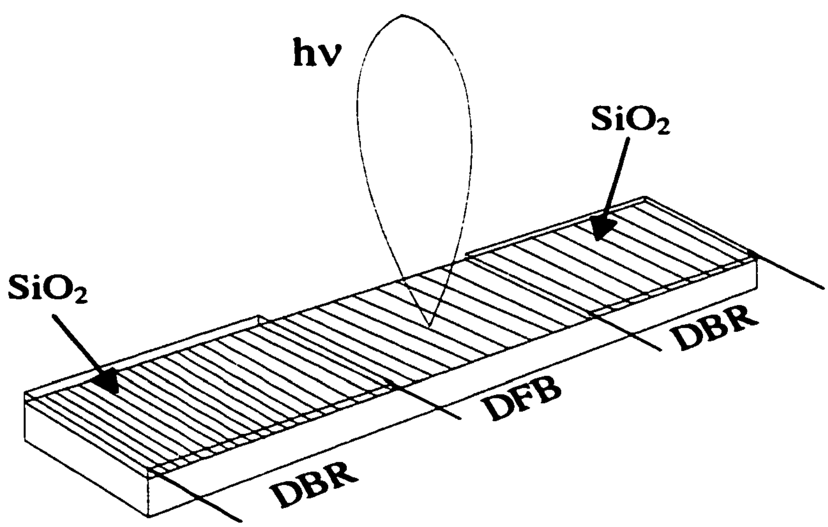

Fig 2.1. Schematic representation of surface-emitting DFB/DBR device operating in a single, orthonormal beam due to a half-wave (i.e. π) central grating phaseshift (not shown).

2.1 Distributed Feedback (DFB) mechanism.

A very high degree of wavelength selectivity can be achieved by incorporating a periodic structure into the semiconductor laser body. For index-coupled DFB lasers, the feedback necessary for laser operation is provided by reflections at periodic refractive-index variations along the laser cavity.

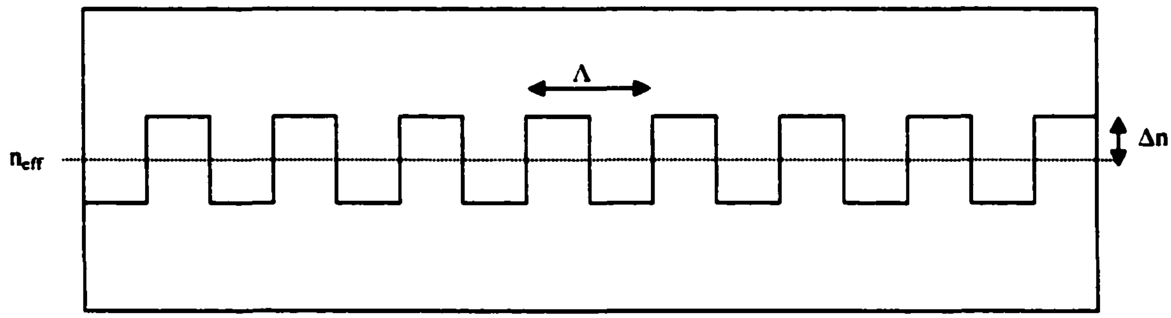

Fig 2.2 Periodic refractive-index variation along the laser cavity.

The refractive index depends on the position, in the longitudinal direction, as such:

$$n(z) = n_{eff} \pm \Delta n \cos(2\beta_o z) \tag{2.1}$$

where βo is the Bragg propagation constant given by

$$\beta_o = k_o n_{eff} = \frac{2\pi}{\lambda_o} n_{eff} = \frac{M\pi}{\Lambda} \tag{2.2}$$

where Λ is the period of the periodic structure, and M is the grating order. The value of M is 1 for a 1^{st}-order grating.

For a lateral structure supporting only one spatial mode, selective feedback in one longitudinal mode can be provided by the periodic variation of the refractive index along the optical waveguide. The longitudinal field in this periodic structure consists of two counter propagating waves R(z) and S(z) as shown in Fig. 2.3. The two waves continuously feed energy into one another through Bragg scattering, and the field amplitudes of R(z) and S(z) are thus coupled to each other. Specifically these propagating waves, R(z) and S(z), are related by the following coupled-mode equations [1]:

$$\frac{dR(z)}{dz} - (\alpha_o - j\delta)R(z) = -j\kappa S(z) \tag{2.3}$$

$$\frac{dS(z)}{dz} + (\alpha_o - j\delta)S(z) = j\kappa R(z) \tag{2.4}$$

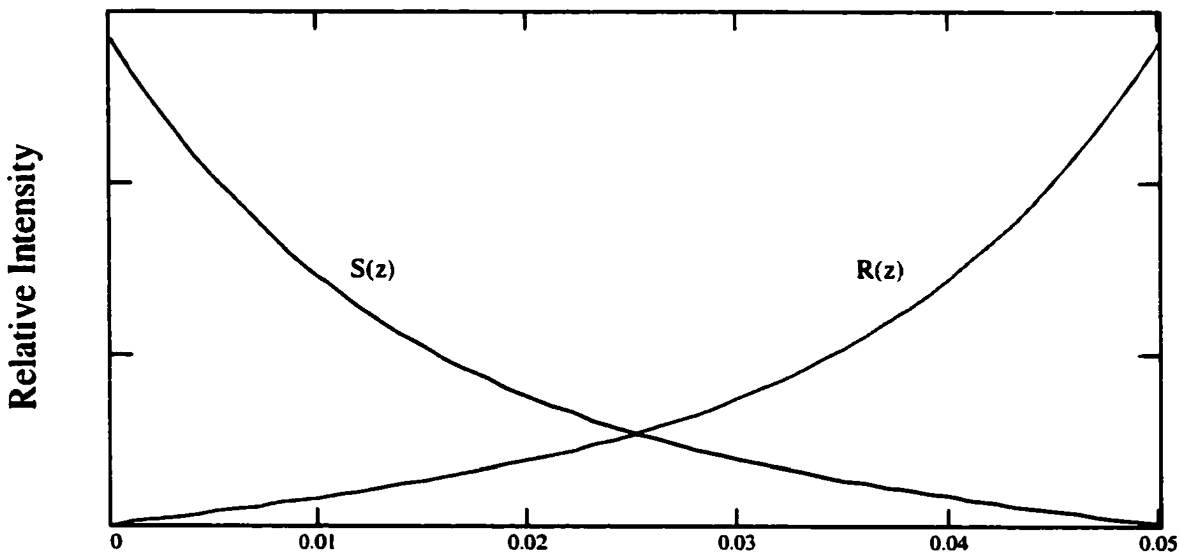

Fig 2.3. The right- and left-going wave, R(z) and S(z).

where κ is the coupling coefficient, which characterizes the coupling between the amplitude for the right propagating wave R(z) and the left propagating wave S(z). The term δ is the deviation of the real part of the propagation constant from the Bragg condition, and α_0 is the gain for the optical field.

$$\beta = \beta_o + (\delta + j\alpha_o) \tag{2.5}$$

Equations (2.3) and (2.4) are a set of linear, coupled first-order differential equations. The most general solution is given by:

$$R(z) = r_1 \exp(\gamma z) + r_2 \exp(-\gamma z) \tag{2.6}$$

$$S(z) = s_1 exp(\gamma z) + s_2 exp(-\gamma z) \tag{2.7}$$

Substituting Eqs. (2.6) and (2.7) back into Eqs. (2.3) and (2.4), one finds that in order to have nontrivial solutions, one must satisfy the condition:

$$\gamma^2 = \kappa^2 + (\alpha_o - j\delta)^2 \tag{2.8}$$

Boundary conditions are needed in order to solve these coupled-mode equations (i.e. Eqs. (2.3) and (2.4)). In most cases it is assumed that antireflection coatings are placed at each end of the structure. So one takes a structure of length L, extending from z= -L/2 to z=L/2, with zero reflectivity at the ends. Since there are no fields propagating into the periodic structure one has:

$$R(-L/2) = S(L/2) = 0 \tag{2.9}$$

giving:

$$\frac{r_1}{r_2} = \frac{s_2}{s_1} = -\exp(\gamma L) \tag{2.10}$$

The resulting field must be either symmetric or antisymmetric, hence;

$$r_1 = \pm s_2, r_2 = \pm s_1 \tag{2.11}$$

The field distribution is then given by:

$$R(z) = \sinh \gamma(z + L/2) \tag{2.12}$$

$$S(z) = \pm \sinh \gamma(z - L/2) \tag{2.13}$$

The characteristic equation can be found by inserting Eqs. (2.12) and (2.13) into Eq. (2.3):

$$\kappa = \frac{\pm\gamma}{\sinh(\gamma L)} \tag{2.14}$$

which can also be written, using Eq, (2.8).

$$(\alpha_o - j\gamma) = j\coth(\gamma L) \tag{2.15}$$

For a given length L and coupling coefficient κ there exists a discrete set of eigenvalues γ, which corresponds to longitudinal modes with the threshold (field) gain given by α_0 and the wavelength determined by the value of δ.

The required gain for DFB laser action ($g_{th} = 2\,\alpha_o$) is equivalent to the mirror losses for Fabry-Perot lasers ($g_{th} = \alpha_{end}$), assuming that there is no internal loss. The solutions of Eqs. (2.14) and (2.15) can only be solved using numerical methods.

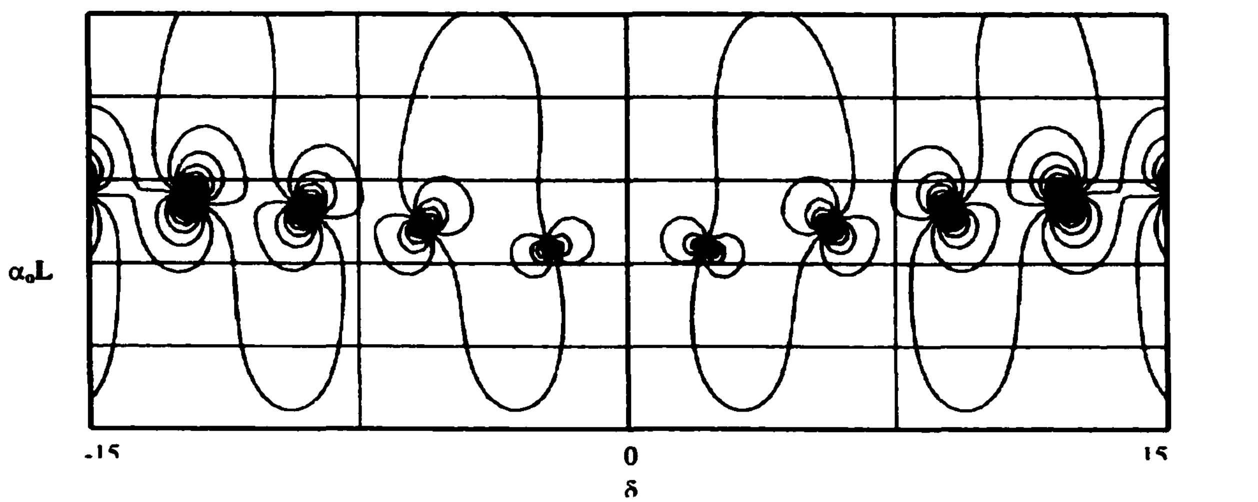

Fig 2.4. The eigenvalue solutions for IC-DFB lasers.

Fig. 2.4 shows that there is no solution at δ=0 for the IC-DFB lasers. Note that there is spacing between the two modes of lowest gain. The spacing region is called the *stop band*, and it has a width of $2\kappa L$ for large values of κL. The appearance of two modes with the same lowest field gain means the existence of two degenerate modes; hence, single-mode operation is not possible. This characteristic is undesirable, but there are various approaches to break this degeneracy: complex-coupled DFB and quarter-wave shifted DFB lasers.

2.2 Complex-Coupled DFB (CC-DFB) Lasers

If both the index of refraction and the gain vary periodically in the longitudinal direction of a semiconductor laser cavity, the structures are known as complex-coupled distributed feedback (CC-DFB) lasers. They differ from standard (index-coupled) DFB lasers by their extra gain coupling, which is achieved either by introducing a loss or a gain grating. However, instabilities due to saturable absorption can occur for loss grating devices. [2] The coupling coefficient, κ, for complex-coupled DFB can be written as:

$$\kappa = \kappa_{index} + j\kappa_{gain} \tag{2.16}$$

where κ_{index} and κ_{gain} are real numbers describing the coupling strength of the index and gain grating, respectively. This is the case where both the index of refraction and the gain vary periodically in the longitudinal direction of the semiconductor laser cavity.

In complex-coupled DFB lasers, each mode experiences a different gain due to their difference in field distribution. The side modes have a different field distribution than the lasing mode, and hence do not see the gain as effectively as the lasing mode. This effect results in a gain difference between modes, so the degeneracy is removed. A typical mode spectrum for gain-coupled DFBs is shown in Fig. 2.5.

In devices with mixed index and gain coupling, a significant improvement occurs in term of reduced spatial hole burning and increased threshold gain difference as compared to index-coupled DFB lasers [3,4]

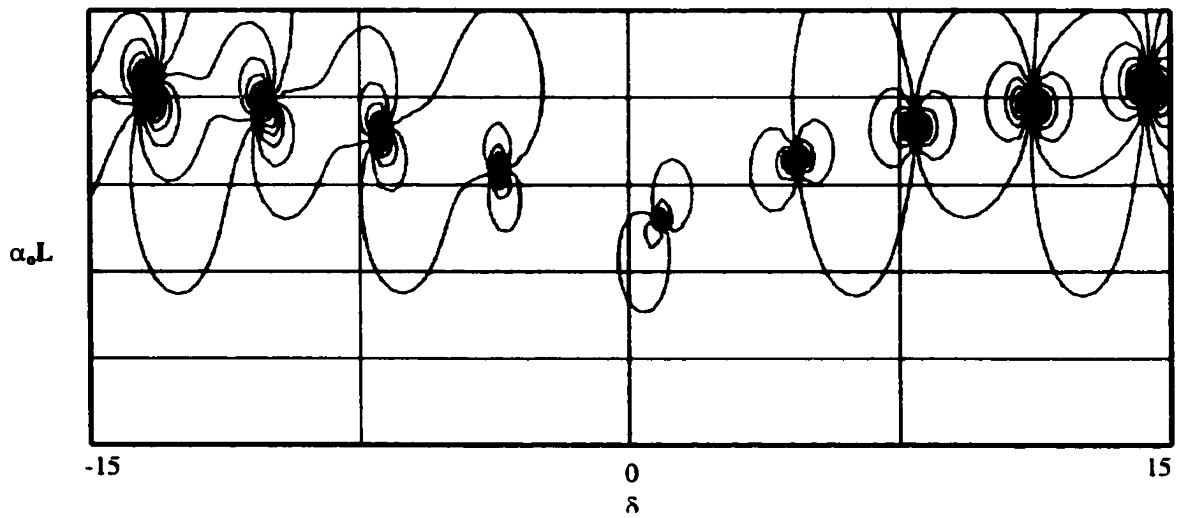

Fig 2.5. The eigenvalue solutions for CC-DFB lasers.

2.3 Quarter-wave ($\lambda/4$) Shifted DFB Laser

There is another way to obtain single-mode operation for a 1st-order DFB laser. The solution is to insert an extra phaseshift in the center of the periodic structure. Figs. 2.6a and b show the grating with no phaseshift and with the phaseshift, respectively.

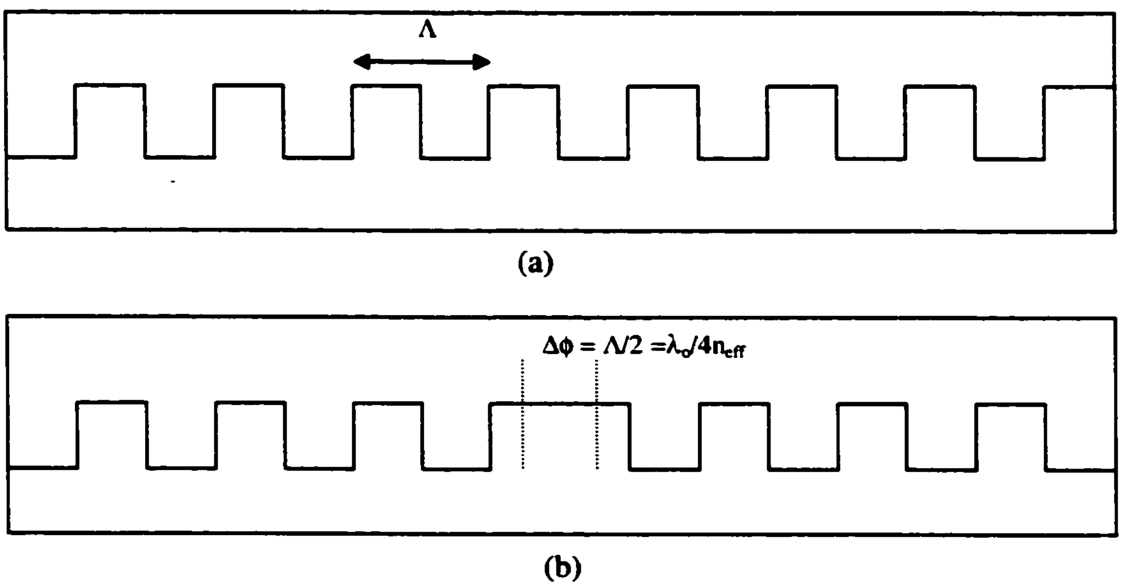

Fig. 2.6. First-order grating structure: (a) without phaseshift; (b) with quarter-wave phaseshift.

If the length of the phaseshift is half of the grating period ($\frac{\Lambda}{2} = \frac{\lambda_o}{4n_{eff}}$), corresponding to an extra phaseshift of $\pi/2$, all the reflected waves will interfere constructively and the total round-trip phase will be multiple of 2π [5]. The solution from the eigenvalues (Fig. 2.7) now has a single dominating mode, of the lowest threshold gain, at δ=0.

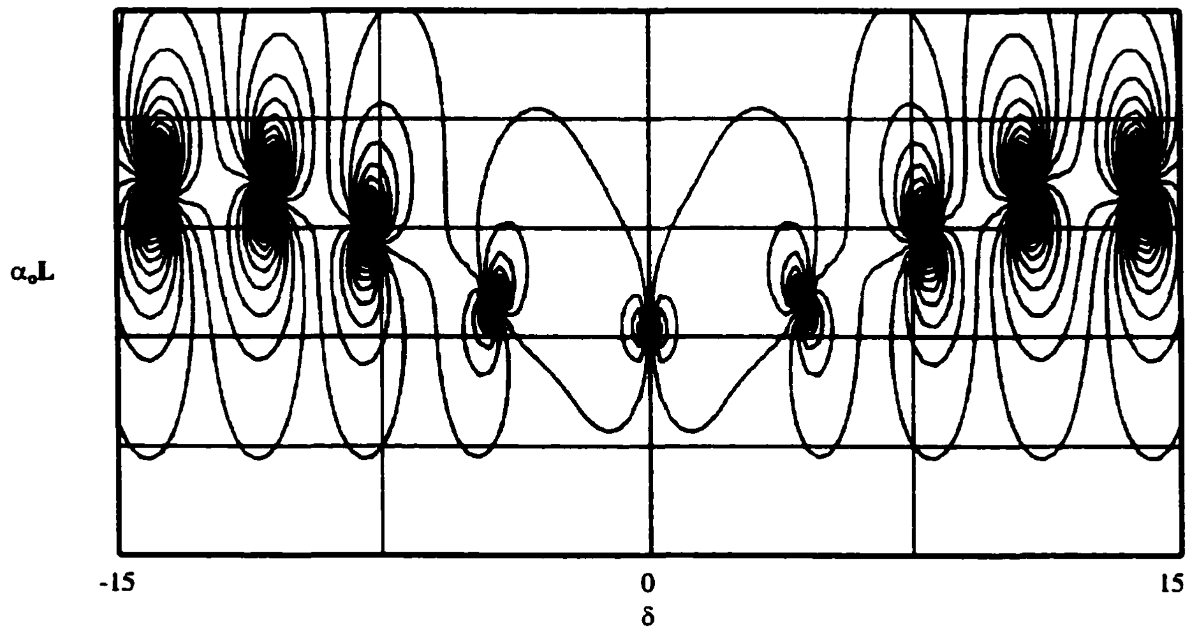

Fig 2.7. The eigenvalue solutions for the quarter-wave shifted DFB lasers.

However, the quarter-wave phaseshift devices have a highly longitudinally nonuniform field-intensity pattern, which limits their single-mode pwers to values below 10 mW.

2.4 Surface-Emitting DFB (SEDFB) Lasers

Figure 2.8 illustrates the conventional reflective diffraction of a plane wave from a periodic grating structure with elements spaced at a period Λ [6]. A plane incoming wave is incident at an angle θ_i, and the Mth-order diffracted plane wave emerges at the angle θ_d.

Constructive interference between the diffracted waves emanating from adjacent elements of the grating requires the condition:

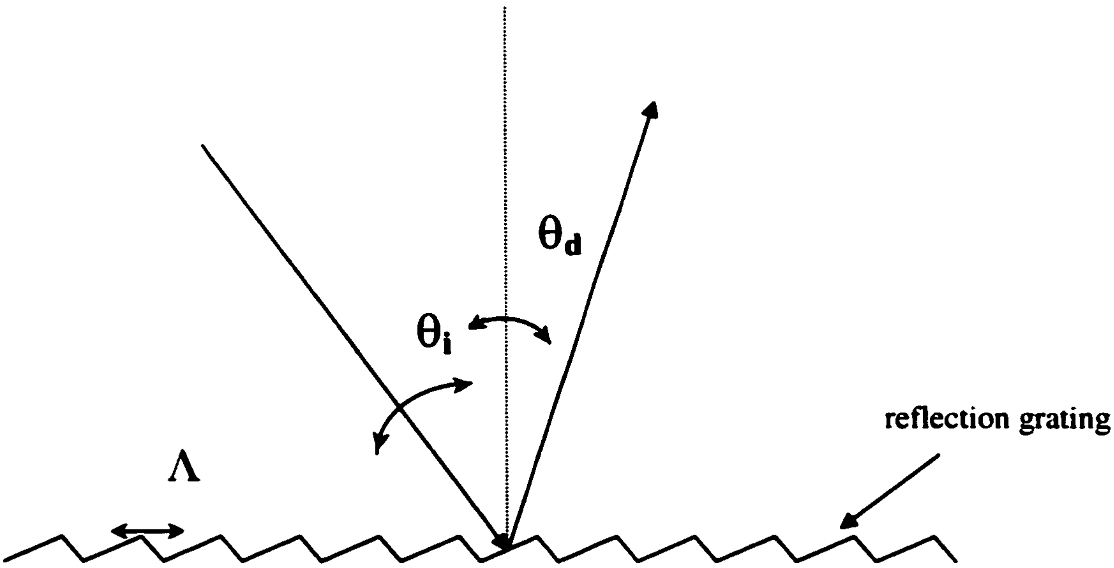

Fig 2.8 A reflective diffraction from a periodic grating. θ_i is an angle of incidence; θ_d is an angle of diffraction; and Λ is grating period.

$$\Lambda(\sin(\theta_i)-\sin(\theta_d))=p\lambda \tag{1.17}$$

The integers p = 0, ±1, ±2, ... define the order of the diffraction or the phase shift on wavelengths between the diffracted waves from adjacent grating elements, and λ is the radiated wavelength. When the refractive indices are different for the two media, the media wavelengths are also different. Huygens' construction for constructive interference from identical points but at different periods of the grating requires that the sum (or difference) of the total optical path in radians to be integer multiple of 2π. In terms of distances and the wavelengths appropriate to different material as in the Fig. 2.9.

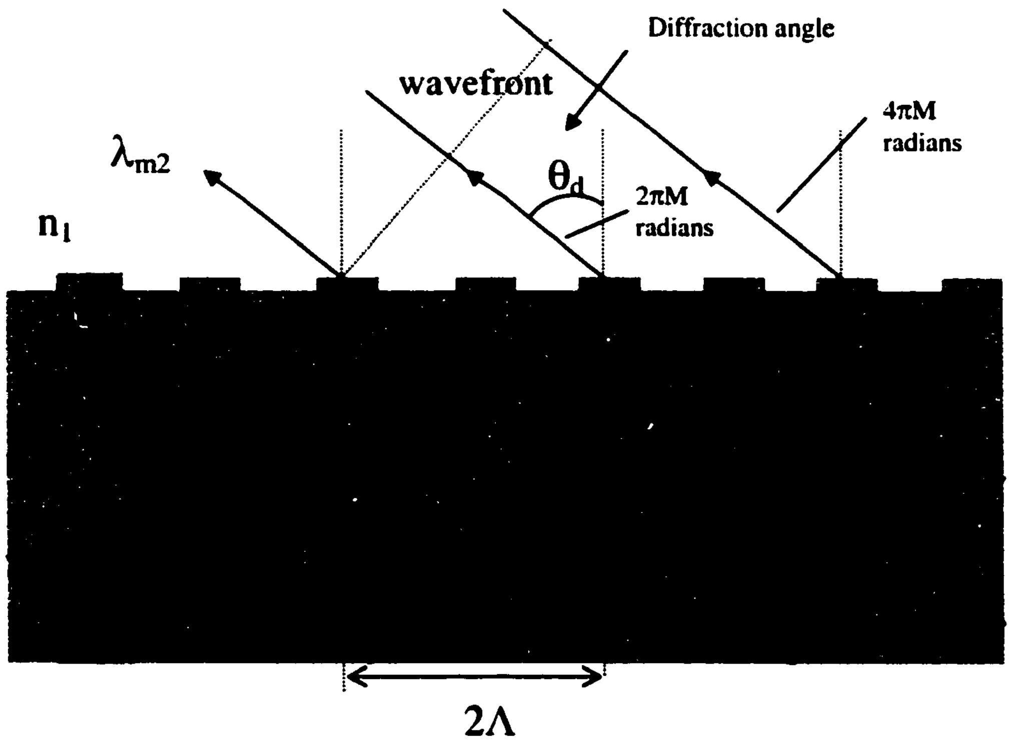

Fig. 2.9. Diffraction from a periodic grating embedded in laser waveguide.

The required constructive interference is then:

$$\frac{\Lambda \sin\theta_i}{\lambda_{m1}} + \frac{\Lambda \sin\theta_d}{\lambda_{m2}} = p \qquad (2.18)$$

On applying the results of Eq. (1.18) to a propagating optical mode in the DFB laser waveguide shows that the angle of incidence, θ_i cannot be less than the critical angle for total internal reflection θ_c, so that:

$$\sin\theta_i \geq \sin\theta_c = \frac{n_2}{n_1} = \frac{\lambda_{m1}}{\lambda_{m2}} \qquad (2.19)$$

Inserting Eq. (2.19) into Eq. (2.18)

$$\sin\theta_d \geq (\frac{\lambda_{m2} p}{\Lambda} - 1) \approx (\frac{2p}{M} - 1) \qquad (2.20)$$

where the integer $M = \Lambda/(\lambda_m/2)$ defines the grating order. Given a physical periodicity Λ of the grating, the optimum free-space wavelength λ_b, which is most strongly reflected, is called the Bragg wavelength and satisfies the Bragg condition;

$$p(\frac{\lambda_b}{n_{eff}}) = 2\Lambda \tag{2.21}$$

where n_{eff} is the mean value of the refractive index in the guide and relates the free-space Bragg wavelength λ_b with the corresponding guide wavelength $\lambda_m = \lambda_b/n_{eff}$.

Table 2.1 summarizes the influence of the grating order M and diffracted order p on the feedback and radiation loss experienced by the propagating mode.

Table 2.1. Summary of feedback and radiation wave from the DFB structure [6].

Order of diffraction	p = 0	p = 1	p = 2
First-order grating, M = 1	Feed-forward	Feedback	
Second-order grating, M = 2	Feed-forward	Radiation	Feedback

The second-order grating, where M = 2, has a diffracted wave which is emitted in a direction normal to the surface. This diffracted wave, which is first-order diffraction, can be used to outcouple the light from the laser out into a direction perpendicular to the junction, to form a surface-emitting laser. The period of the index and a gain variations equals the wavelength of light in the active medium ($\Lambda = \frac{\lambda_b}{n_{eff}}$), for a 2nd-order grating. The counter-propagating waves $R(z)$ and $S(z)$ are the results of the 0th-and 2nd-order diffractions. Fig. 2.10 shows the diffraction-order waves for a 2nd-order DFB structure.

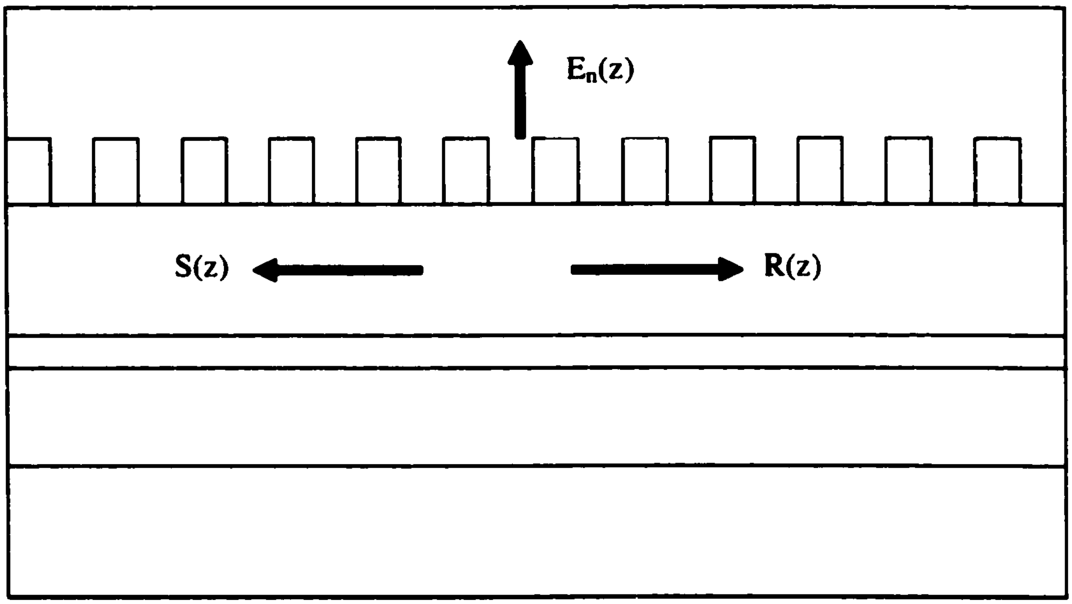

Fig 2.10. Feedback and radiation waves for 2nd –order DFB structure. $E_n(z)$ is outcoupled radiation wave resulting form 1st-order diffraction. S(z) and R(z) are counter-propagating waves resulting form 2nd-order diffraction.

2.5 Conventional Surface-Emitting 2nd-order DFB (SEDFB) Lasers

For index-coupled, surface-emitting DFB lasers, it has been found both theoretically and experimentally that the mode of least radiation loss (i.e. output) and thus the one favored to lase is invariably an antisymmetric mode having a nonuniform guided-field profile. The radiated near-field pattern of the antisymmetric mode has a null at the center and peaks at the ends of the structure as shown in Fig. 2.11. The guided-field intensity profile is depicted in Fig. 2.12. Such a device invites multimoding via gain spatial hole burning because of a nonuniform guided-field profile. The farfield of the antisymmetric mode is a double-lobed with each lobe being off normal with respect to the plane of the surface.

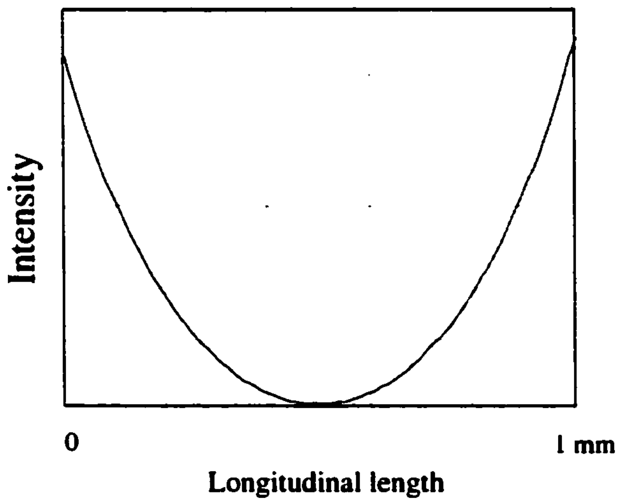

Fig. 2.11. The antisymmetric (A) mode near-field intensity profile.

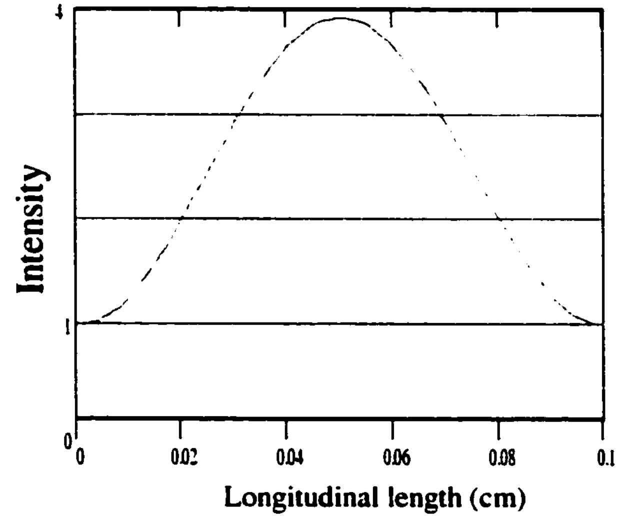

Fig. 2.12. The guided-field intensity profile.

Fig. 2.13 depicts the near-field intensity profile of the desired mode; the symmetric (S) mode. The far-field pattern of the symmetric mode is single-lobed and normal to the surface.

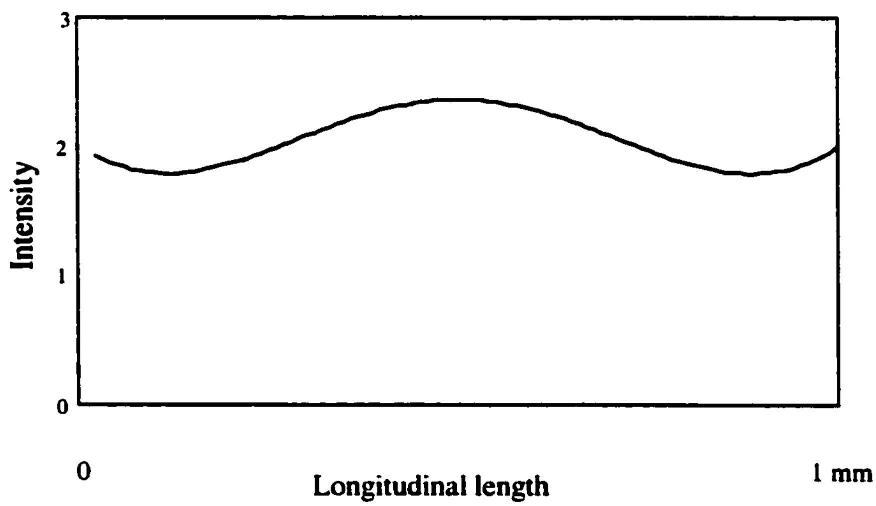

Fig. 2.13. The symmetric mode (S) near-field intensity profile.

Chapter 2 References

[1] H. Kogelnik and C.V. Shank, "Coupled-Wave Theory of Distributred Feedback Lasers," J. Appl. Phys. **43** (5), 2327 (1972).

[2] J. Zoz, B. Borchert, "Dynamic Behaviour of Complex-Coupled Distributed Feedback Lasers with In-phase absorptive Grating," Electron. Lett. **30** (1), 39 (1994).

[3] E. Kapon, A. Hardy, A. Katzir, "The Effect of Complex-Coupling Coefficient on Distributed Feedback Lasers," IEEE Journal of Quantum Electronics, **QE-18** (1), 66 (1982).

[4] G. Morthier, P. Vankwikelberge, K. David, and R. Baets,"Improved Performance of AR-Coated DFB Lasers by the Introduction of Gain Coupling," IEEE Photon. Tech. Lett. **2** (3), 170 (1990).

[5] Jens Buss, "Single Frequency Semiconductor Lasers," Published by SPIE - International Society for Optical Engineering, WA (1991).

[6] J. Carrol, J. Whiteway, D. Plumb, "Distributed Feedback Semiconducctor Lasers," Published by SPIE - The International Society for Optical Engineering, UK (1998).

Chapter 3

Horizontal-Cavity Surface-Emitting 2nd-order Distributed Feedback Lasers

Our previous work to obtain a single-lobed beam using a metal grating (Fig 3.1), while feasible, introduces too much of a penalty loss for mode, such that efficiencies are at best 20% and the gain threshold is quite high (~ 70 cm^{-1}).[1]

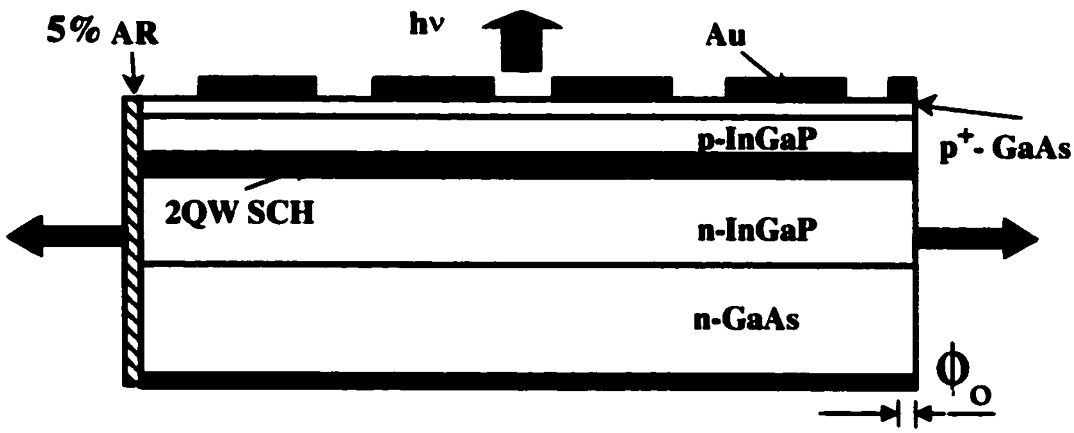

Fig. 3.1 Asymmetrically facet-coated surface-emitting DFB laser structure with Au/Air grating

.

This dissertation explores a novel technique: incorporation of a central phasehift; which introduces no penalty in the efficiency to obtain single-mode operation with a single-lobed beam pattern, relatively low threshold gain, and high efficiencies.[2]

3.1 Modeling Methods

3.1.1 Coupled-mode theory

In order to design, optimize and analyze the 2nd-order DFB structure, a numerical method, which computes the complex coupling coefficient of conventional and gain-coupled

DFBs, was adopted. This method solves for the two-dimensional electric field E(x,z) and was originally developed by Noll and Macomber [3]. Fig. 3.2 shows the SEDFB structure with its feedback and radiated waves. To find E(x,z) one must solve the wave equation:

$$\nabla^2 E(x,z) + k^2 \varepsilon(x,z) E(x,z) = 0 \tag{3.1}$$

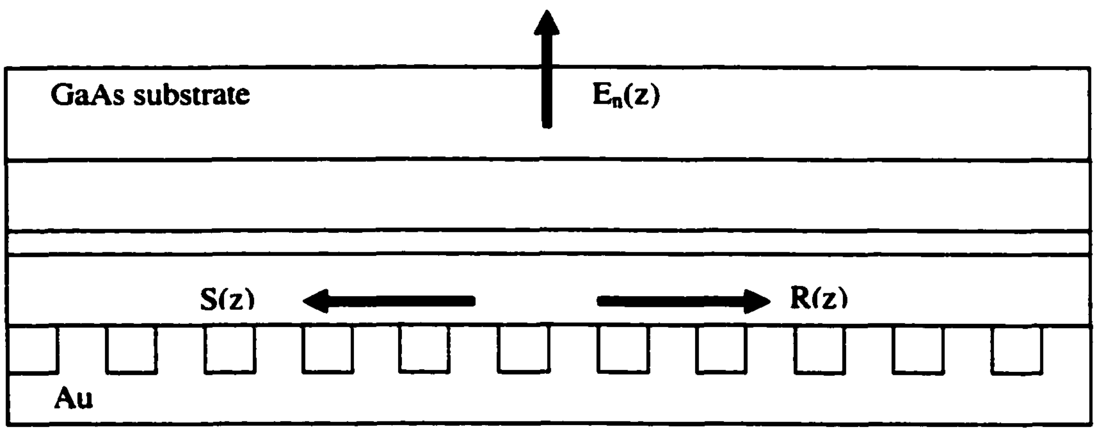

Fig. 3.2. Waveguide-grating structure. The 2[nd]-order grating provides both outcoupling light, $E_n(z)$ and in-plane feedbacks, R(z) and S(z).

The parameter ε(x,z) is the two-dimensional dielectric function and is varied along the z-direction due to the grating layer. The function ε(x,z) can be expressed in a Fourier expansion:

$$\varepsilon(x,z) = n^2(x) + \sum_{m=-\infty}^{\infty} \varepsilon_m(x) e^{imK_o z} \tag{3.2}$$

where $n^2(x)$ is the 0^{th}-order term, which represents the index profile in the structure for which the grating layer is represented by the average dielectric constant. The propagation constant is:

$$K_o = \frac{2\pi}{\Lambda} = \frac{2\pi n_{eff}}{\lambda_o} = k_o n_{eff} \tag{3.3}$$

The field in a grating region without any phaseshift is approximated by a pure transverse-electric form:

$$E_g(x,z) = E_o(x)[R(z)e^{iK_o z} + S(z)e^{-iK_o z}] \tag{3.4}$$

where $E_o(x)$ is the guided-mode field, $R(z)$ is right-going guided-mode amplitude, and $S(z)$ is left-going guided-mode amplitude. The coupled-wave equations are given by:

$$\begin{aligned} \frac{\partial R(z)}{\partial z} &= [\alpha(z) + i\delta + i\zeta)R(z) + i\kappa S(z) \\ \frac{-\partial S(z)}{\partial z} &= [\alpha(z) + i\delta + i\zeta)S(z) + i\kappa R(z) \end{aligned} \tag{3.5}$$

where $\alpha(z)$ is a complex-valued amplitude which represents the field gain. The term δ is the detuning factor, which represents how much the operating center wavelength deviates from the Bragg condition. ζ is a correction parameter which is determined by metal and surface losses and Bragg offsets.

The detuning factor, which is the wavelength shift from the Bragg condition due to the (transparency) refractive index, $\Delta n_{eff,0}$, the injected carriers, Δn_{dep}, and the index difference due to structure design, Δn_{dbr}, is given by:

$$\delta = \frac{\omega_o}{c}(n_{eff,0} + \Delta n_{dep} + \Delta n_{dbr}) - \frac{\pi}{\Lambda} \tag{3.6}$$

The term Δn_{dep}, which is a real value, depends on the antiguiding factor, b, which is defined as the ratio of decrease in the real part of refractive index, Δn_r, to the increase in the imaginary part of refractive index, Δn_i; [4]

$$b = \frac{-\Delta n_r}{\Delta n_i} \tag{3.7}$$

This change in n_r is due to the carrier injection within the active region, which acts to depress the refractive index at the lasing wavelength thereby enhancing the longitudinal radiation losses. The imaginary refractive index is related to the gain g by;

$$\Delta n_i = \frac{g}{2k_o} \tag{3.8}$$

where $k_o = 2\pi/\lambda_o$, with λ_o the free space wavelength.

The correction parameter, ζ, and coupling coefficient, κ, in Eq. 3.5 are complex-valued and are related to the surface diffraction loss coefficient, the resonant wavelengths in infinite length calculation, and the metal loss coefficient.[3] The term ζ corrects the gain thresholds and Bragg offsets to account for surface radiation.

The parameters κ, ζ and α_{surf} (surface loss) are then used in the transfer matrix method, from which the gain threshold, g_{th}, the external differential quantum efficiency, η_D, the guided-field and near-field intensity profiles, and the farfield pattern of the DFB modes are calculated.

3.1.2 The transfer-matrix method

The transfer matrix technique has been a convenient approach for analyzing multi-section structures. The laser structure that is considered here contains a number of regions, namely antireflection regions, passive-DBR regions, and active-DFB region. For each section we look at the right-propagating field R(z) on the left-hand side and the left-propagating field S(z) on the right-hand side of the section.

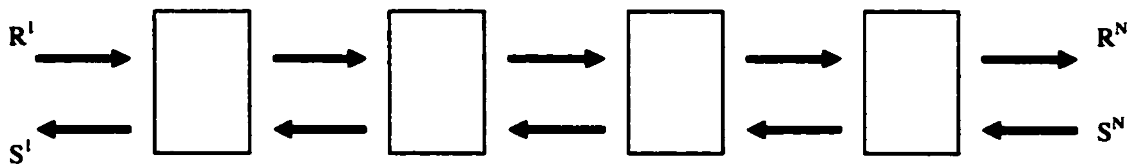

Fig. 3.3. Multi-section structure

The fields on the left-hand side and on the right-hand side of section i are related by a transfer matrix F_i.

$$\begin{Bmatrix} R^{i+1} \\ S^{i+1} \end{Bmatrix} = \begin{Bmatrix} A & B \\ C & D \end{Bmatrix} \begin{Bmatrix} R^{i} \\ S^{i} \end{Bmatrix} = \overline{\overline{F}}_i \begin{Bmatrix} R^{i} \\ S^{i} \end{Bmatrix} \tag{3.9}$$

The transfer matrix for the complete structure is found by matrix multiplication:

$$\overline{\overline{F}} = \overline{\overline{F_N}}\,\overline{\overline{F_{N-1}}} \ldots\ldots \overline{\overline{F_2}}\,\overline{\overline{F_1}} \tag{3.10}$$

$$\begin{Bmatrix} R^{N+1} \\ S^{N+1} \end{Bmatrix} = \overline{\overline{F}} \begin{Bmatrix} R^{1} \\ S^{1} \end{Bmatrix} \tag{3.11}$$

For a laser for which there are no incoming fields ($S^{N+1} = R^1 = 0$), but there are outgoing fields (R^{N+1} and $S^1 \neq 0$). This gives the lasing condition:

$$F_{22} = 0 \tag{3.12}$$

For the DFB structure we consider here, the end reflection matrix form can be written as:

$$\overline{\overline{F}}(r) = \begin{Bmatrix} \dfrac{1}{1-r} & \dfrac{-r}{1-r} \\ \dfrac{-r}{1-r} & \dfrac{1}{1-r} \end{Bmatrix} \tag{3.13}$$

where r is the (amplitude) reflectivity. For a homogenous section of length L with a propagation constant β we have:

$$\overline{\overline{F}}(L)=\begin{Bmatrix} e^{-j\beta L} & 0 \\ 0 & e^{j\beta L} \end{Bmatrix} \tag{3.14}$$

The transfer matrix for a conventional periodic structure of length L can be derived from the coupled- mode theory [5] to be:

$$\overline{\overline{F}}_{DFB}=\begin{Bmatrix} \cosh(\gamma L)+\frac{\alpha-j\delta}{\gamma}\sinh(\gamma L) & -\frac{j\kappa}{\gamma}\sinh(\gamma L) \\ \frac{j\kappa}{\gamma}\sinh(\gamma L) & \cosh(\gamma L)-\frac{\alpha-j\delta}{\gamma}\sinh(\gamma L) \end{Bmatrix} \tag{3.14}$$

The parameter $\delta = \beta - \beta_o$.

The transfer matrix for the composite DFB/DBR structure with central phaseshift is:

$$\overline{\overline{F}} = \overline{\overline{F}}(r_r)\overline{\overline{F}}_{DBR}\overline{\overline{F}}_{DFB}\overline{\overline{F}}_{DBR}\overline{\overline{F}}(r_l) \tag{3.15}$$

Once Eq. 3.15 is solved for the threshold gain, g_{th}, and the detuning factor, δ, for this multi-section structure, then the field inside the waveguide, the guided-field profile, is obtained from:

$$\left(|E_g(z)|\right)^2 = \left(|S(z)|^2 + |R(z)|^2\right) \tag{3.16}$$

and the corresponding radiated near-field intensity profile is given by the square of the amplitude sum of the right- and left-going wave:

$$\left(|E_n(z)|\right)^2 = \left(|S(z)+R(z)|\right)^2 \tag{3.17}$$

From here, the external differential quantum efficiency, η_D, can be calculated as:

$$\eta_D = \eta_i \frac{2*\alpha_{DBR}\int^{L_{DBR}}|R(z)+S(z)|^2 dz + \alpha_{DFB}\int^{L_{DFB}}|R(z)+S(z)|^2 dz}{\int_{g(z)>0} g(z)\left[|R(z)|^2+|S(z)|^2\right]dz} \tag{3.18}$$

where the internal cavity loss, α_i, is included in the field gain, $g(z)$. The terms α_{DFB} and α_{DBR} are the surface-loss coefficients in the active region (i.e. DFB section) and passive regions (i.e. DBR sections), respectively. η_i is the internal efficiency. L_{DBR} is the length of one section of DBR and L_{DFB} is the length of DFB section.

3.2 Design Calculation

To analyze 2nd-order DFB lasers, Noll et. al.[3] has developed a method that includes the effect of the radiation field to the surface. However, there have been no reports on applying the transfer-matrix method for analyzing 2nd-order DFB lasers, that includes the effect of radiation and absorption loss, detuning due to current injection into the active region and the wavelength shift due to design structure. Hence, some parameters in the transfer-matrix method must be modified to accommodate the above factors.

In the composite DFB/DBR lasers, the difference in effective refractive index between the passive-DBR and active-DFB regions results in detuning of the Bragg offset. Current injection into the active-DFB region results in more deviation of the DFB Bragg condition from the DBR Bragg condition. The background absorption loss in the passive-DBR region needs to be considered as well. Moreover, the surface radiation loss must be included in the transfer-matrix method to effectively account for the effect of the complex coupling coefficient and the complex ζ term. Eq. (3.14) has to be modified to account for the effect of current injection, outcoupled loss, the absorption loss, and the effective-index difference between active-DFB region and passive-DBR region. The modified transfer matrix for the composite DFB/DBR structure can be written as:

$$\overline{\overline{F}}_{grating} = \begin{Bmatrix} \cosh(\gamma L) + \dfrac{\alpha_o^{'} - j\delta^{'}}{\gamma}\sinh(\gamma L) & -\dfrac{j\kappa}{\gamma}\sinh(\gamma L) \\ \dfrac{j\kappa}{\gamma}\sinh(\gamma L) & \cosh(\gamma L) - \dfrac{\alpha_o^{'} - j\delta^{'}}{\gamma}\sinh(\gamma L) \end{Bmatrix} \qquad (3.19)$$

For the active-DFB region:

$$\begin{aligned} \alpha_o^{'} &= -\mathrm{Im}(\zeta_{dfb}) + \alpha_o \\ \delta^{'} &= \mathrm{Re}(\zeta_{dfb}) + \delta + \delta_{dp} \end{aligned} \qquad (3.20)$$

where δ_{dp} is the detuning due to current injection.

For the passive-DBR region:

$$\begin{aligned} \alpha_o^{'} &= -\mathrm{Im}(\zeta_{dbr}) - \alpha_{dbr} \\ \delta^{'} &= \mathrm{Re}(\zeta_{dbr}) + \delta + \delta_{dbr} \end{aligned} \qquad (3.21)$$

The parameter α_{dbr} is the background absorption loss in passive-DBR region and δ_{dbr} is the detuning due to effective refractive-index difference between the active-DFB region and the passive-DBR region.

The inclusion of the phaseshift, $\Delta\phi$, in the grating structure modifies the transverse electric field on Eq. 3.4. The field now becomes:

$$E_g(x,z) = E_o(x)[R(z)e^{i(K_o z + \Delta\phi(z))} + S(z)e^{-i(K_o z + \Delta\phi(z))}] \qquad (3.22)$$

and the differential equations [6] for right-going, $R(z)$, and left-going, $S(z)$, fields are given by:

$$\begin{aligned} \frac{\partial R(z)}{\partial z} &= [\alpha(z) + i\delta + i\zeta]R(z) + i\kappa S(z)e^{2i\Delta\phi(z)} \\ \frac{-\partial S(z)}{\partial z} &= [\alpha(z) + i\delta + i\zeta]S(z) + i\kappa R(z)e^{-2i\Delta\phi(z)} \end{aligned} \qquad (3.23)$$

The phaseshift at the center is written in degrees, so the transfer-matrix equation for the phaseshift is:

$$\overline{\overline{F}}_{\phi} = \begin{Bmatrix} e^{-j\phi} & 0 \\ 0 & e^{j\phi} \end{Bmatrix} \tag{3.24}$$

The transfer matrix for the composite DFB/DBR structure with central phaseshift is:

$$\overline{\overline{F}} = \overline{\overline{F}}(AR)\overline{\overline{F}}_{DBR}\overline{\overline{F}}_{DFB}\overline{\overline{F}}(\Delta\phi)\overline{\overline{F}}_{DFB}\overline{\overline{F}}_{DBR}\overline{\overline{F}}(AR) \tag{3.25}$$

Chapter 3 References

[1] J. Lopez, G. Witjaksono, and D. Botez, "Single-Mode, Single-Lobe Operation of Surface-Emitting, Second-Order Distributed Feedback Lasers," Appl. Phys. Lett, 75 (7), 885 (1999).

[2] G. Witjaksono and D. Botez, "Surface-Emitting, Single-Lobe Operation from 2nd-order DFB/DBR Lasers with Central Grating Phaseshift," Proc. 2000 IEEE 17th ISLC, 35 (2000).

[3] R. J. Noll and S. H. Macomber, "Analysis of Grating Surface Emitting Lasers," *IEEE J. of Quantum Electron.* **26** (3), 456 (1990).

[4] W. Streifer, R. D. Burham, and D. R. Scifres, "An analytic study of (GaAl)As gain guided lasers at threshold," IEEE J. Quantum Electron. QE-18, 856 (1982).

[5] Jens Buss, "*Single Frequency Semiconductor Lasers*," Published by SPIE - International Society for Optical Engineering, WA (1991).

[6] S. Macomber, private communication.

Chapter 4

Device Simulation of Surface-Emitting 2nd-Order Distributed Feedback Laser with Central Phaseshift Grating

The device-composite structure is simulated by dividing the longitudinal region into several finite sections, i.e. the antireflection regions, a phaseshift region, and the grating regions. The grating regions consist of a single finite-DFB section and two finite-DBR sections. The coupled-mode theory (CMT) for the 2nd-order DFB surface emitter is then used to calculate the coupling coefficient, κ, the correction parameter, ζ, and the surface loss in the finite-grating regions. Later, the transfer-matrix method is utilized to obtain the grating field loss and frequency shift for the whole structure, in which detuning due to the index differences in the DFB and DBR regions and the index depression due to current injection are included in the calculation. By combining both the coupled-mode theory for a finite grating and the transfer-matrix method for a multi-section structure, this scheme not only efficiently solves the composite DFB/DBR structure without the need for complex numerical techniques, but also allows for independent optimization (for efficient surface emission) of each grating section.

4.1 Device Parameters

Fig. 4.1 shows the composite DFB/DBR structure under study. The structure has an n-doped 1μm-thick n-InGaP-cladding layer and a 100nm-thick InGaAsP (1.6 eV) lower optical-confinement layer. Two 7nm-thick InGaAs quantum wells separated by a 20nm-thick InGaAsP(1.6eV) barrier layer form the active region. Next are a 100nm-thick InGaAsP upper optical-confinement layer, a 300nm-thick p-InGaP cladding layer, and a p^+-GaAs grating layer of 3000Å period and incorporating a central phaseshift, $\Delta\phi$. SiO_2 is then deposited and etched to create DBR regions. Au is then deposited on the top of GaAs-cap to form electrical contact to the DFB region. The GaAs/Au grating provides both high coupling coefficient, κ, as well as insures that all first-order diffracted light is collected. Absorbing InGaAs regions are then regrown (not shown) at the ends of the DBR regions, to insure virtually zero reflections. The light is emitted through a window in the n-side metallization of the GaAs substrate.

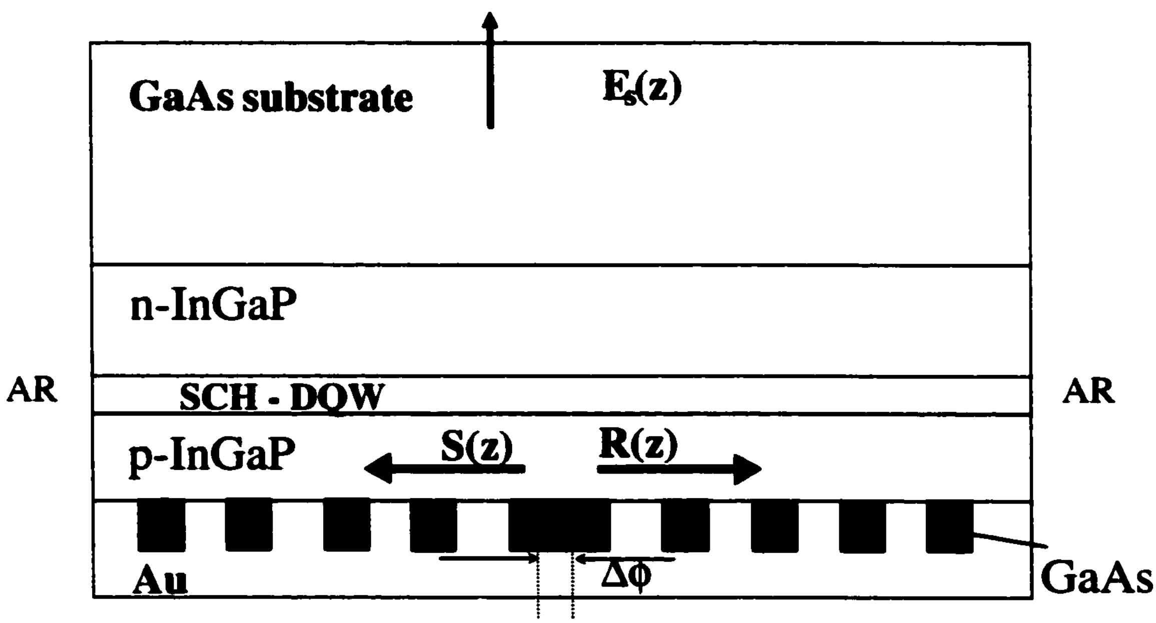

Fig. 4.1 Surface-emitting DFB structure.

The parameters for the devices used in the analysis are listed in Table I. The grating, which consists of Au/GaAs, provides the high coupling coefficient values needed to obtain high differential quantum efficiency. Both ends of passive-DBR sections are set to have zero reflectivity (AR). Moreover the background absorption loss coefficient in the passive-DBR region is set to 15 cm^{-1} [1], and the index difference (Δn) between DFB-DBR regions is 3×10^{-4}.

TABLE 4.1

PARAMETERS OF THE COMPOSITE DFB/DBR LASER

Lasing wavelength, λ	0.98 μm
Confinement factor, Γ	10%
Thickness of grating, g	0.1 μm
Transverse effective index, n_{eff}	3.27
DFB coupling coefficient, κ_{DFB}	-5.47 + i49.42
DFB correction parameter, ζ_{DFB}	36.43 + i50.28
DBR Coupling coefficient, κ_{DBR}	2.75 + i30.46
DBR correction parameter, ζ_{DBR}	-37.98 + i31.19
Absorption loss in DBR, $\alpha_{DBR} = \Gamma G$	15 cm^{-1} [1]
Index difference of DFB-DBR, Δn	3 x 10^{-4}
Detuning factor, b	2

The get the optimum design iterations of the length study and the phaseshift study are done several times. Our initial goal is to achieve single-mode operation with a single-lobed farfield beam at certain lengths of the DFB- and DBR- sections and over a certain range of phaseshift. Later, for high power operation, it is also required to optimize the design for large discrimination against other longitudinal modes, high quantum efficiency, and high degree of uniformity of the guided field as well as a relatively low threshold gain.

4.2 Length Study

The device design performance is explored by evaluating many different distributed-feedback (DFB) lengths as well as distributed-reflector (DBR) lengths. The central phaseshift is set to be 180° during this study.

Surface-emitting 2^{nd}-order DFB lasers are equivalent to complex-coupled 1^{st}-order DFB lasers. For a surface-emitting 2^{nd}-order grating the imaginary part of the coupling coefficient, κ_i, is a function of the surface (radiation) loss and the metal loss. Complex-coupled DFB lasers have several characteristics, which are superior to those of index-coupled DFBs [2], not the least of which is the removal of modal degeneracy. The lifting of the mode degeneracy is due to a phenomenon called the standing wave factor. [3] The two counter-propagating waves R(z) and S(z) in a DFB produce a standing wave pattern. This standing wave overlaps the gain profile in such a manner as to alter the overall losses and hence the threshold gain for a particular mode. The better the overlap, the better the gain enhancement. The amount of overlap is quantified by a parameter called the standing wave factor, f_{st}. The standing wave overlap, $\kappa_i f_{st}$, can reduce the threshold gain. In this numerical analysis, the threshold gain, g_{th}, is defined as the sum of the effective grating loss (α_{rad}), the edge loss, α_{edge}, both are function of coupling coefficient, and the internal cavity loss, α_i.

$$g_{th}(\kappa L) = \alpha_{rad}(\kappa L) + \alpha_{edge}(\kappa L) + \alpha_i \tag{4.1}$$

where the α_{rad} is the sum of the 1^{st}-order diffraction loss, α_{surf}, the metal loss, α_m, grating mirror loss, α_g, and the standing wave overlap, $-\kappa_i f_{st}$.. The radiation loss, α_{rad}, is proportional to the integral of the near-field intensity profile $|R(z)+S(z)|^2$ over the cavity length.

We also define a guided-field aspect ratio, R, which is the peak-to-valley ratio of the guided-field intensity profile within the DFB region. Thus R characterizes the degree of uniformity of the longitudinal guided-field profile, a relevant factor at high drive levels above threshold.

$$R = \frac{\left|E_{dfb}\right|^2_{peak}}{\left|E_{dfb}\right|^2_{valley}} \tag{4.2}$$

4.2.1 DFB-Length Study

The DBR-region length on each side of DFB region is set to be 500 μm. The length is determined to make sure that the fields at the DBR ends are close to zero, and assuming perfect AR coatings, no fields are reflected back into the device. The analysis becomes much more complicated in the case if there is reflection from the DBR-ends because the device performance is very sensitive to the unavoidable random phase introduced as a result of the uncontrollable nature of the cleave or etch location to the phase of the submicron-period DFB grating.

Figs. 4.2 and 4.3 show how the threshold gain, g_{th}, the intermodal discrimination, Δg_{th}, the external quantum efficiency, η_D, and the guided-field uniformity (i.e. aspect ratio), R, vary with DFB-region length.

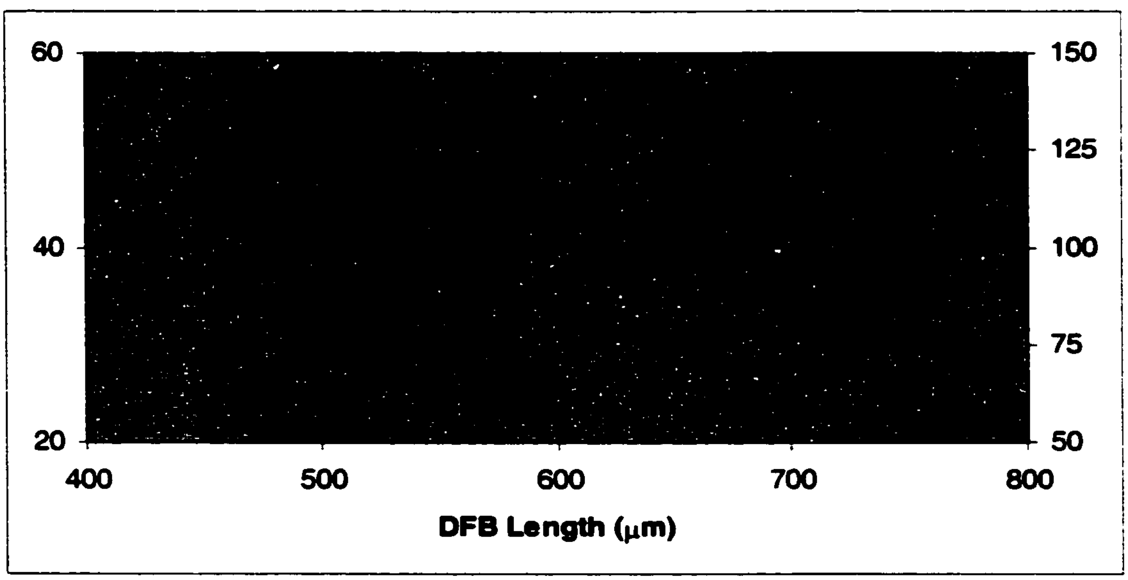

Fig. 4.2 The curves show how (a) threshold gain, intermodal discrimination, and quantum external efficiency vary with DFB-length with DBR-length is set to 500 μm.

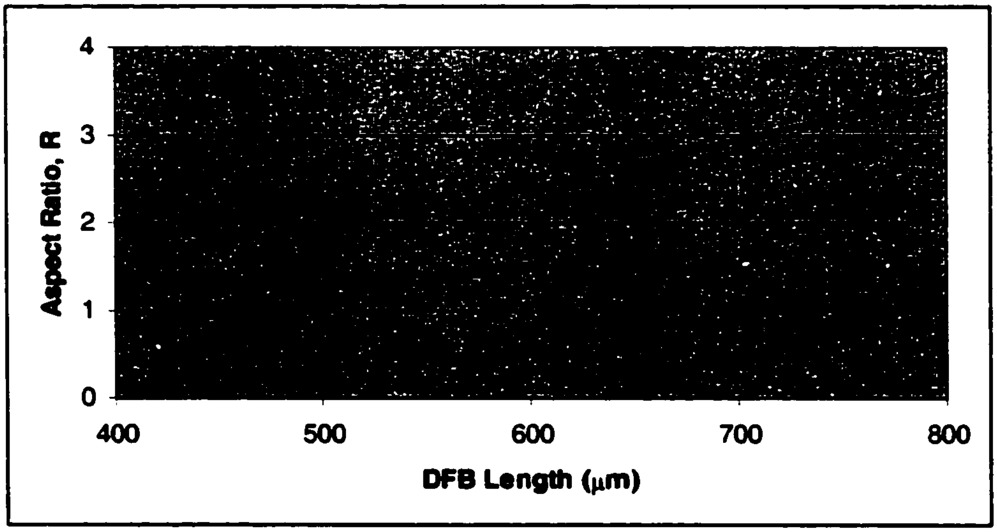

Fig. 4.3 The curve shows how the aspect ratio varies with DFB-region length when the DBR-region length is set to 500 μm.

It is clear from the curves that increasing the DFB length increases η_D while reducing g_{th}. However, these improvements come at two costs: 1) reduction of the modal discrimination between the symmetric and the antisymmetric modes, and 2) increase aspect ratio.

Figures 4.4 and 4.5 show the guided-field profiles at DFB-length of 300 μm and 800 μm, respectively and their far-field patterns.

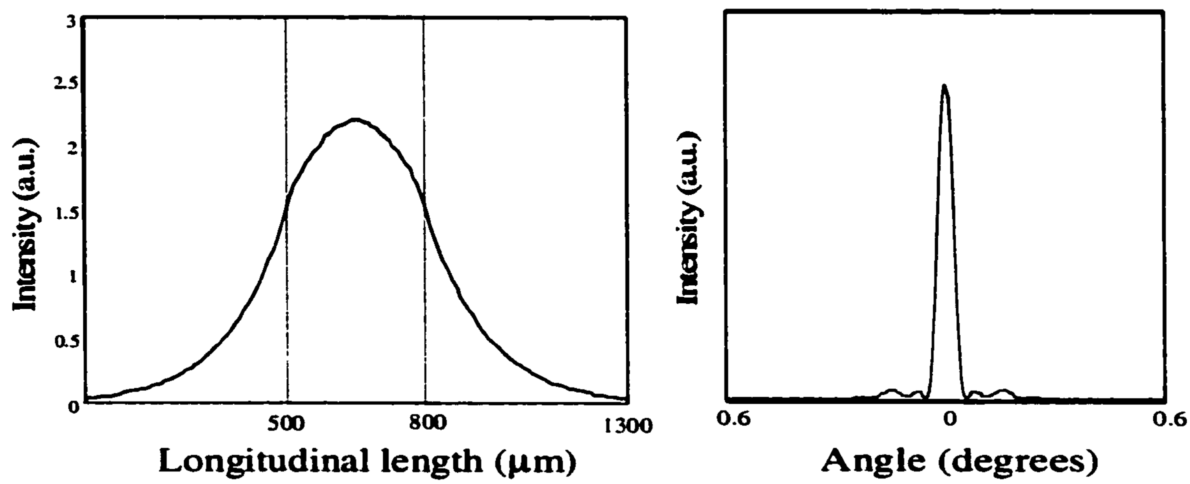

Fig 4.4 The guided-field profile and its farfield for the device with DFB length of 300 μm and DBR length of 500 μm.

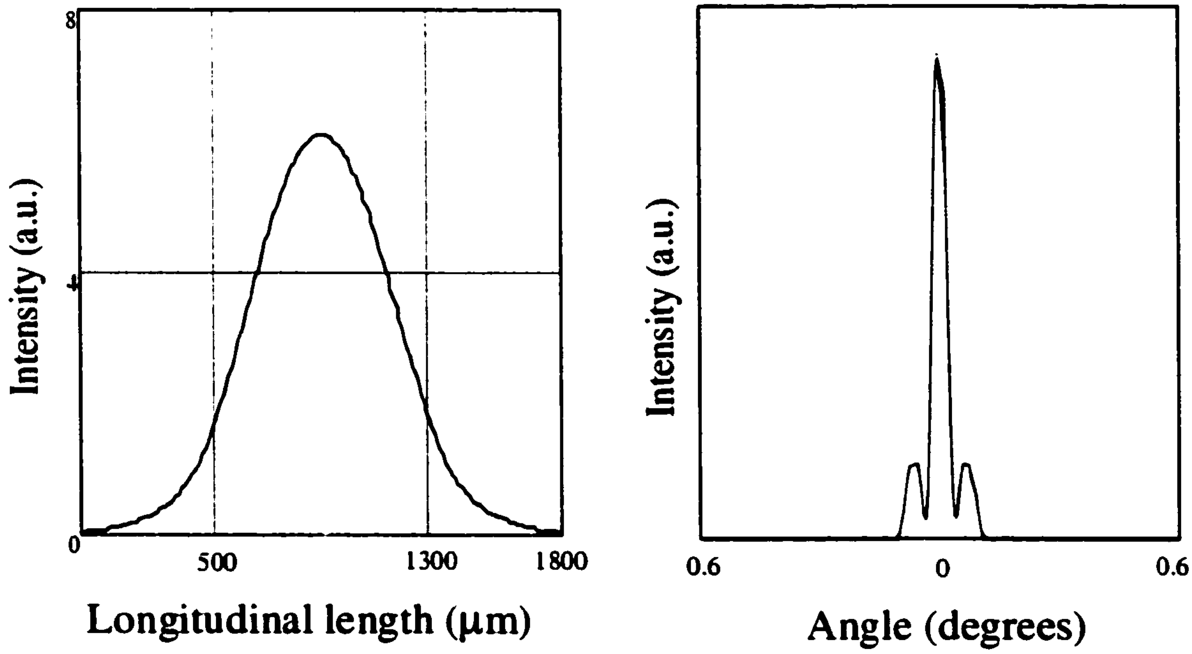

Fig 4.5 The guided-field profile and its farfield for the device with DFB length of 800 μm and DBR length of 500 μm.

As the DFB-region length increases, hence κL increases, it is appearent that the field inside the waveguide has higher aspect ratio. The device operation can then become susceptible to longitudinal gain spatial hole burning for increasing κL. If the coupling becomes too large, light is trapped within the cavity. In this case, the guided-field uniformity is worsen.

Moreover when the central-lobe energy content is taken into account, the effective quantum efficiency, $\eta_{D,eff}$, which is the product of the external quantum efficiency and the power content in the main lobe, can be calculated. Fig. 4.6 shows how the central-lobe energy content and the effective quantum efficiency vary as the DFB-region length changes. In contrast to the trend in the external quantum efficiency, the effective quantum efficiency, $\eta_{D,eff}$ decreases as the DFB-region length increases.

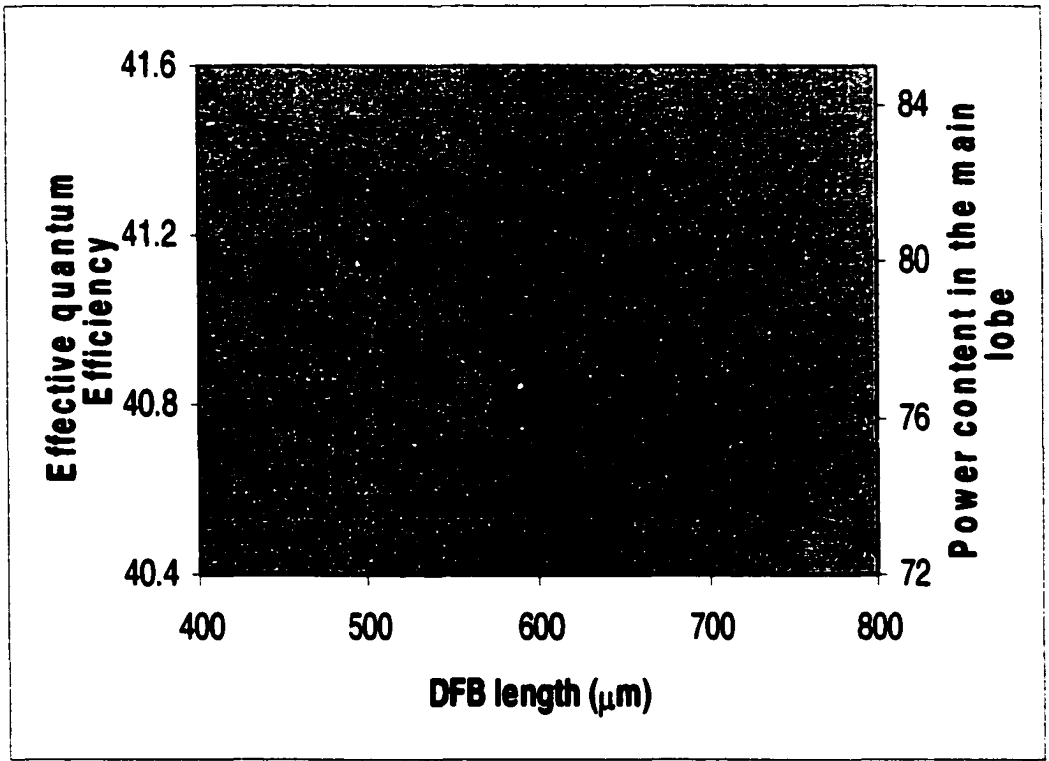

Fig 4.6 The plot of central-lobe energy content (FF_{main}) and effective quantum efficiency as DFB length varied.

4.2.2 DBR-Length Study

Fig. 4.7 shows how the threshold gain, g_{th}, the intermodal discrimination, Δg_{th}, the external quantum efficiency, η_D, and the guided-field uniformity (i.e. aspect ratio), R, vary with the DBR length when the DFB-region length is set to be 500 μm. It is clear from the curves in Fig. 4.6 that increasing the DBR length does not change much of device performances (e.g. g_{th}, Δg_{th}, η_D and R). However, as the DBR length increases, it increases the total length of the composite DFB/DBR, which makes the total number of devices per wafer decreases.

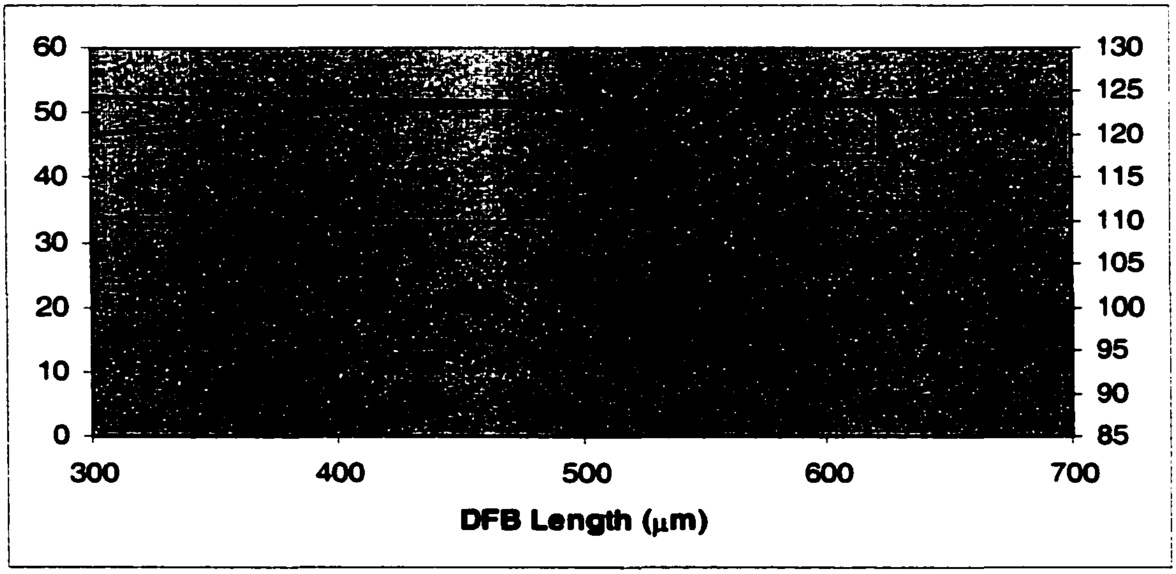

(a)

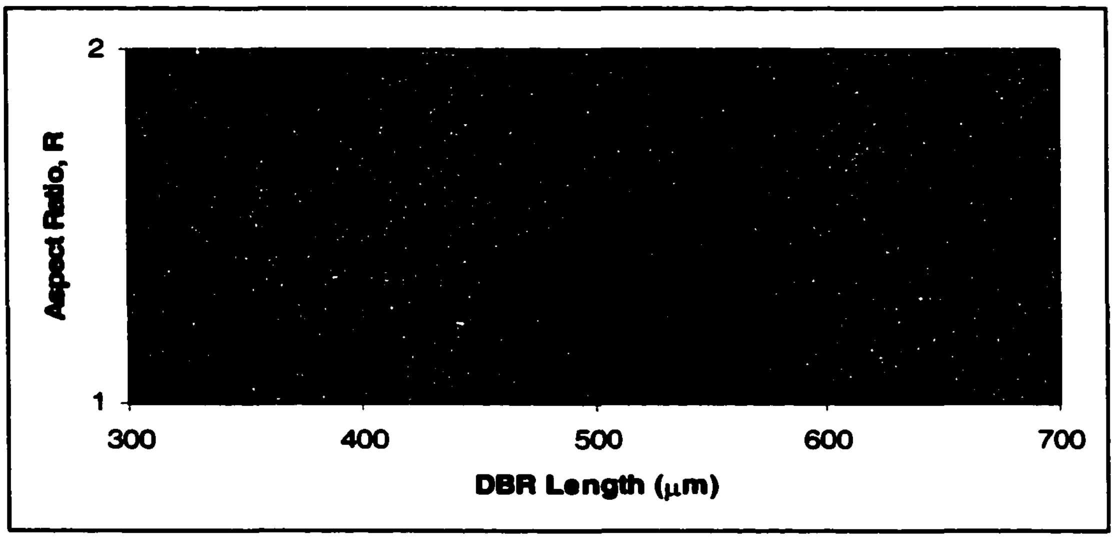

(b)

Fig. 4.7 The curves show (a) how threshold gain, intermodal discrimination, quantum external efficiency; (b) and aspect ratio vary with DBR-length with DFB-length is set to be 500 μm.

Decreases the DBR length below 300 μm makes discrimination decreases, Δg_{th}, and the edge loss, α_{edge}, increases, hence the threshold gain, g_{th}, increases as well (Eqn. 4.1). Fig 4.8 shows the guided-field profile, which has ~10% of the field at the edge of DBR ends, for 200 μm

DBR length. High portions of field at the edges will increase the edge loss and at the same time can disrupt the DFB performance due to reflections at the edges from imperfect AR coatings.

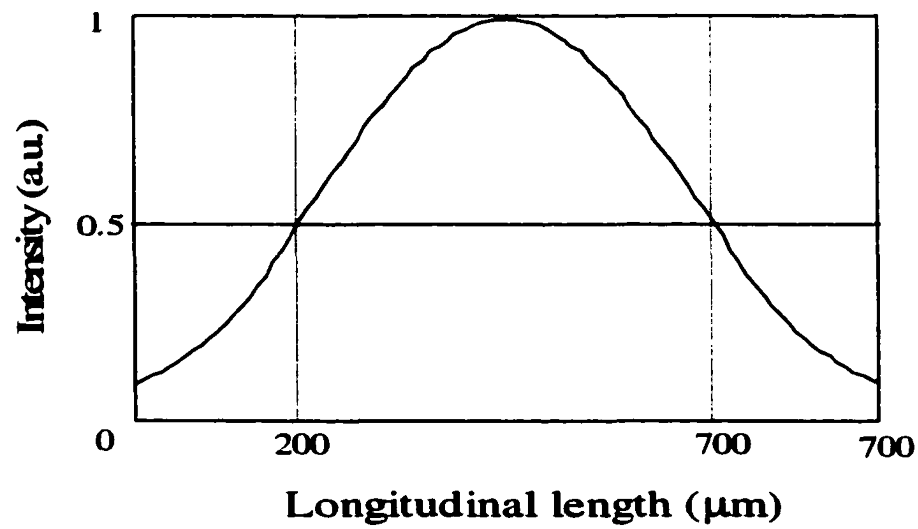

Fig 4.8. A guided-field profile for DBR length of 200 μm, which shows considerable amount (~10%) of the field at the edge.

4.3 Central Grating Phaseshift Study

The device characterization is now explored by changing the central grating phaseshift while keeping the length of DFB and DBR constant. The lengths of each passive-DBR and the active-DFB regions are 500 μm each.

Fig. 4.9 shows how the threshold gains for symmetric modes (S) and antisymmetric modes (A) vary as the central grating phaseshift is varied [4]. As seen in Fig. 4.9, a symmetric-like mode (S) is favored to lase over the antisymmetric one (A) when the phaseshift, $\Delta\phi$, ranges from 100° to 280°, with maximum discrimination occurring when $\Delta\phi$ = 180°; i.e., a half-wave ($\lambda/2$) central phaseshift. Large discrimination (>100 cm^{-1}) is still maintained over phaseshift values of 150° to 210°. The largest discrimination occurs at $\Delta\phi$=180° : a value of 130 cm^{-1}.

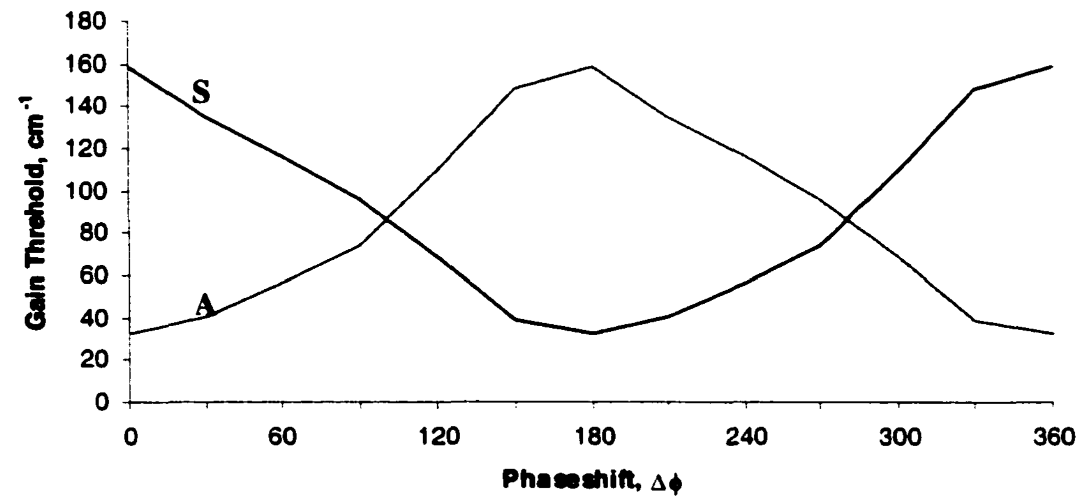

Fig. 4.9. Threshold gain as a function of the grating central phaseshift, $\Delta\phi$, value for modes of symmetric (S) and antisymmetric (A) radiated near-field amplitude profile.

The 180° phaseshift does *not* affect the in-plane propagating (guided) light, as the field roundtrip through the phaseshifter is 360° (i.e., the guided field remains antisymmetric). That is evidenced from the device spectra with and without 180° phaseshift (Figs. 4.10a and b, respectively). For both cases lasing occurs virtually at the Bragg wavelength. [The slight deviation from λ_{Bragg} is caused by the mixture of a complex-coupled grating from the DFB and the DBRs].

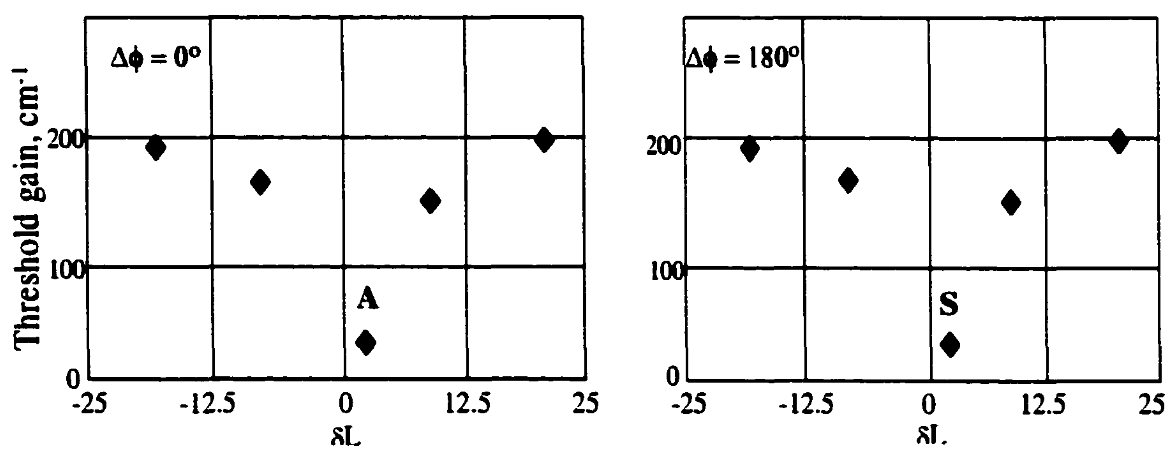

Fig. 4.10 (a) The DFB/DBR mode spectrum at $\Delta\phi$ = 0°; and (b) at $\Delta\phi$ = 180°, δ is deviation from Bragg frequency (i.e. $\beta - \beta_o$, where β_o is Bragg wavevector corresponding to the Bragg frequency), A and S are modes of antisymmetric and symmetric (radiated) near-field profiles, respectively.

For the grating-outcoupled light the π central-phaseshift region defines two surface-emitting regions whose outcoupled fields are *out-of-phase* with each other (Fig. 4.11).

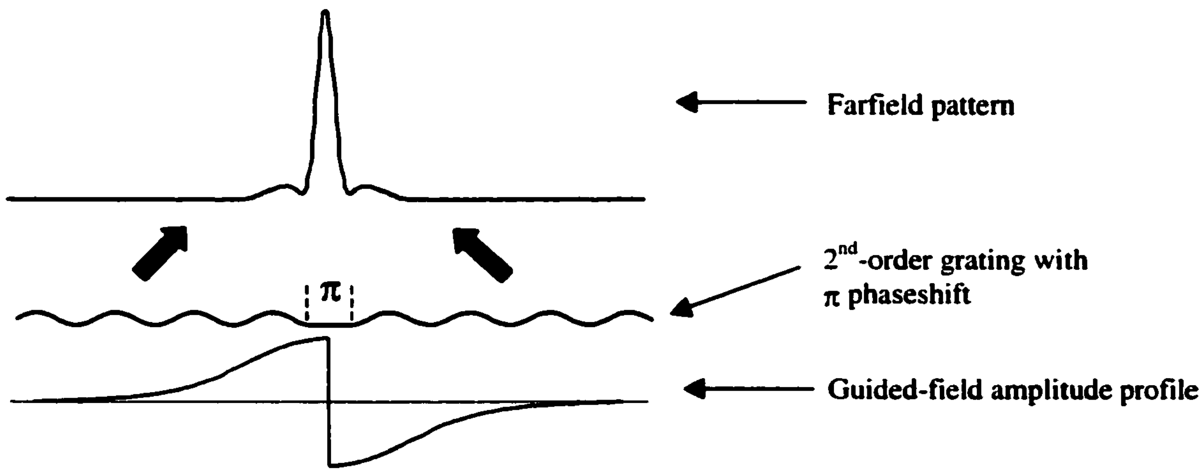

Fig. 4.11 The guided-field of antisymmetric amplitude profile is outcoupled in out-of-phase beams due to the π phaseshift at the grating center, thus resulting in a single-lobed, orthonormal farfield beam pattern.

Thus the outcoupling of the guided antisymmetric field provides in-phase (i.e. symmetric) radiated near-field and far-field patterns (Figs. 4.11 and 4.12b). The situation is quite similar to the use of π phase-shifter films on the facets of out-of-phase operating phase-locked arrays [5,6], in order to obtain in-phase beam patterns.

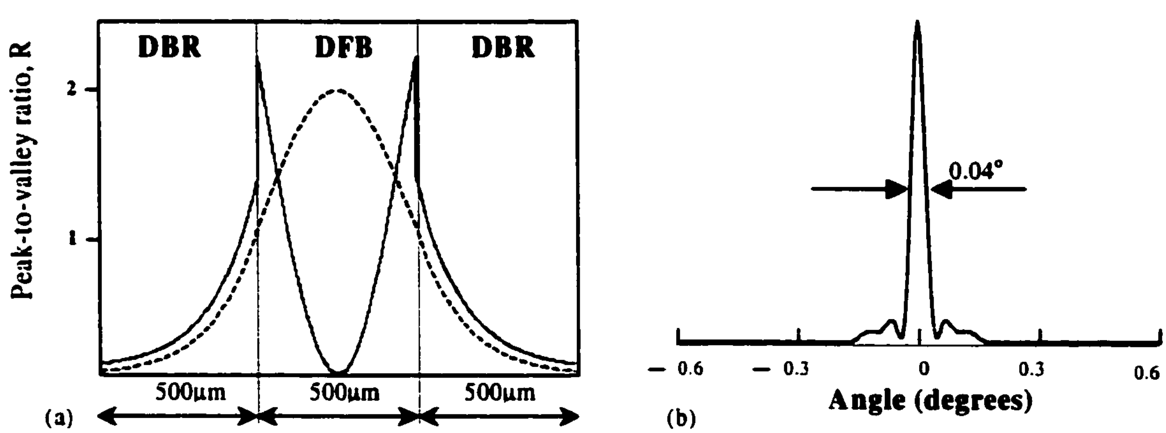

Fig. 4.12 DFB/DBR device with $\Delta\phi = 180°$: (a) Near-field (solid curve) and guided-field (dashed curve) intensity profiles. The left margin gives the guided-field peak-to-valley ratio, R, values in the DFB region; (b) Far-field beam pattern.

As seen in Fig. 4.12a, the guided-field peak-to-valley ratio, R, in the active (i.e., DFB) region is only 2, which insures single-mode operation to high powers since the intermodal discrimination is high (~ 100 cm^{-1}; Fig. 4.8.) The far-field consists of an *orthonormal* beam with 88% of the light in the central lobe.

The variation of the external quantum efficiency around the π-phaseshift is shown in Fig. 4.12. The differential quantum efficiency, η_D, is 51%, which reduces to 45% (i.e., effective η_D) when taking into account the central-lobe energy content [7]. Over a wide range in $\Delta\phi$: 150° to 210°; the effective η_D is relatively high (> 42%) (Fig. 4.13). We also find that the degree of guided-field uniformity is low (R<2) over the same range in $\Delta\phi$ (Fig. 4.14). These high degrees of uniformity as well as high effective quantum efficiencies over a wide range in phaseshift variation provide for large tolerances in device fabrication. Therefore a practical solution has been found for single (orthonormal)-lobe, efficient surface emission from 2nd-order DFB lasers.

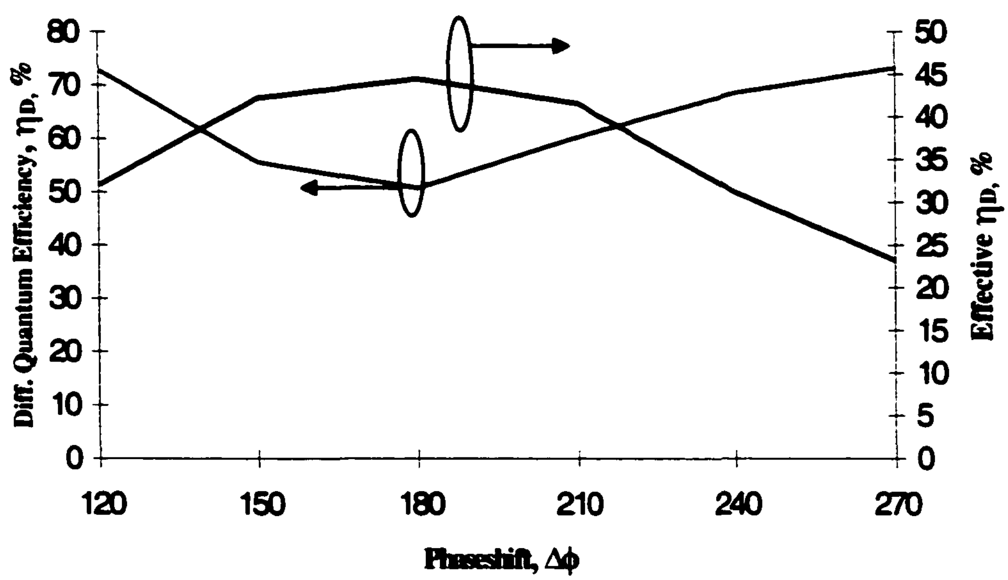

Fig. 4.13 Differential quantum efficiency, η_D, and effective η_D for DFB/DBR devices as a function of $\Delta\phi$.

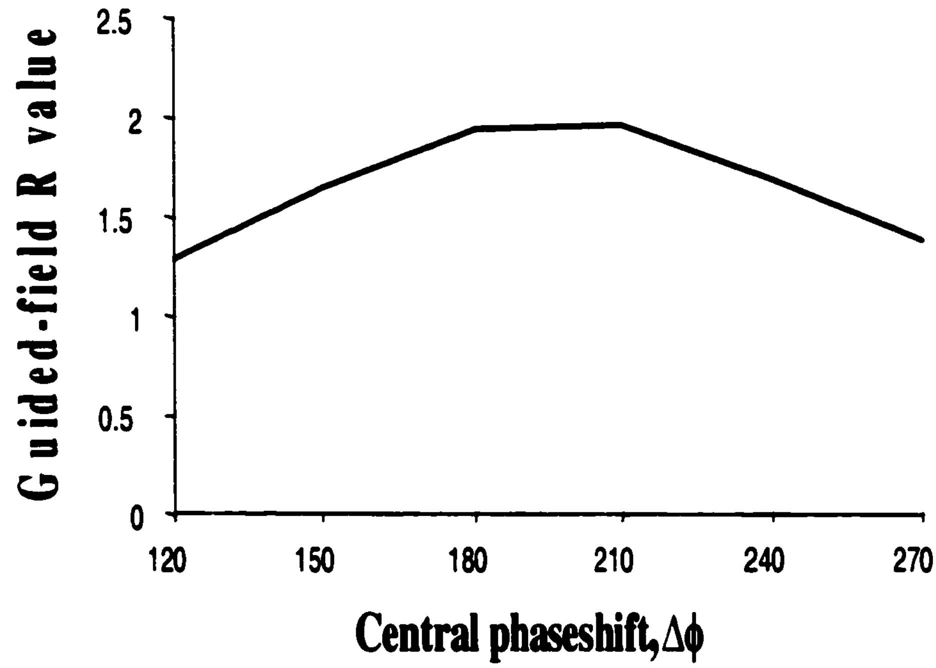

Fig. 4.14 Peak-to-valley ratio, R, of guided-field profile in the active (i.e. DFB) region for DFB/DBR devices as a function of $\Delta\phi$.

Moreover, for devices optimized for maximum η_D, we studied [8] the variation of the threshold gain and η_D as a function for the grating duty cycle, σ, defined as the ratio of Au as part of the grating period (Fig. 4.15a and b). [8] The intermodal discrimination, $\Delta\alpha$, reaches a maximum of 113 cm^{-1} for $\sigma = 0.5$, while the S-mode threshold gain is only 22 cm^{-1} for $\sigma = 0.4$, with a respectable $\Delta\alpha$ value: 52 cm^{-1}. For a device with 550 μm-long DBR region and 600 μm-long DBR regions, η_D reaches values as high as 62% for $\sigma = 0.4$ and has values above 50% over the σ range: 0.35-0.50 (Fig. 4.15b). The effective η_D varies like η_D: reaches a maximum of 55% for $\sigma = 0.4$ and stays above 44% for σ in the 0.35-0.5 range. Therefore the device can tolerate some variation in grating duty cycle at a relatively small penalty in slope efficiency.

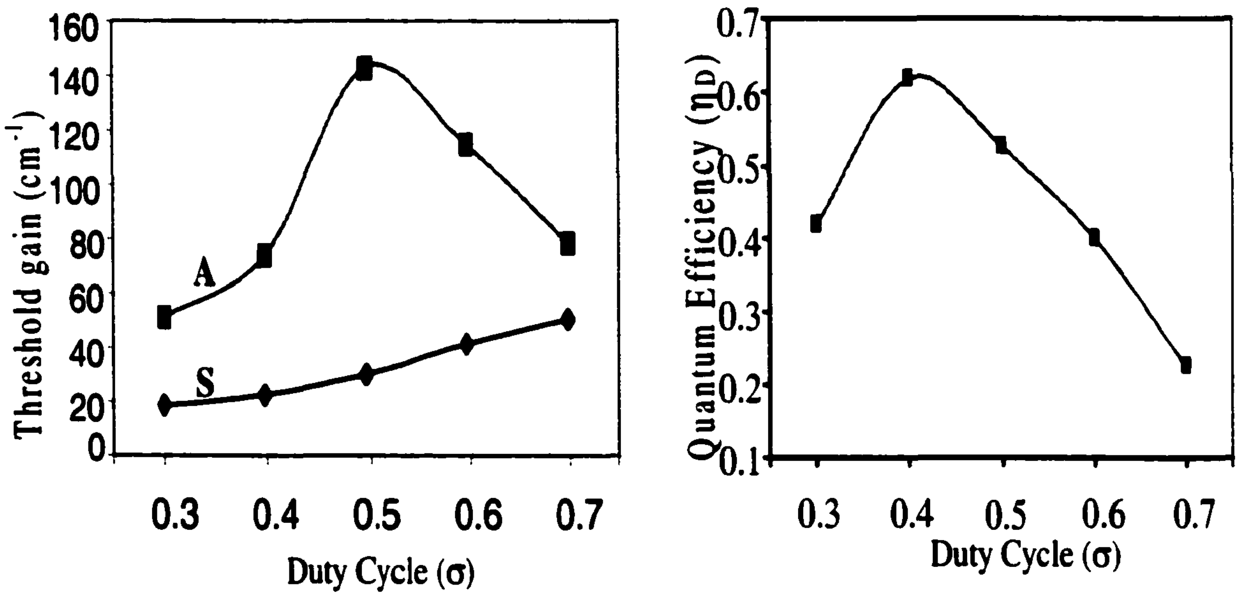

Fig. 4.15 (a) Threshold gains for symmetric (S) and antisymmetric (A) modes; and (b) the external differential quantum efficiency, η_D, for the S mode, as a function of the grating duty cycle.

Chapter 4 References

[1] M. Hagberg, N. Eriksson, and A. Larsson, "Investigation of high-efficiency surface-emitting lasers with blazed grating outcouplers," *IEEE J. Quantum Electron.* **32** (9), 1596-1605 (1996).

[2] Y. Luo, H.L. Cao, M. Dobashi, H. Hosomatsu, Y. Nakano, and K. Tada, "Gain-coupled distributed feedback semiconductor lasers with absorptive conduction-type inverted grating," IEEE Photon. Technol. Lett. Vol. 8, pp. 476-478 (1992).

[3] K. David, J. Buus, and R. Baets, "Basic Analysis of AR-coated, partly gain-coupled DFB lasers: the standing wave effects," IEEE J. QE-28, pp. 427-433 (1992)

[4] G. Witjaksono and D. Botez, "Surface-Emitting, Single-Lobe Operation from 2nd-order DFB/DBR Lasers with Central Grating Phaseshift," Proc. 2000 IEEE 17th ISLC, 35 (2000).

[5]. D. E. Ackley, D. Botez, and B. Bogner, "Phase-Locked Injection Laser Arrays with Integrated Phase Shifters," *RCA Review*, **44**, pp. 625-633, Dec. 1983.

[6] M. Matsumoto, M. Taneya, S. Matsui, S. Yano, and T. Hijikata, "Single-lobed far-field pattern operation in a phased array with an integrated phase shifter," Appl. Phys. Lett., **50**, 1541-1543, June 1987.

[7] G. Witjaksono and D. Botez, "Surface-Emitting, Single-Lobe Operation from 2nd-Order Distributed-Reflector Lasers with Central Grating Phaseshift," *Appl. Phys. Lett.*, **78**, 4088-4090 (2001).

[8] G. Witjaksono, S. Li, and D. Botez, "High-efficiency, Single-lobe Surface-Emitting DFB/DBR Lasers", Paper TuA3 at the 14th IEEE LEOS Annual Meeting, 12-15 Nov. 2001, San Diego, CA.

Chapter 5

Fabrication of 2^{nd}-Order DFB Incorporating Central π-Phaseshift Grating

The previous chapter concluded with the simulation results from single-element (i.e. ridge-guide) surface emitter incorporated with central π-phaseshift grating. The next step is to fabricate such devices and to show that single-lobed operation can be achieved using this design. This chapter discusses a fabrication method of patterning 2^{nd}-order DFB with central π-phaseshift on a photoresist using holographic exposure system and a grating transfer process from the photoresist to GaAs layer via dry- and wet-etching. Sec. 5.1 describes the fabrication procedure of patterning 2^{nd}-order grating via the image reversal method to produce central π-phaseshift. Sec.5.2. addresses the resulting patterns in the photoresist from the image reversal method. Next step is to transfer the grating pattern in the photoresist into the GaAs-cap layer. Sec. 5.3 discusses the dry- and wet-etching process, which has been developed, for transferring the grating pattern into the GaAs layer. The unique challenges imposed to make single-element device, which is surface-emitting through the n-side window will follow in the next chapter.

5.1 Fabrication Procedure of Patterning 2^{nd}-Order Grating with Central π-Phaseshift

E-beam lithography has been widely used for fabrication of grating on the edge-emitting semiconductor lasers. This technique has advantages of being able to control precisely not only the grating period but also grating duty cycle. However, the cost and the maintenance of such a system can be very high, and more importantly exposure over large area samples introduces stitching errors. Other method of patterning the grating is by using interferometric lithography (holographic exposure) system. The holographic system uses expanding beams that are folded back to produce a grating interference pattern at the sample location.

The holographic system is preferred over e-beam lithography to expose large area because of no stitching errors. The exposure source of the holographic system is an argon-ion laser operating single-frequency at 351.1 nm. Grating with a spatial wavelength, Λ, around 3000 Å (second order grating for λ=0.965 μm) are exposed in diluted AZ5206 (1 part AZ5206 photoresist : 1 part AZ1500 thinner). The nominal resist thickness is 80 nm. Samples are prebaked on the hot plate at 120° C for 1 minute. Typical exposure times are 120 seconds for laser power of 130 – 150 mW. For positive image, the samples are spin-developed for approximately 10 seconds using MF-327 developer. For negative image, after the holographic exposure, the samples are post-exposure baked (PEB) on the hot plate at 120° C for 2 minutes, flood exposed using new aligner (MJB-3) for 3 seconds, and spin-developed for approximately 6 seconds using MF-327 developer. No postbake cycle is performed to eliminate the possibility of pattern degradation because of resist flow.

A uniform grating, either positive or negative image, without a phaseshift can be easily patterned using holographic-exposure technique of a laser beam with appropriate wavelength to expose standard photoresist. However fabrication of a central phaseshifted grating is more challenging. Some methods, which have been demonstrated to obtain the phaseshifted grating based on a holographic-exposure technique, utilize either the use of a patterned retardation plate [1] or simultaneous use of two photoresists, [2] positive and negative photoresists. The grating fabrication incorporating central π-phaseshift with two photoresists requires the patterning of positive resist and negative resist side-by-side. This could results in the photoresist mixing and the alignment is very difficult.

The method, which I have used to pattern 2^{nd}-order grating with central π-phaseshift is using only one photoresist (the image reversal method). [3] This method utilizes a property of the photoresist which can be made to behave as either positive resist or a negative resist by appropriate chemical treatment [4]. The challenge with this method, when only a single photoresist (i.e. AZ5206) is used, is the processing of the positive-image patterns must not disturb the photoresist property for the negative-image patterns and vice versa. In order to that, germanium, which is deposited on the top grating-exposed photoresist, is used for two reasons: as a hardmask to protect the exposed photoresist underneath it and as light blocker to reflect UV light during flood exposure.

The right thickness of germanium is critical to the success of patterning the grating with central π-phaseshift. If the germanium thickness is too thin, it can not block the light during flood exposure. On the other hand, when germanium is too thick, a photoresist on the top of Ge could peel off, thus creating broader transition regions, which are the interface areas between the positive-image patterns and negative-image patterns. A good range of the germanium thicknesses is between 40 nm to 60 nm. The other critical step in patterning the grating with π-phaseshift is the means of the germanium is deposited. It is very important that the holographic-exposed photoresist is not disturbed during germanium deposition. It is found that e-beam (metal) evaporator is not suitable for depositing germanium because of the high-energy germaniums, which react with the grating-exposed photoresist and form a compound that hard to etch on later processing. The best way to deposit germanium is using thermal evaporation. By slowly increasing the drive current, a uniform germanium layer could be deposited without forming the compound layer. However, due to a heating on a tungsten boat, which could exposes the photoresist, the ability to control the drive current to heat up the tungsten boat is very important. The recipe to deposit germanium by thermal evaporation is given in the Appendix A.

The next two figures describe how the grating with central π-phaseshift is fabricated. Figure 5.1a shows the grating-exposed photoresist using the holographic system on the top of GaAs-cap layer. The period of the grating, Λ, is around 2985 Å with the photoresist thickness of 800 Å. Later germanium is deposited to form a 50 nm-thick layer using thermal evaporation (Fig5.1b). The right thickness of the Ge film can be examined visually by looking at a color of the Ge film. The Ge-film color should look metallic gray looking at normal of the surface and transparent gold looking at 45° from the normal of the surface. Pure AZ5206 photoresist is then spinned at speed of 4000rpm for 30 seconds on top of Ge film to get about 0.6μm thickness (Fig. 5.1c). Using mask 1 (phaseshift mask) and new aligner (MJB-3), the photoresist is patterned. Half of the region, which the photoresist has been exposed and developed and the Ge film has been wet etched, is patterned to get positive-image grating (Fig 5.1d). The other half of the region is then patterned to get negative-grating image.

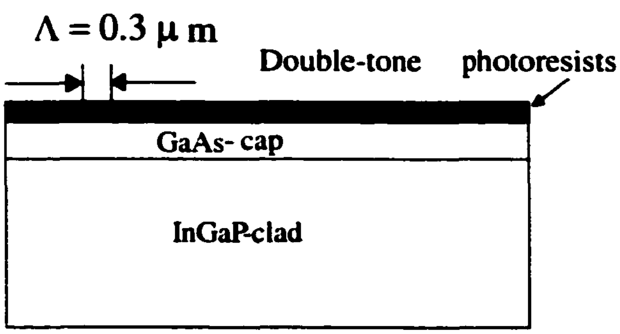

(a)

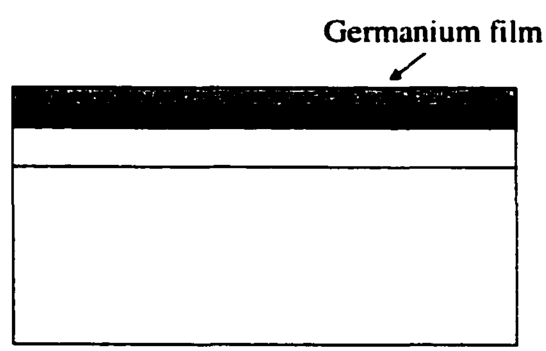

(b)

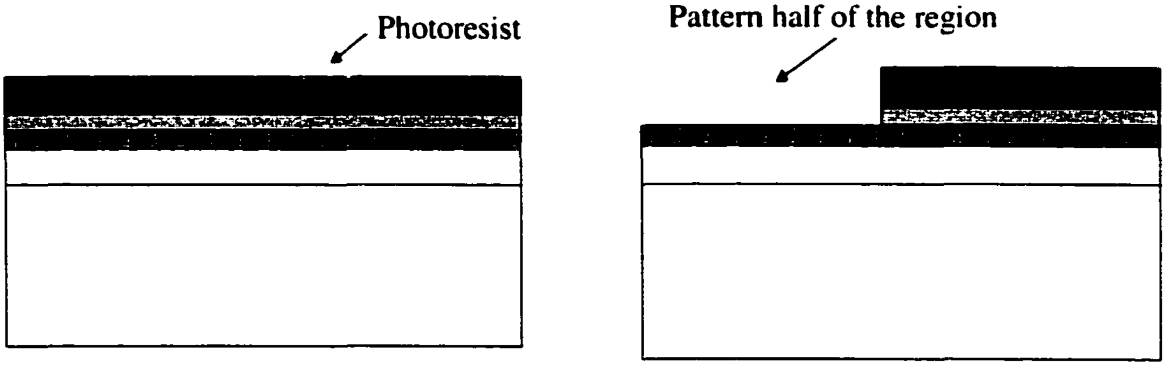

(c) (d)

Fig. 5.1. The processing steps to divide a region of the grating-exposed photoresist. One half of the region will be patterned to get positive-image gratings and the other half will be negative image-gratings.

Fig 5.2 shows the fabrication steps for patterning the negative-image grating. The photoresist on top of the Ge film is stripped, in the same time, as the positive-image resist is developed (Fig. 5.2a). The next step is to deactivate the positive-image resist so it does not react with the later processing for obtaining the negative-image resist. The first step to deactivate the positive-image resist is by flood expose for 3 seconds with MJB-3. Then the sample is immersed in the chlorobenzene for 15 minutes. The purpose of the cholorobenzene immersion is to make the surface of the photoresist becomes harder (Fig 5.2b). The chlorobenzene immersion is commonly used for metal lift-off. Later the remaining of the Ge film is etched away. To complete the deactivation of positive-image resist, the sample is baked on the hot plate at 120°C for 2 minutes (Fig. 5.2c). The whole sample area is flood exposed one more time to pattern the negative-image resist. Fig 5.2d shows the positive-image resist on one half of the region and ready-to-develop resist on the other half of the region to become negative-image resist.

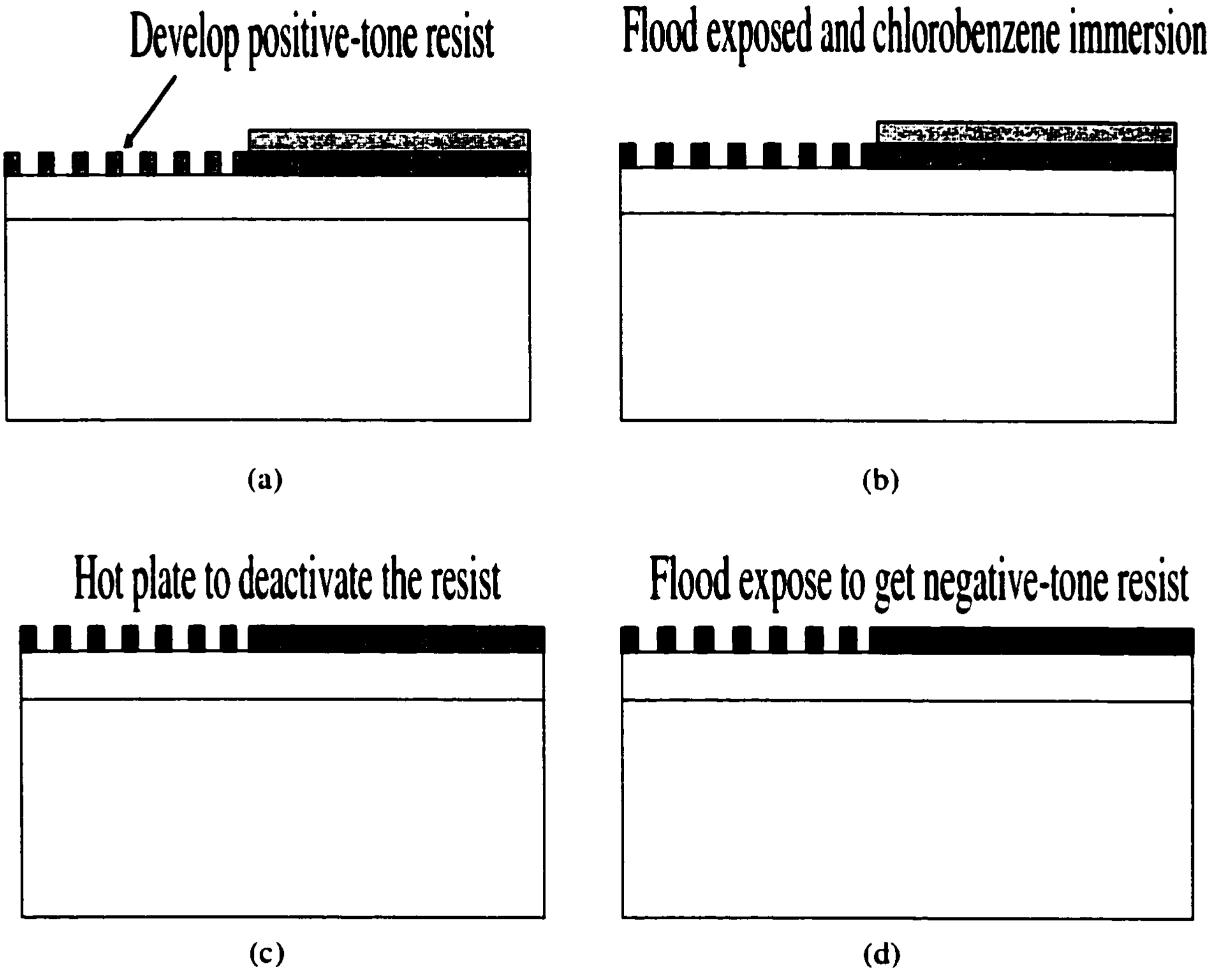

Fig 5.2. The continuing process from Fig. 5.1 to pattern negative-image gratings on the other half of the region.

After a spinned develop for 7 seconds with MF327 developer, the negative-image grating is patterned on the other half of the region (Fig 5.3). The sample now has 2nd-order grating with central phaseshift. The phaseshift is half of the grating period which corresponds to the π-phaseshift for 2nd-order grating.

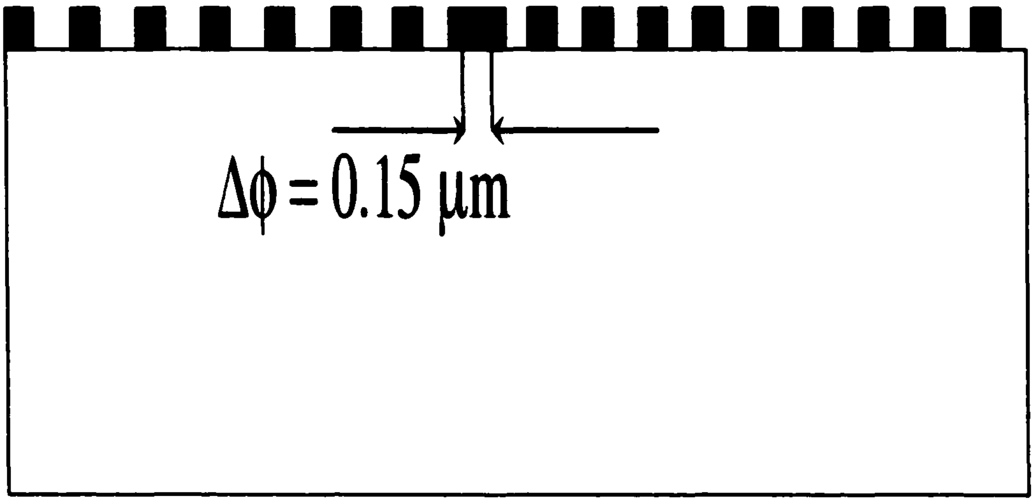

Fig 5.3. A finished grating fabrication, which shows 2nd-order grating with a central π-phaseshift.

5.2 Photoresist Images Patterned by The Image Reversal Method

After several iterations were done to calibrate all the fabrication steps, photoresist images with a large pattern are fabricated using the procedure described in the previous section. Figure 5.4 shows the image of the positive- and negative-tone resists, which have a pattern of 4 μm-core width and 15 μm-side widths. It is clearly seen that one half of the region (positive-tone resist) has an opposite tone compared to the other half of the region (negative-tone resist). The interface of the two images shows a sharp change which indicates a very small transition region. This step is used to calibrate the processing parameters. Consequently the π-phaseshifted grating could be done with the same procedure with some adjustments and calibrations.

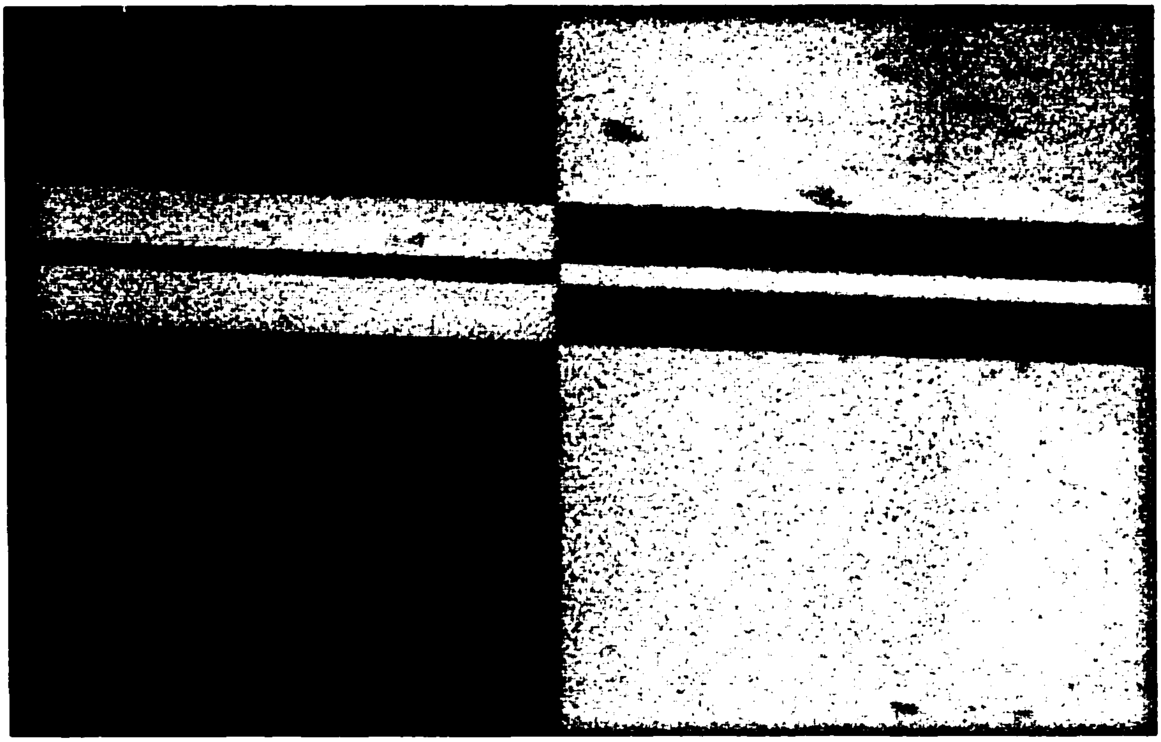

Fig. 5.4 The photoresist image of large patterns showing positive-tone resist on one half of the region and negative-tone resist on the other half of the region.

The next step is to actually pattern the 2^{nd}-order DFB with central π-phaseshift grating. Fig. 5.5 shows that π-phaseshifted gratings have been successfully patterned using the image reversal method. The dark lines, which are the peaks of the gratings, on one half of the region meet the white lines, which are valleys of the grating, on the other half of the region. The transition region is very small, which indicate abrupt change in the photoresist tone. This calibrated fabrication technique has smaller, hence better, transition regions than the previous technique [3]. Fig 5.6 shows the enlarged image of Fig 5.5. From Fig 5.6, the transition region can be measured to be less than 0.15 μm. The transition-region lines of Fig. 5.6 are perpendicular to the grating lines. This scheme is not going to be the final grating pattern on the real devices. For the 2^{nd}-order DFB surface emitter with a central π-phaseshift, the transition-region lines are parallel to the grating lines.

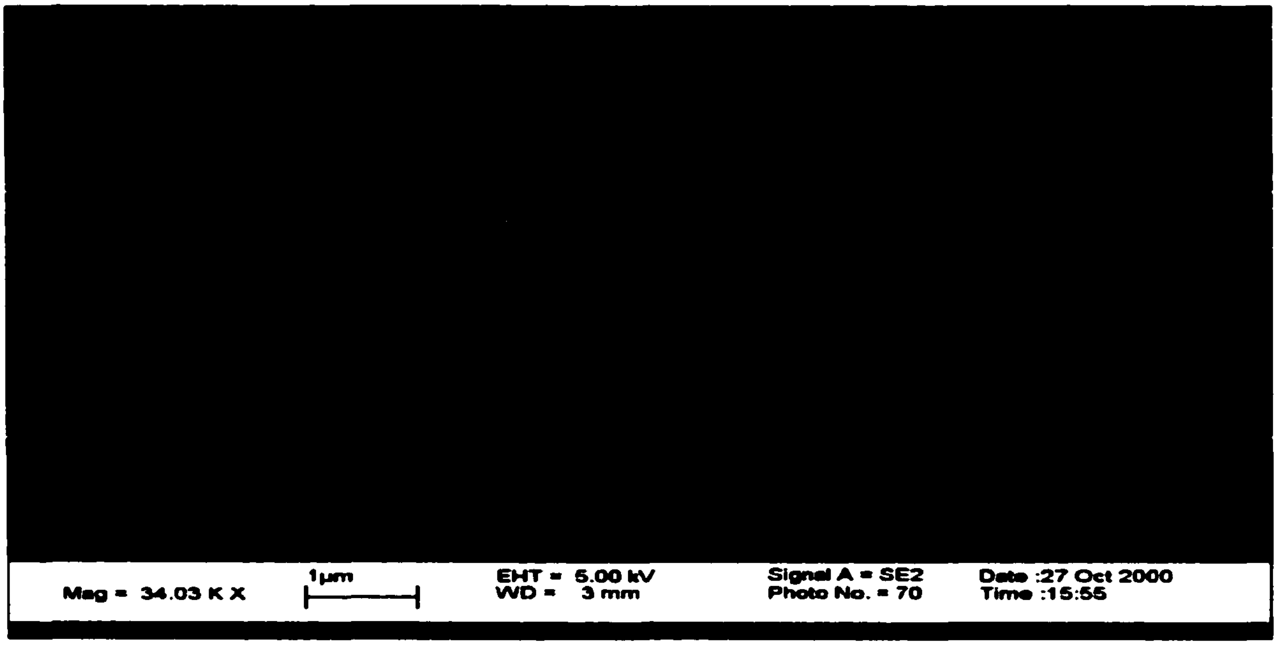

Fig. 5.5 The SEM image showing the grating pattern by the image reversal method. The dark and the white lines are the peaks and the valleys of the grating, respectively. The dark lines on the left image meet the white lines on the right image indicating reversed tones.

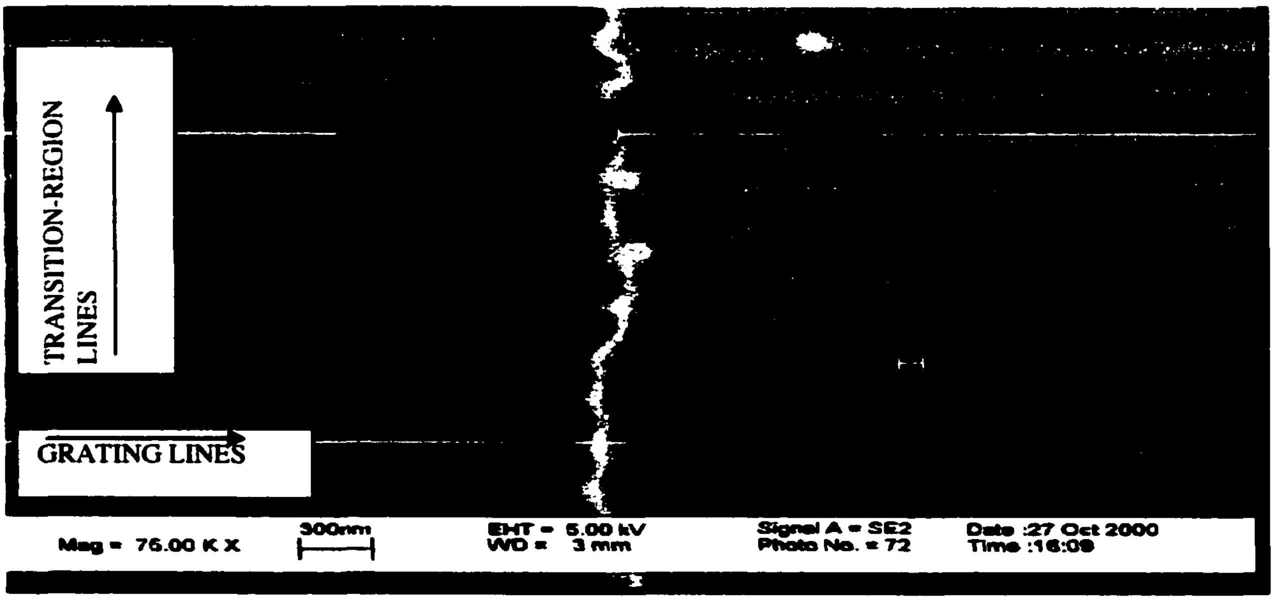

Fig. 5.6 The SEM picture of the enlarge image from Fig. 5.5. The transition regions is less than 0.15 µm. The grating lines are perpendicular to the transition-region lines in the grating pattern.

5.3 Second-Order GaAs Grating Incorporating Central π-Phaseshift Grating.

The previous section shows the photoresist images, which have the grating lines perpendicular to transition-region lines, patterned by the image reversal image method. This section will show the final grating patterns, in which the grating lines are parallel to the transition-region lines, used for the real devices. Once the (grating) photoresists have been developed, the grating is transferred into GaAs layer. To improve the adhesion of the photoresist into the GaAs layer, hence better grating uniformity, transition layer (i.e. Si_3N_4) is deposited between photoresist and the GaAs layer. Therefore the grating pattern is first transferred into the Si_3N_4 by dry etching, then into the GaAs layer by wet-etching.

The most common method for grating pattern transfer into Si_3N_4 is by dry etching, either reactive ion etching (RIE) or chemically-assisted ion beam etching (CAIBE). However, a challenge is imposed in this grating pattern transfer since the holographic-exposed photoresist is very thin (80 nm). A good-quality grating-transfer pattern is commonly required a much thicker photoresist (10x) compared to the Si_3N_4 thickness (40 nm used in this research). An etching rate of Si_3N_4 is slower than the stripping of the photoresist by NF_3 plasma for certain duty cycle of a grating. This could result in a bad, or even failed, grating transfer. It becomes more complicated when the grating profiles of positive-tone resist is different from the negative-tone resist, which results in a difference of the etching rate of Si_3N_4 for positive- and negative-tone resists. In the early work, some grating-transfer patterns can only be successfully transferred either from positive- or negative-tone resist, but not from both of them. A lot efforts have been done to obtain the same grating profile in the photoresist from both the positive- and negative-tone resists.

The grating patterns transferred by wet etching techniques impose other fabrication challenges regarding photoresist exposure: (1) because the adhesion of the photoresist to the substrate must be sufficient to withstand the agitation and surface tension effects associated with the development and etching steps. These issues do not necessary apply when the transition layer (i.e. Si_3N_4) is deposited between the photoresist and the substrate to reduce the adhesion problem; (2) the substrate surface must be free of imperfections that could inhibit uniform photoresist application and disrupt the holographic interference pattern; (3) the gratings need to be uniform on all across the surface of the substrate. This could be the biggest challenge since it could be very difficult to have the uniform grating on the positive- and negative-tone photoresists.

The potential problems associated with nonuniform (photoresist) gratings across samples were my greatest concern. Submicron lines of photoresist across samples as large as one inch diameter, which undergo different processes for patterning positive- and negative-tone resists, seemed hard to be precisely controlled. Different regions of photoresist are experiencing different chemical and environment exposures. The detail fabrication processes to obtain the positive- and negative-tone resists are given in Appendix A. To ensure a good grating uniformity across the wafer on positive and negative-tone resists, calibrations of processing parameters on the test samples are always performed before processing the real wafers.

Fig 5.7 shows an SEM photograph of the fabricated GaAs grating with π phaseshift by using positive- and negative-tone resists. [5] The uniformity across the sample on the positive- and negative-GaAs images is pretty good. The phaseshift, which is measured from peak to peak at the center region, is a half of the period, hence π-phaseshift. A transition regions from other samples are observed, but its width is not that relevant as long as the two grating regions are out-of-phase with each other. That is, the grating phaseshift does not necessarily have to be π; it can be an odd number of π, since the in-plane propagating (guided) light is unaffected by it.

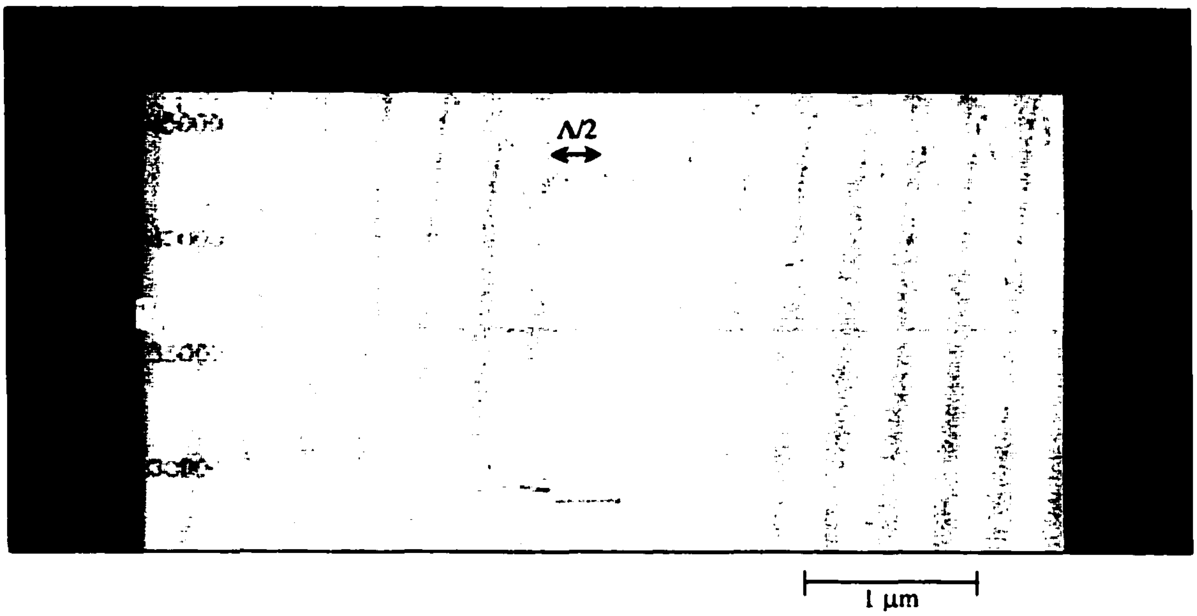

Fig 5.7. Scanning electron micrograph and its intensity profile showing a π phase-shifted GaAs grating fabricated by using the image-reversal method on one photoresist [5]. The period of the grating is 0.3 μm.

Chapter 5 References

[1] F. Koyama, Y. Suematsu, K. Kojima, and K. Furuya, "1.5μm Phase Adjusted Active Distributed Reflector Laser for Complete Dynamic Single-Mode Operation," Electron. Lett. **20**, 391 (1984).

[2] K. Utaka, S. Akiba, K. Sakai, and Y. Matsushima, "λ/4-shifted InGaAsP/InP DFB Lasers by Simultaneous Holographic Exposure of Positive and Negative Photoresists," Electron. Lett. **20**, 1008 (1984).

[3] W.K. Chan, J. Chung, R.J. Contolini, "Phase-Shifted Quarter Micron Holographic Gratings by Selective Image Reversal of Photoresist," Appl. Optics **27** (8), 1377 (1988).

[4] M. Spak, D. Mammato, S. Jain, and D. Burham, "Mechanism and Lithographic Evaluation of Image Reversal in AZ5214 Photoresist," AZ Corp.

[5] G. Witjaksono, S. Li, and D. Botez, "High-efficiency, Single-lobe Surface-Emitting DFB/DBR Lasers", Paper TuA3 at the 14th IEEE LEOS Annual Meeting, 12-15 Nov. 2001, San Diego, CA.

Chapter 6

Single-Lobe Operation from Surface-Emitting, 2^{nd}-Order Distributed Feedback Lasers with Central π-Phaseshift Grating

Once, the grating with π phaseshift in the GaAs-cap layer is patterned, the single-element (i.e. ridge-guide) surface-emitter is fabricated.

6.1 Single-Element (i.e. Ridge-Guide) Device.

Before discussing the fabrication of single-element surface emitter, it is useful to understand the basic properties of the single-element waveguide. In the single-element (positive) guide, the effective core index, n_o, is higher than the lateral cladding index, n_l. Using the effective index approximation, the fundamental lateral mode is shown is Fig 6.1. Higher order modes can be supported by this structure depending on Δn_{eff} and the core width. Laterally-confined modes exist for propagation constants β_i and reflected angles θ_i^{core} within the range:

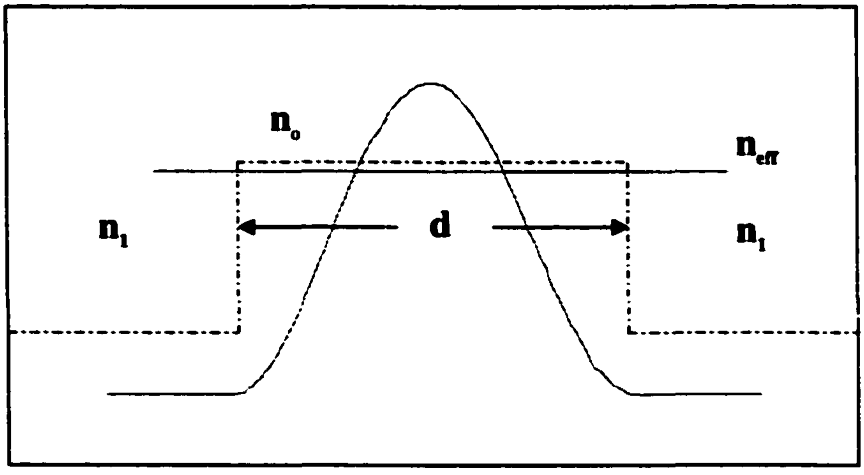

Fig. 6.1. Index profile for single-element guide. The field intensity curve and its effective index for the fundamental mode are shown.

$$n_o k > \beta_o > \beta_i > \dots \beta_N > n_1 k \qquad [6.1]$$

$$0 < \theta_o^{core} < \theta_1^{core} < \dots < \theta_N^{core} < \theta_c^{core} \qquad [6.2]$$

where the N^{th} mode is the highest-order confined mode and θ_c^{core} is the angle at which a mode reaches cutoff and radiates energy into the low-index lateral cladding regions.

Within the range specified by Eqn. 6.1, β_i can assumed only discrete values satisfying the following eigenvalue equation, obtained by requiring that the fields obey the appropriate boundary conditions at the lateral interfaces:

$$\tan \kappa_i d = 2\kappa_i \delta_i / (\kappa_i^2 - \delta_i^2) \qquad [6.3]$$

where d is the core width. The parameters κ_i and δ_i are defined as:

$$\kappa_i = (n_o^2 k^2 - \beta_i^2)^{1/2} = n_o k \sin\theta_i^{core} \qquad [6.4]$$

$$\delta_i = (n_1^2 k^2 - \beta_i^2)^{1/2} \qquad [6.5]$$

In Fig 6.2, the propagation constant κ_i is shown from a ray-optics perspective. For the i^{th} confined mode the propagation constant can be expressed as:

$$\beta_i = n_o k \cos\theta_i^{core}$$

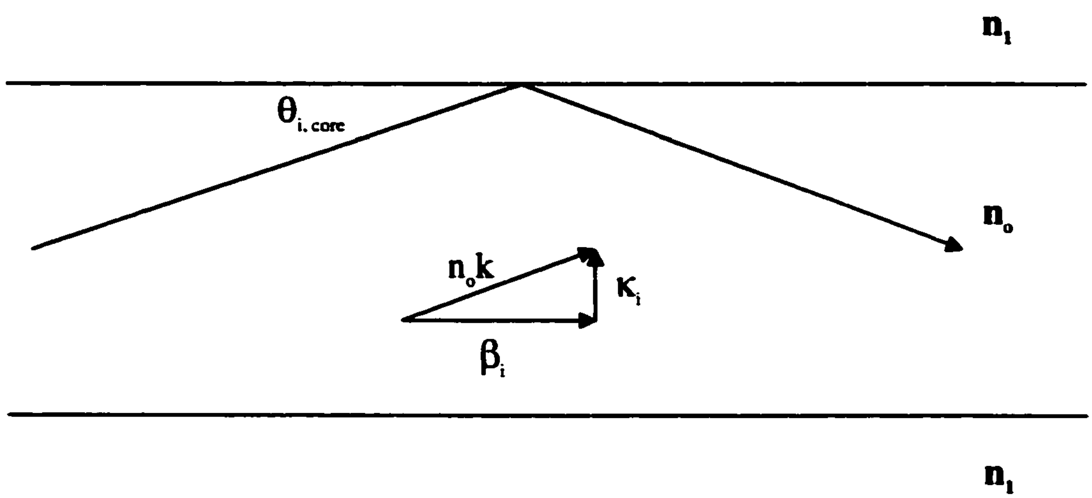

Fig. 6.2 Ray-optics indicating total internal reflection.

For each β_i satisfying Eqn. 6.1, the ray suffers total internal reflection at an angle θ_i^{core} at both lateral cladding interfaces so that the no power can be transmitted into the surrounding media. In this case, the optical field is evanescent in the lateral cladding regions and δ_i is imaginary. As Δn_{eff} decreases, each β_i (θ_i^{core}) correspondingly decreases (increases). Eventually, θ_i^{core} reaches the cutoff value θ_c when the ray is no longer totally reflected at the interfaces. The field in the cladding layers then becoming sinusoidal and energy radiates away from the core, leaving *N-1* confined modes.

In our ridge-guide design, the effective index difference (Δn_{eff}) is 6×10^{-3}. To achieve single-spatial mode operation, the device must be designed such that all modes other than the fundamental mode are pushed beyond cutoff. This can be achieved by setting the core width to be 2.5 μm.

6.2 Fabrication of Single-Element Surface Emitter

The structure has a GaAs buffer layer, followed by a 1μm-thick n-doped (5×10^{17} cm^{-3}) $Al_{0.54}Ga_{0.46}As$-cladding layer, a 110nm-thick $Al_{0.42}Ga_{0.58}As$ lower optical-confinement layer and a 10nm-thick GaAs-transition layer. Two 7nm-thick InGaAs quantum wells separated by a 20nm-thick GaAs barrier layer form the active region. Next are 10nm-thick GaAs-transition layer, a 110nm-thick $Al_{0.42}Ga_{0.58}As$ upper optical-confinement layer, a 200nm-thick p-doped (5×10^{17} cm^{-3}) $Al_{0.54}Ga_{0.46}As$ and a 200nm-thick p-doped (5×10^{17} cm^{-3}) InGaP cladding layer, and a 100nm-thick p^+(2×10^{19} cm^{-3})-GaAs cap layer patterned with 3000Å grating period incorporating a central π-phaseshift grating.

The requirement of unannealed metal on p-side for the single-element surface emitter determines the processing sequence as follow: first, patterning the ridge-guide on the p-side; lapping and polishing on the n-side, followed by n-side metal and an antireflective (AR) coating; finally opening the window for the contact and depositing p-metal.

Fig 5.7 Shows the GaAs grating incorporating a central π-phaseshift. The ridge-guide surface emitter is going to have a grating region composed of a positive GaAs grating on one half of region and the negative GaAs grating on the other half, which provides a π-phaseshift in the center of the longitudinal direction (Fig 6.3). The transition region, where the π-phaseshift is, is the area between the positive and a negative GaAs-grating regions. The alignment of the ridge mask on the GaAs grating is done by precisely placing one of the transition region on the edge of the wafer.

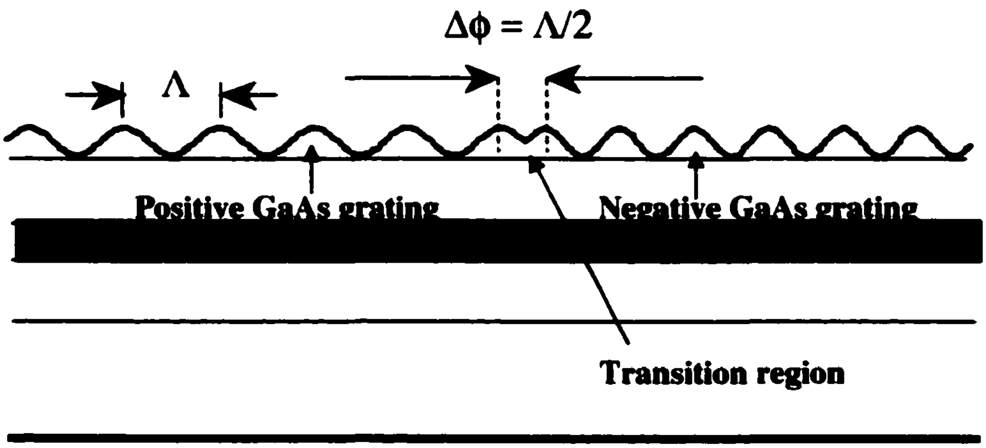

Fig. 6.3 A cross-section of the device showing the positive GaAs grating on half the region and negative GaAs grating on the other half.

Before patterning the ridge-guide on the wafer, SiO_2 with the thickness of 1000 Å is deposited on the top of the GaAs grating. The purpose of this SiO_2 is two-fold: as a hardmask when etching the ridge guide and as a protection layer for GaAs grating for later processing. As soon as the GaAs grating is covered by SiO_2, photoresist (PR1827) is spinned on the wafer and then patterned to get 2.5-μm ridge waveguides. Later the SiO_2 and the semiconductor layers (0.1μm GaAs-cap and 0.2 μm InGaP-cladding layers) are wet-etched using the recipe given in the Appendix B (Fig 6.4a). Without postbake and stripping the photoresist, the wafer is placed in a PECVD chamber to deposit SiO_2 with a thickness of 2000 Å. A thicker SiO_2 is used here to eliminate the problem of driving the current outside of stripe width due to the misalignment. Later, the thick SiO_2 on top of photoresist is lifted-off using acetone and PR stripper (Fig 6.4b)

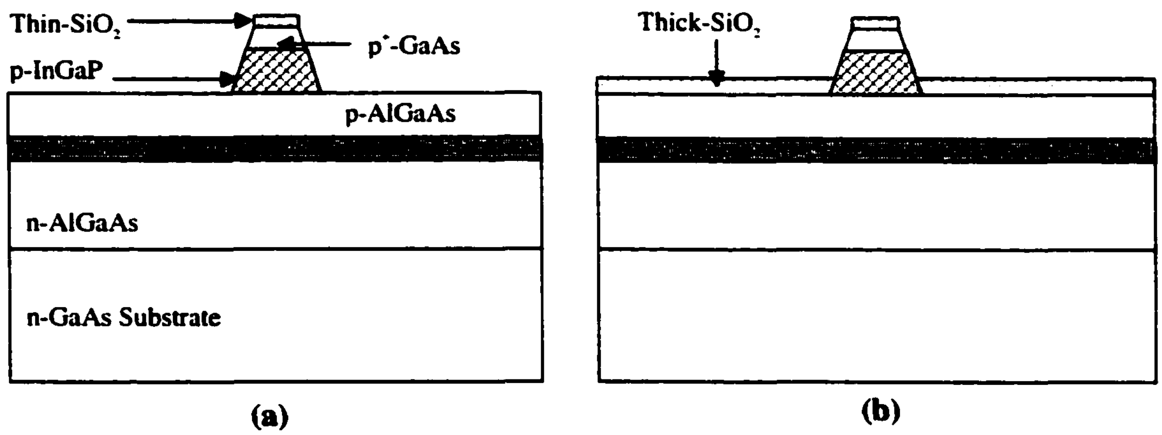

Fig 6.4 A cross-section of the ridge guide after (a) etching the semiconductor layers; (b) SiO_2 lift-off.

The wafer is then lapped to a thickness of 150 μm and polished in order to obtain flat and shiny surfaces. The photoresist (PR1827) is then spinned and patterned. The n-metal, which consists of 200Å-Ge/1000Å-AuGe/300Å-Ni/3000Å-Au is deposited using e-beam evaporation. A metal lift-off is then performed to make windows for light emission. For the lift-off, the wafer needs to be immersed overnight in PR stripper to get good patterns. The wafer is now ready for annealing. The annealing temperature is 375°C for 30 seconds.

Next step is coating the window on the n-side with AR coating. The n-side of the wafer is spinned again with PR1827 and patterned. After overnight pumping in the dielectric (e-beam) evaporator, an antireflective coating, which consists of 180Å-Al_2O_3/270Å-Si/1500Å-Al_2O_3, is deposited on the n-side. AR-coating lift-off is then performed using warm PR-stripper. This step concludes the processing step on the n-side. The wafer now has contact metal and a light-emitting window with AR coating on the n-side and a GaAs-grating on the p-side. Figure 6.5 shows a 3-D picture of the wafer up to this step.

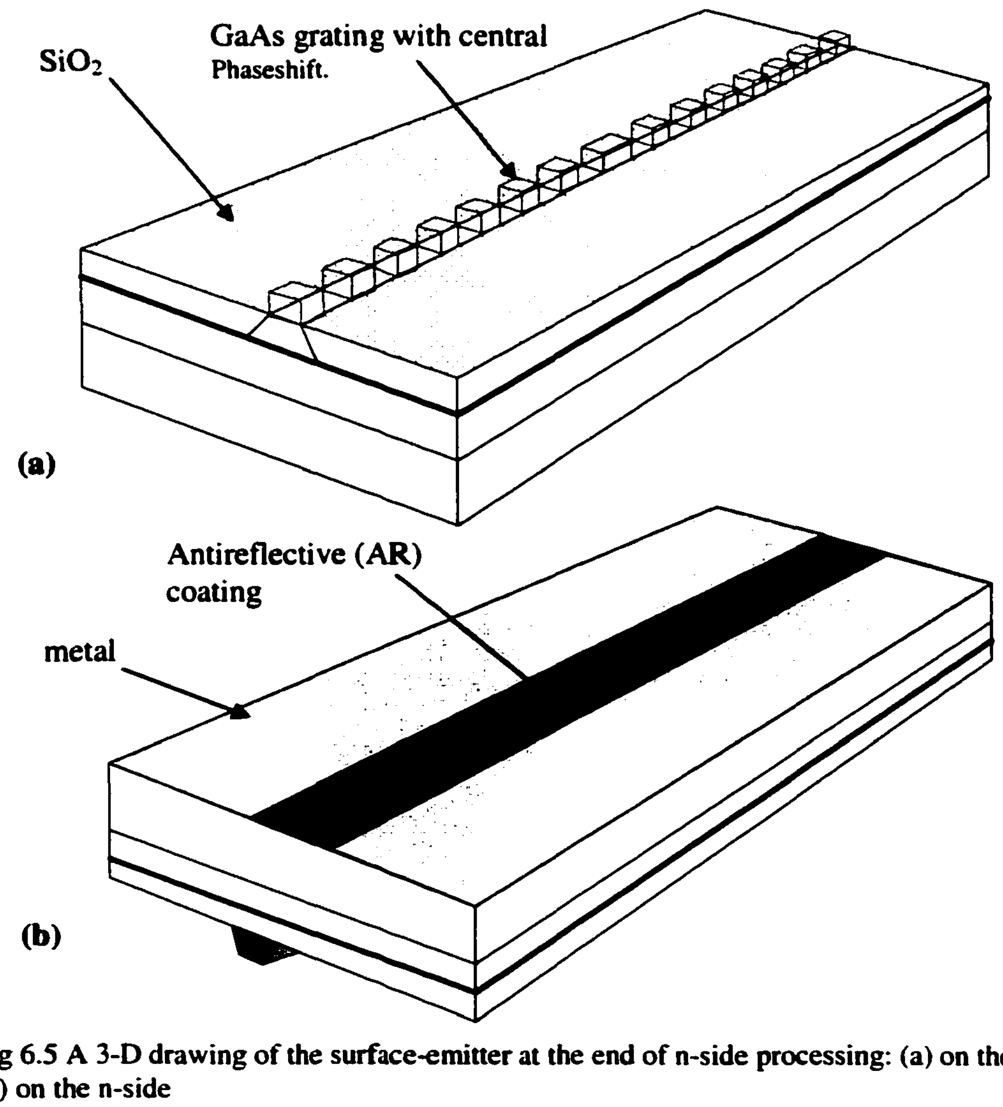

Fig 6.5 A 3-D drawing of the surface-emitter at the end of n-side processing: (a) on the p-side; (b) on the n-side

Since Au on the p-side is intended to reflect all the light, the p-side metal is not annealed. Therefore the Au on the p-side is "shiny". The primary problem when only Au is used for metal contact is a poor electrical contact due to the poor adhesion of Au to the SiO_2. On the other hand, depositing conventional p-side metals (250Å-Ti/500Å-Pt/2000Å-Au) will introduce a large metal loss, which would result in large threshold gains and very low efficiency. A compromise approach is to use only thin Ti (20Å) and Pt (20Å) layers before Au, but the adhesion to SiO_2 is still a problem. The best approach to get a good contact and low metal loss is by using a little bit thicker Ti (40Å) and Au but without Pt. Appendix B describes the fabrication steps in detail. Figure 6.6 shows a single-element surface emitter after the p-side metallization.

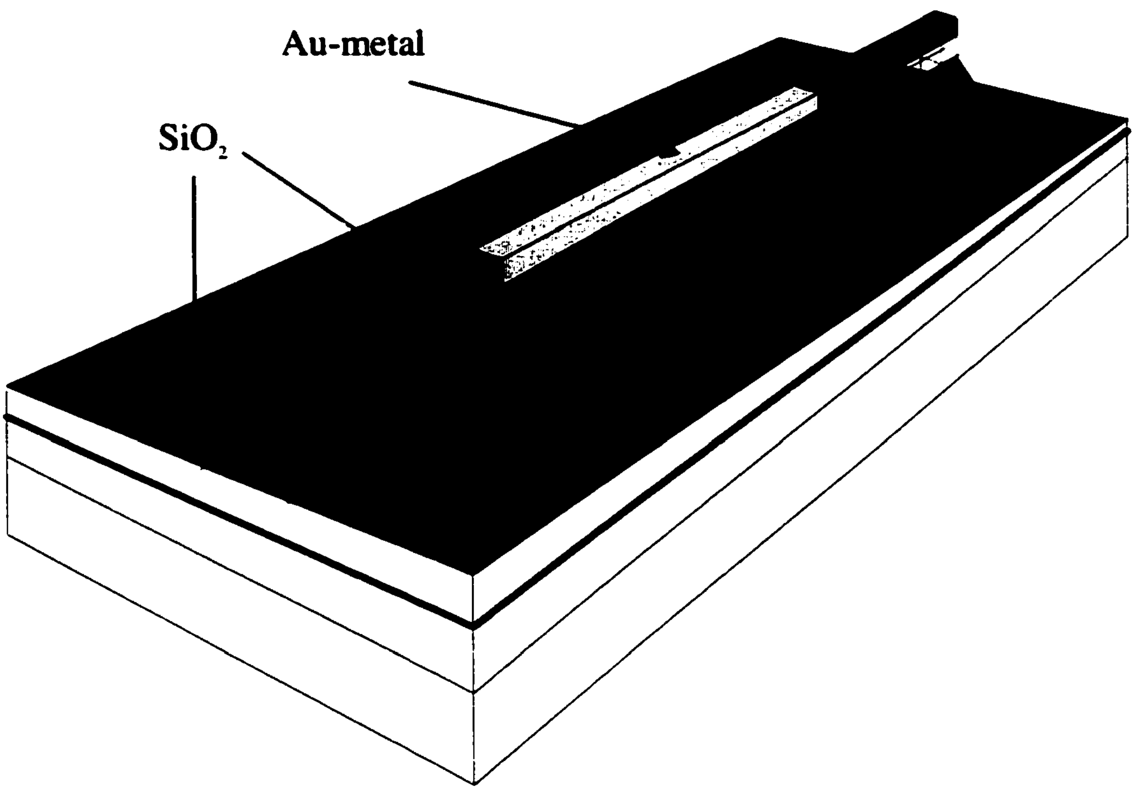

Fig. 6.6. Single-element surface emitter after p-side metallization.

The wafer is then cut into bars for facet coating. The length of the bars is 1500μm, which consist of a 500μm-long DFB region, and 500μm-long DBR regions. Antireflective coatings are deposited on both sides of the edges using a dielectric (e-beam) evaporator. This coating has a reflectivity of less than 1% at 965nm. Finally, the bars is cut into devices, which are ready for testing.

6.3. Experimental Results

After several iterations were done to calibrate all the fabrication steps, a device was fabricated and tested. Broad-area (BA) devices (100μm-wide stripes) from the same wafer were fabricated to obtain the lasing wavelength, which is necessary to determine the grating period. The period is patterned to have a Bragg wavelength of 965 nm, which is 15 nm away from lasing wavelength. The threshold current was 350 mA, and the efficiency was 110 mW/A (from each facet) for this 1000μm-long BA edge-emitter devices. The next step was to fabricate single-element (ridge-guide) edge emitters to calibrate the p-side metal. As mentioned in the previous section, a good p-side metal contact is required and, in the same time, not producing a high metal loss. This ridge-guide edge emitters were fabricated by the same procedures as the surface emitters but without a window on the n-side. A good IV (current-voltage) curves together with good threshold current of 25 mA from this ridge-guide edge emitters indicate good metal contact. The next step is to make single-element surface emitters. Appendix B contains the detailed recipe for making single-element (i.e. ridge-guide) surface emitters.

After applying AR coatings on both cleaved sides for surface emitters, the chips (1500 μm long) were tested. The first testing was the IV curve. The test setup used is shown in Fig. 6.7.

The testing results would indicate whether the chips have good metal contacts. A typical IV curve for good-metal devices is shown in Fig. 6.8. The turn-on voltage for this single-element surface-emitter is about 1.4 V.

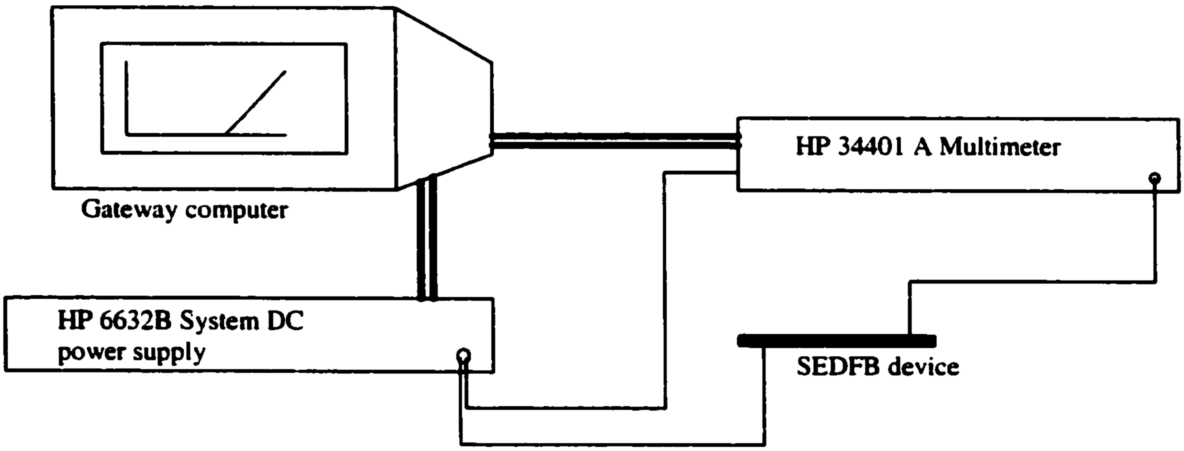

Fig. 6.7 Current-voltage (IV) test setup.

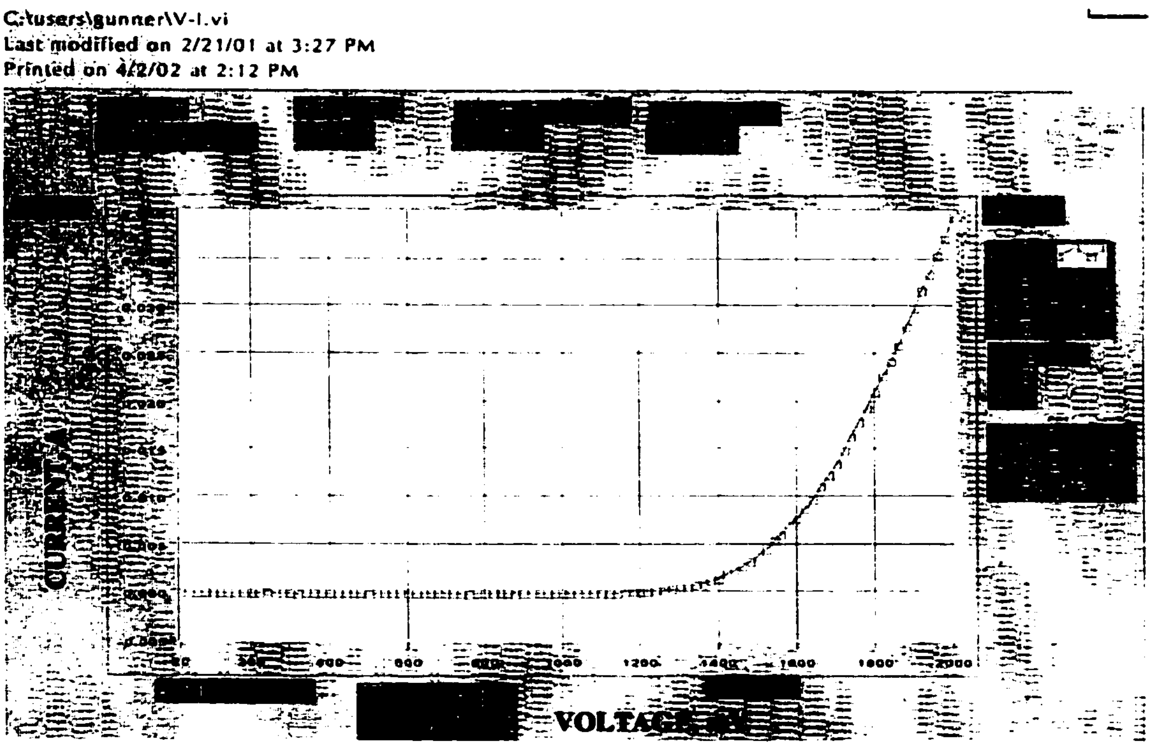

Fig. 6.8 A typical IV curve for good-metal devices.

The MOCVD-grown InGaAs/AlGaAs DQW structure has a 2nd-order GaAs grating, with a central π phaseshift (not shown), which also acts as contact layer (see inset) in the DFB region (500μm long) and extends longitudinally 500μm on both sides (i.e., DBR mirrors). Fig 6.9 shows a bird's eye of the finished device with AR coating on both ends of DBR regions. The radiation is outcoupled through a window in the n-side metal contact.

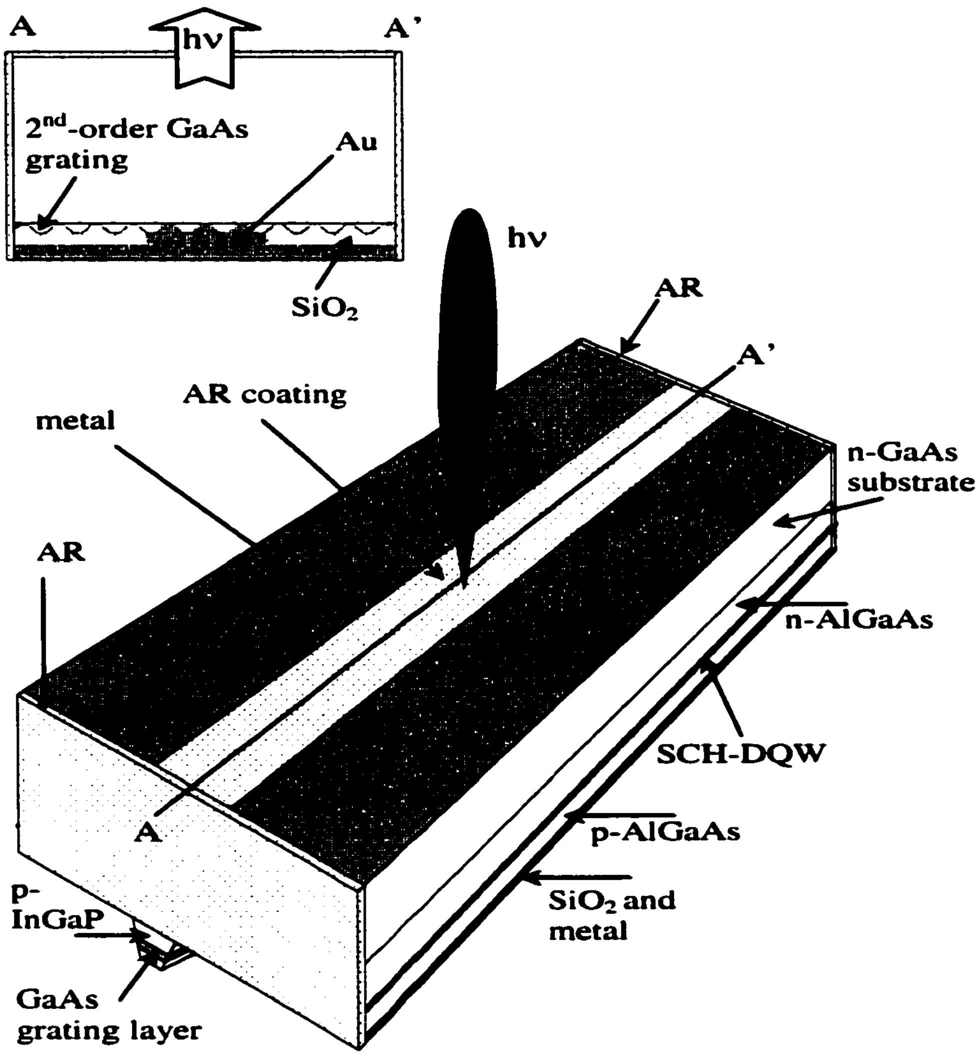

Fig 6.9 The surface-emitting 2nd-order DFB/DBR laser. Inset: longitudinal cross-section: 500μm-long DFB and two 500μm-long DBRs

The far-field beam patterns were measured to find out whether the device operates in the symmetric, antisymmetric or both modes. Fig. 6.10 depicts the setup used to measure the far-field.

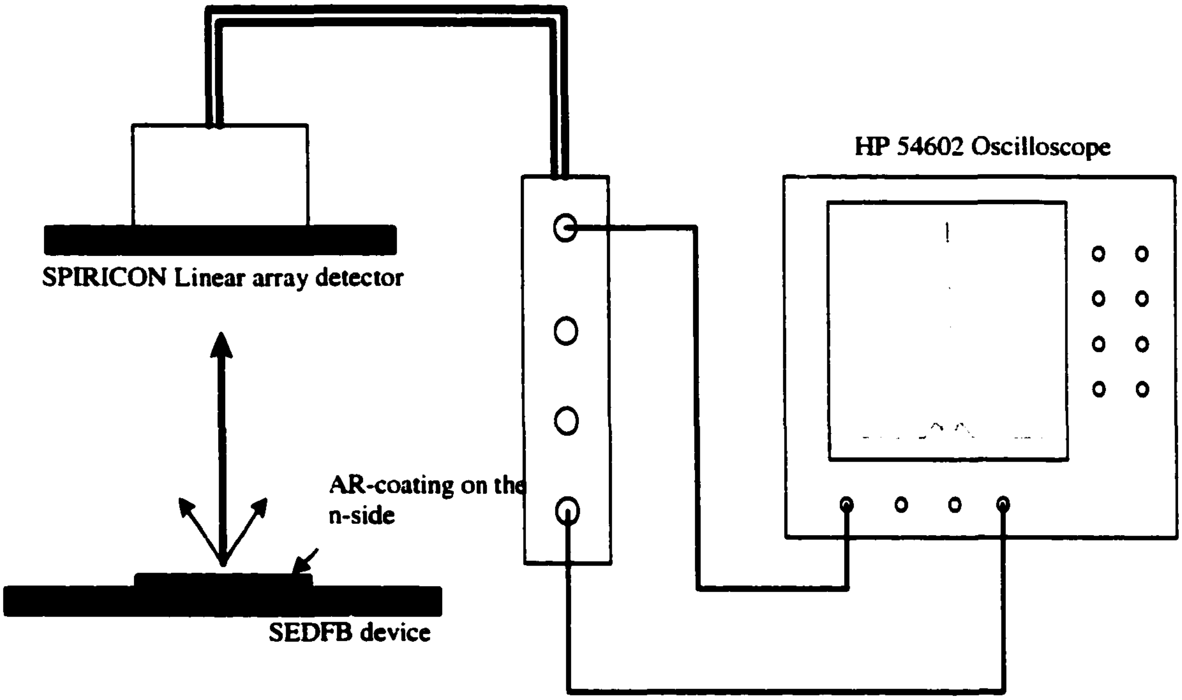

Fig. 6.10. Setup for measuring far-field of surface-emitting DFB laser.

Fig. 6.11 shows the far-field patterns measured in the setup of Fig. 6.10. The figure shows a single-lobe, orthonormal far-field intensity profile. This result proves the concept described in earlier chapters. This is for the first time that single-lobed, orthonormal far-field beam was obtained from a high-coupling (κL), monolithic surface emitter, without introducing any loss mechanism to suppress the antisymmetric mode. This device, with further optimization, can produce high single-mode power levels with high efficiency. Moreover, the far-field beam is diffraction-limited. Theoretically, the FWHM of the far-field is 0.043°. The difference in FWHM compared the experimental results (0.048°) is contributed from the error in measuring the data from plot.

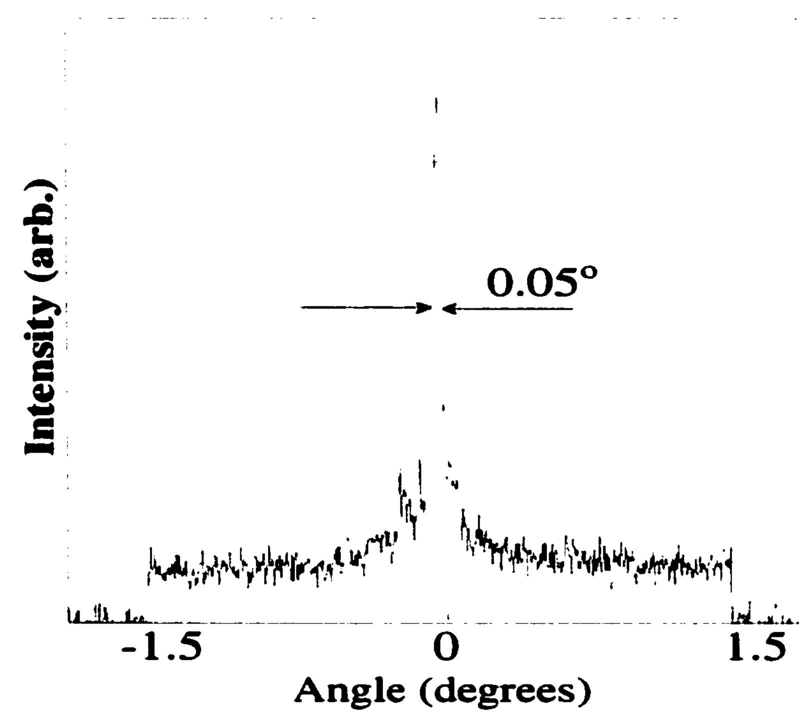

Fig. 6.11 Measured far-field of surface-emitting DFB laser with central grating π-phaseshift

The spectrum is measured from light emitted out of the window on the n-side using a Hewlett-Packard (HP) Optical Spectrum Analyzer (OSA). The test setup used is shown in Fig. 6.12. A pulse generator injects pulse current into the laser (2 kHz repetition rate and 5 μm pulse width), and a multimode fiber connected to an XYZ stage collect the light for input into OSA.

Fig. 6.12 is a printout from OSA showing the spectrum of a surface-emitting 2[nd]-order distributed feedback laser. Clearly, the device lases in a single DFB longitudinal mode. The lasing wavelength is 964 nm, as expected from the grating design.

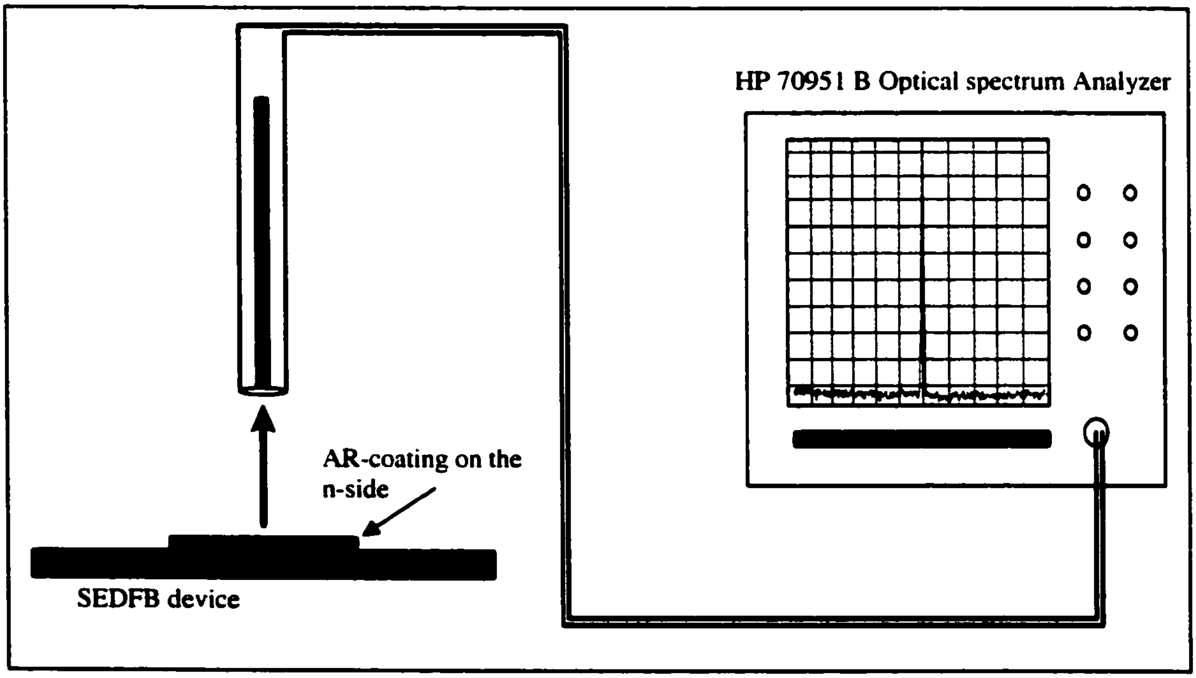

Fig. 6.12 OSA spectrum measurement setup

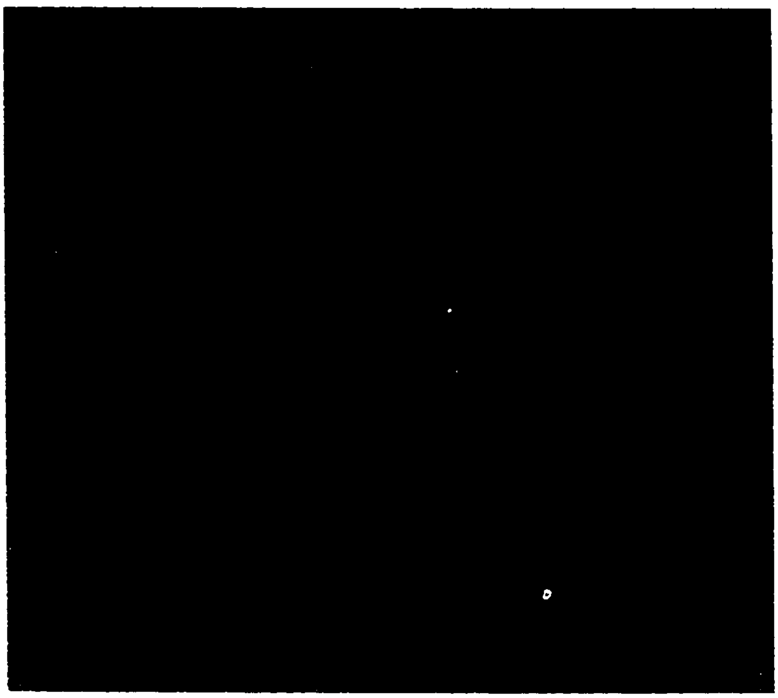

Fig. 6.13 Spectrum of surface-emitting DFB laser with central grating π-phaseshift and AR-coatings for both facets using HP OSA.

The wavelength shifts at rate of 0.3Å/°C, which clearly indicates the DFB action, as opposed to 3Å/°C from the Fabry-Perot modes. A higher resolution spectrometer shows the linewidth to be ~ 0.8Å. Fig. 6.14 shows the shift of wavelength as temperature change from 20°C to 50°C.

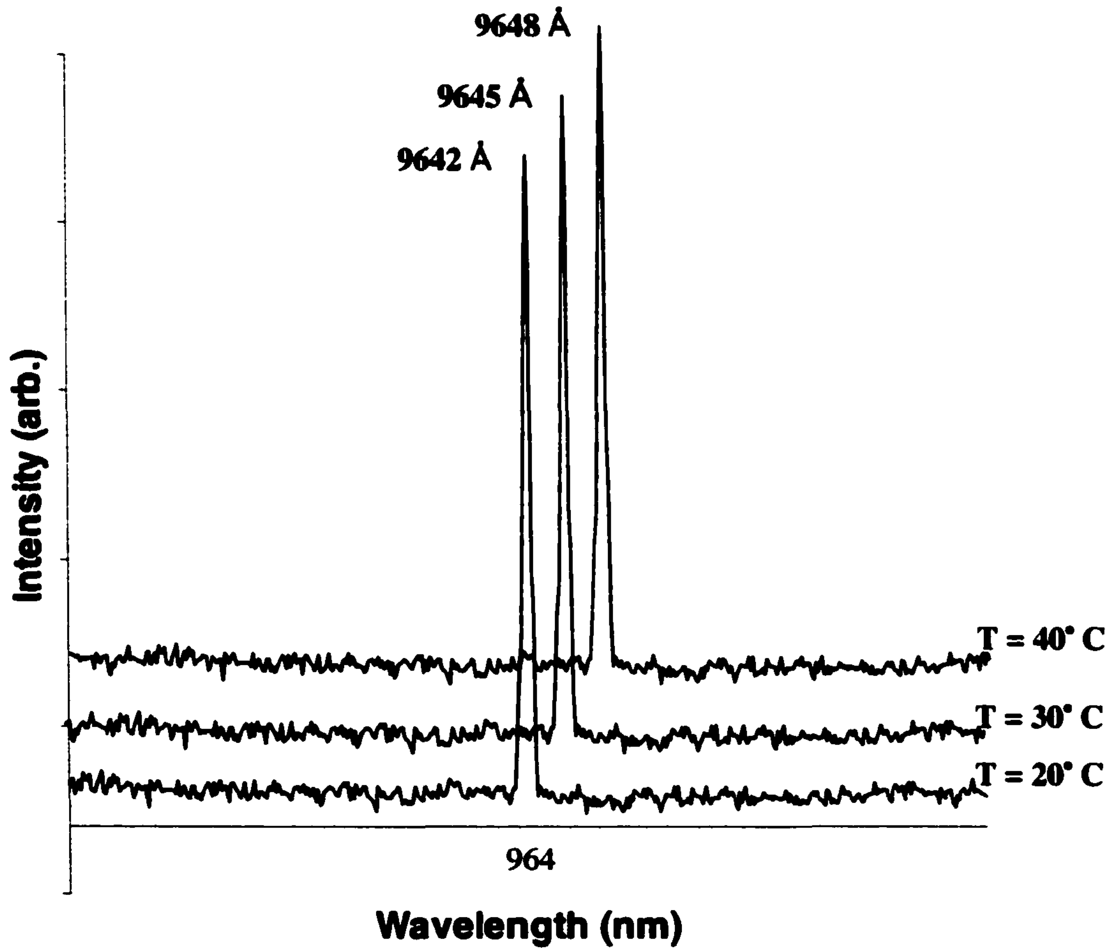

Fig. 6.14 Single-frequency spectrums from surface-emitting 2nd-order DFB/DBR laser with 500μm-long DFB and two 500μm-long DBR regions. The 0.3 Å/°C temperature coefficient confirms DFB action

Chapter 6 References

[1] J. Buss, IEEE J. Quantum Electron., vol. QE-18, pp. 1083, 1982

[2] G. Witjaksono, Shuang Li, and D. Botez, "Single-Lobe, Orthonormal-Beam Surface Emission from 2nd-Order DFB/DBR Lasers with Half-Wave Phaseshift," accepted for presentation at the 18th IEEE International Semiconductor Laser Conference, Garmisch-Partenkirchen, Germany, Sep. 29 – Oct 3, 2002.

Chapter 7

Conclusion and Future Work

7.1 Conclusion

The main objective of this dissertation has been to demonstrate single-lobe, orthonormal surface emission from 2^{nd}-order distributed feedback device, at *no penalty* in efficiency, using a central grating π-phaseshift. This work was organized into smaller tasks, each representing a milestone in the overall project plan.

Device simulation and optimization has been developed using two-dimensional coupled mode theory and the transfer-matrix method. [1] Devices of high degree of guided-field uniformity and large intermodal discrimination, which ensure single-mode operation to high drive levels, have been designed. Differential quantum efficiency (D.Q.E.) values as high as 62% can be achieved for a grating duty cycle of 40%. [2]

Second-order DFB grating fabrication incorporating a central π-phaseshift was realized via interferometric lithography (holographic) systems with image reversal method. [2] Reproducible holographic grating exposure of the substrate was successfully demonstrated using a combination of dry- and wet-etching transfer process. Complete in-house surface-emitting DFB laser fabrication was thus realized.

This work culminated in the successful demonstration of the first surface-emitting, single-mode operation with a single-lobed far-field beam from single-element (i.e. ridge-guide) 2^{nd}-order DFB device incorporating central grating π-phaseshift. [3] The experimental results confirm the theoretical predictions of fundamental lasing in a single-lobe, orthonormal surface emission beam pattern from monolithic 2nd-order DFB devices without built-in loss mechanisms.

7.2 Future Work

The significance of this dissertation lies not necessary in the device results themselves, but in the proof of concept that a central grating π-phaseshift in a 2nd-order DFB/DBR device will result in lasing in a single-lobe, orthonormal beam pattern. It is important to note that the effectiveness of central grating p-phaseshift is not limited to single-element (i.e. ridge-guide type) devices. This concept can be applied to array structures (in the lateral direction) to produce two-dimensional surface emitters. Fig. 7.1 shows the 2-D surface emitter incorporating a 40-element (i.e. 200 μm-wide) resonant optical waveguide (ROW) array structure in the lateral direction and a 2nd-order DFB/DBR grating with central grating π-phaseshift in the longitudinal direction (1200μm-long DFB/DBR regions).

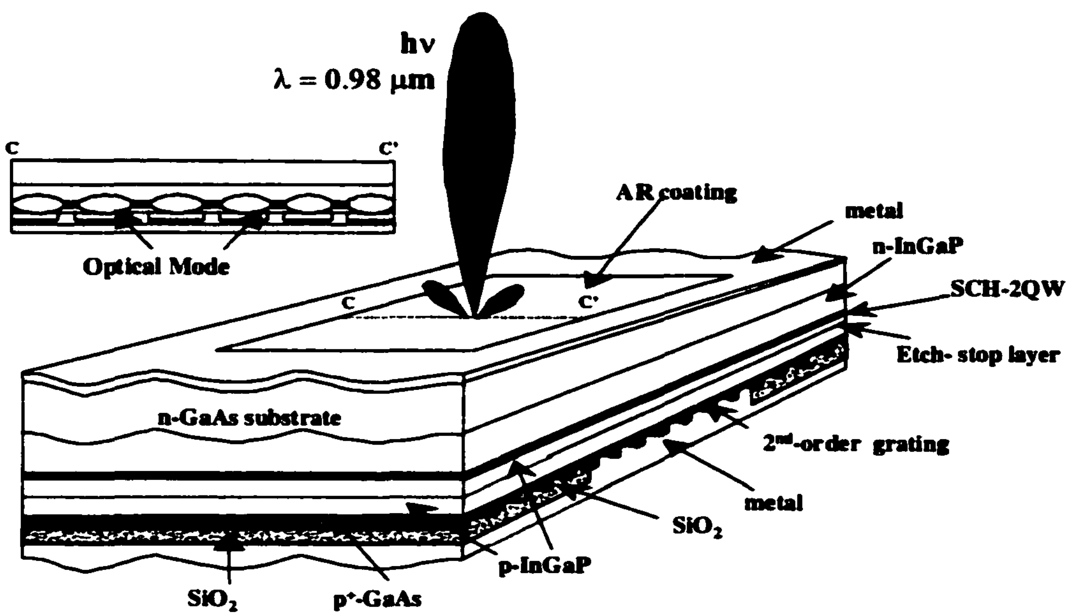

Fig. 7.1 3-D view of antiguided array combined with central-phaseshift DFB/DBR grating structure

The beam aspect ratio is only 6, which allows for easy beam circularization with commercially available anamorphic prism pairs [4]. This 2-D single-mode, single-lobe surface emitters (of horizontal resonant cavity) are ideal high-power (≥ 2W) coherent sources due to the low-aspect-ratio beams as well as the potential for scaling the power via resonant coherent coupling of the sources at the wafer level [5].

Clearly there is work to be done in improving the discrimination and the differential quantum efficiency for these devices. The low discrimination could results from the combination of both the reflection from both facets, which induces the excitation of Fabry-Perot modes, and metal loss due to Ti deposition in the grating region. To completely suppress reflections from the cleaved chip ends, absorbing material (InGaAs) should be introduced (via etch and regrowth process) at the DBR-reflector ends. This measure prevents disturbing lasing in the DFB (active) region due to back reflections with random phase from the DBR-reflector ends. [Even though the guided field is relatively small at the DBR ends, random-phase reflections can propagate through the mostly bleached DBR reflectors (i.e. the backgorund absorption coefficient is only ~15 cm^{-1} when considering a bulk absorption coefficient of 200 cm^{-1} [6]) and affect lasing in the DFB region.]

In addition to optimizing 2-D surface emitter for high-power operation, a significant effort should be undertaken to reduce the metal loss due the inclusion of Ti and/or Pt in the p-side metalization. To eliminate the adhesion problem on the SiO_2 but still having a good ohmic contact, when only Au is being used, on the p-side metal for the pump (DFB) region, two-step p-metal deposition is the best alternative. This method is achieved by depositing conventional (200-Ti/200-Pt/2000-Au) on the whole region and followed by metal lift-off on the pumped (i.e.

DFB) region. Fig 7.2 shows the cross section of 2-D surface emitter after the metal lift-off and just before the Au deposition (in the longitudinal direction). Then Au deposition is performed on the active (DFB) region.

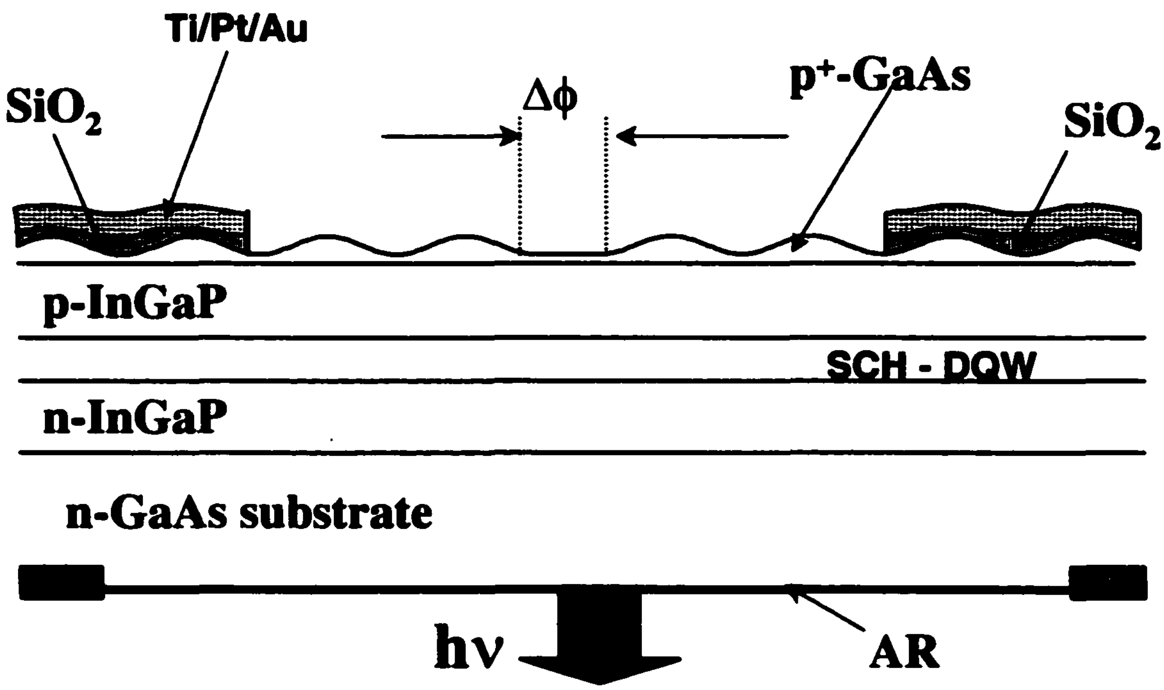

Fig. 7.2 the cross section of 2-D surface emitter just before the Au deposition on the p-side

The relatively easy of fabrication associated with these devices, together with their potential for high-output powers, opens a wide variety of exciting possibilities for many applications.

Chapter 7 References

[1] G. Witjaksono and D. Botez, "Surface-Emitting, Single-Lobe Operation from 2nd-Order Distributed-Reflector Lasers with Central Grating Phaseshift," *Appl. Phys. Lett.*, **78**, 4088-4090 (2001)

[2] G. Witjaksono, S. Li, and D. Botez, "High-efficiency, Single-lobe Surface-Emitting DFB/DBR Lasers", Paper TuA3 at the 14th IEEE LEOS Annual Meeting, 12-15 Nov. 2001, San Diego, CA.

[3] G. Witjaksono, S. Li, and D. Botez , "Single-lobe, Orthonormal-Beam Surface Emission from 2nd-order DFB/DBR Lasers with Half-Wave Grating Phaseshift", submitted to IEEE 18th ISLC 2002.

[4] Melles Griot Product Catalog, Section 15, Page 8.

[5] L. J. Mawst, D. Botez, M. Jansen, C. Zmudzinski, S. Ou, M. Sergant, C. Tu, T. J. Roth, G. Peterson, M. Valley and J. J. Yang, "2-D Coherent Surface-Emitting Leaky-Wave Coupled Laser Arrays," *IEEE J. Quantum Electron.*, **29**, 1906-1917 (1993).

[6] M. Hagberg, N. Eriksson, and A. Larsson, "Investigation of high-efficiency surface-emitting lasers with blazed grating outcouplers," *IEEE J. Quantum Electron.* **32** (9), 1596-1605 (1996).

Appendix A

Procedure of Patterning Grating with Central π-Phaseshift

This appendix describes the fabrication of the π-phaseshift 2^{nd}-order DFB surface emitter.

1) The laser base grown for this device has a p^+-GaAs-cap layer with the thickness of 1000 Å .

2) The first step is to deposit the Si_3N_4 on the top of the laser base at the thickness around 300 Å. The recipe for the PECVD deposition is given below:

   N_2 = 21%

   SiH_4 under N_2 = 50%

   NH_3 (5%) = 80%

   Pressure = 850 mTorr

   RF power is 20 W (4%).

   Time = 1.5 minutes.

   The deposition rate is around 150 - 180 Å.

3) The base is then spin-coated with HMDS at the speed of:

   Starts from 2000rpm and increased by 1000rpm every 10 seconds until it reaches 5000 rpm. Then at that highest speed, leave it for 30 seconds in order to get about 1 atomic monolayer of HMDS on the top of Si_3N_4.

4) Next step is to spin the HMDS-coated laser base with dilute at a speed of 4000 rpm for 30 seconds. It is recommended that the whole laser base be used at this stage. The dilute AZ5206 is a mixture of 1 part pure AZ5206 and 1 part of AZ1500 thinner.

5) The approximate thickness of this photoresist is around 850-1000 Å. Prebake the base with the hot plate for 1 minute at 127°C.

6) The sample now is ready to be exposed by holographics system. First the period of the grating need to be determined. Optics adjustment need to be performed to get the desired period.

7) To get V-groove grating shape, the sample need to be aligned such away that the grating lines are perpendicular to cigar/crystal direction (Fig. 1b).

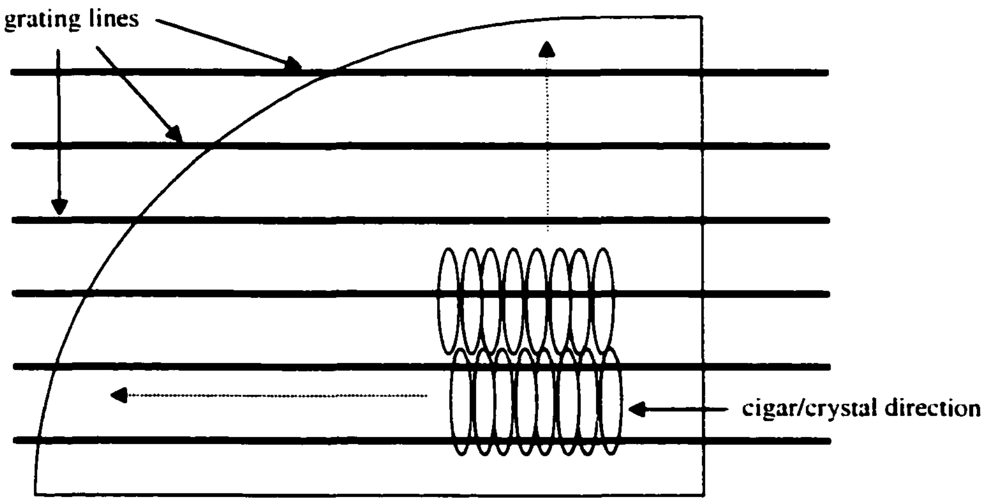

8) The base at this point is cut into 4 quarter-wafers. The reason for cutting the wafer so that the base can be aligned perpendicular to crystal orientation (cigar direction) before the holographic exposure.The holographic system is then used to expose the PR-coated base to pattern the grating. The power of laser is around 130mW to get about 0.20 – 0.24 mW across the surface of the laser base. The exposure time is 120 seconds.

9) As soon as the bases being exposed, they are needed to be placed in the thermal evaporator for about 3 to 4 hours to reach base pressure around 2.10^{-6} Torr. The amount of the Germanium ball placed on the tungsten filament is no more than 0.3 gr. It is a requirement that all the exposed bases do not get exposed to any luminescence (room light or sun rays form window) during and after this stage until the bases are ready to develop.

10) Once the vacuum reaches base pressure, the power on the evaporator is turned on and then is increased slowly to heat up the tungsten filament. The desired Ge-deposition thickness is around 45 – 60 nm. This thickness can be obtained by carefully adjust the current and the duration time. Below is one of the recipe to get that particular thickness:

Current, mA	Time, s
120	30
130	30
140	20
150	20
160	30
170	15
120	30

11) At the end of the last 30-sec, the shutter is closed and the current is decreased slowly. Wait until 15 minutes before the bases are taken out from the chamber.

12) The color of the Ge-coated base is metallic silver looking normal the base and goldish yellow looking with 45° angle.

13) Spin the Ge-coating based with AZ-5206 at the spinner speed of 4000 rpm for 30 seconds.

14) Prebake the bases on the hot plate with PR-coated side down for 1 minute at 100°C.

15) With a new aligner (MJB-3) and Mask 1 (phaseshift mask), exposed the samples for 8 seconds.

16) Develop the sample with MF327 for 1 minute and rinse it with DI water. Check with microscope to make sure that the photoresist is developed well. Postbake is might not needed at this point.

17) Flood exposure the base with a new aligner for 16 seconds.

18) Etch the Ge with H_2O_2:H_2O = 2:1 for around 2 minutes (The developed time is varied with the Ge thickness, it is important that the change of color on photoresist is observed during this process to make sure that it does not underdevelop or overdeveloped) and then rinse it with DI water for 1 minute.

19) Spray developed the holographic-exposed PR at a pressure of 7.5 psi and a speed of 500 rpm for about 15 seconds (the exact time depends on the exposure time and grating-exposure power level) . The time is very critical here and it determines the successful of grating transfer to GaAs later.

20) At this point, the base now has grating on the half of the region and Ge coating on the other half. The Ge coating has to be clean from any remaining photoresist.

21) Deactivate the grating photoresist by flood exposed the base for 3 seconds with the new aligner.

22) To harden even more the grating photoresist, the base is then immersed in the Chlorobenzene for 15 minutes and then air dry for 5 minutes.

23) Strip the remaining Ge coating with H_2O_2:H_2O = 2:1 for around 2 minutes.

24) Complete deactivation of the positive PR by post bake the base on the hot plate at 127°C for 2 minutes.

25) Flood exposure the base for 4 seconds with new aligner to pattern the negative photoresist.

26) Spray developed the negative-grating PR at pressure 7.5 psi and speed 500 rpm for about 9 seconds.

27) At this point the (photoresist) grating has fully developed on the surface of the laser base with positive grating on the half of the region and negative grating on the half of the region. The dark blue color on part of the grating (if any) indicates a thinner PR thickness on that region. This color will be used as a reference to determine the time needed to etch Si_3N_4

28) Reactive ion etching (RIE) PECVD is used to transfer the grating from the photoresist to Si_3N_4. The recipe is given below:

    $CF_4 : O_2$ = 20 sccm : 2 sccm.

    RIE mode

    Time: 2 minutes (approximate)

    Power: 150 W (incident) and 3 W (reflected).

    The reflected power need to keep below 5 W during plasma etch. The color of the discharging gas is cloudy purple. It is very critical to observe the color of the grating after this plasma etch. Be cautious that during this process the photoresist is also being etched off, consequently Si_3N_4 will be striped away if careful observation is not performed. Half way of the etch time (1 minute), the sample need to be rotated 180° to get uniform etch.

    Other way to etch SiN is using new PECVD. The recipe is:

NF_3 = 10 sccm (5%)

Pressure = 30 mTorr

RF1 power = 100 W (20%)

Etching time: 1 minute.

Etching rate is about 670A/minute.

Discharging gas color is pink.

The same as using old PECVD, the sample need to be rotated 180o half way into the etching time

29) The remaining PR is cleaned by PR stripper (AZ4110 stripper). It is not recommended that acetone be used to strip the PR because acetone will not be able to fully clean the surface.

30) At this point, the grating should look uniform all across the surface, which indicates that the grating is successfully being transferred to Si_3N_4, otherwise all steps which have been must be repeated again.

31) Lastly, transfer the grating to the GaAs-cap using $NH_4OH : H_2O_2 : H_20 = 3 : 1 : 50$ for about 25 seconds.

APPENDIX B

Procedure of Fabricating Single-Element (Ridge-guide) SEDFB Lasers

This appendix describes the fabrication of the single-element (ridge-guide) surface emitter.

1) The laser base, which is going to be used for this device, has been patterned with π-phaseshifted 2^{nd}-order DFB (see appendix A).
2) The first step is to deposit SiO_2 for 1000 Å with new PECVD on the top of GaAs-grating to protect the surface of the grating for later processing. The recipe is given below:

   Circulator temperature = 60°C

   Chamber temperature = 250°C

   N_2O= 40.5%

   SiH_4 under N_2 = 44%

   Pressure = 900 mTorr

   RF power is 30 W (6%).

   Time = 1 minute and 41 seconds
3) This laser base is then spinned first with HMDS at speed of:

   Starts at 2000 rpm and increased to 1000 rpm every 10 seconds until it reaches 5000 rpm. Then at that highest speed, leave it for 30 seconds in order to get about 1 atomic monolayer of HMDS at the top of SiO_2.
4) On the top of HMDS, PR1827 is spinned at the speed of 4000 rpm for 30 seconds.
5) Prebake the base in the oven for 30 minutes at 90°C.

6) Using the new aligner (MJB-3) and Mask 2 (ridge), exposed the photoresist for 2 minutes and 30 seconds and developed for 5 minutes.

7) Etch SiO_2 with BOE (20 : 1 = Ammonium Fluoride: HF (49%)) for 75 seconds.

8) Next steps are etching the semiconductor layers to form the ridge waveguide. First, etch the GaAs-cap (1000 Å) with $NH_4OH : H_2O_2 : H_2O = 3 : 1 : 50$ at room temperature (RT) for 18 seconds. The etching rate is about 5000 Å/minute.

9) Etch the InGaP (2000 Å) cladding layer with pure HCl at RT for 18 seconds. The etching rate is about 150 Å /second. Now the ridge structure after this step is shown below:

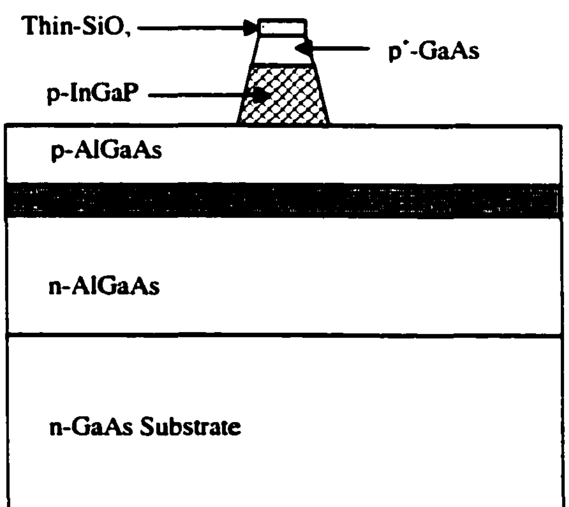

10) Without stripping the photoresist, deposit SiO_2 with new PECVD with the same recipe as step 2) but double the deposition time (3 minutes 22 seconds) to get 2000 Å -thickness of SiO_2.

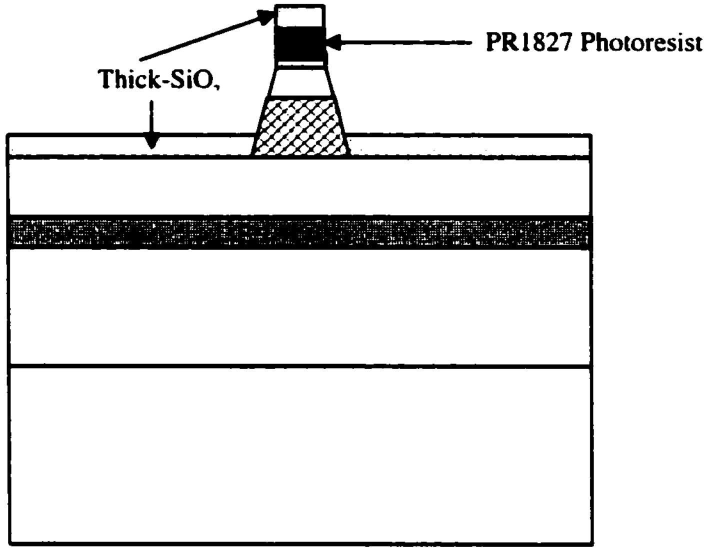

11) Next step is SiO_2 lift-off using ultrasonic bath for 1 minute. The base is immersed in the acetone during this process. Later the SiO_2 is gently wiped with acetone-wet Q-tip. The base is inspected with microscope to make sure that all metals are being lifted-off completely.

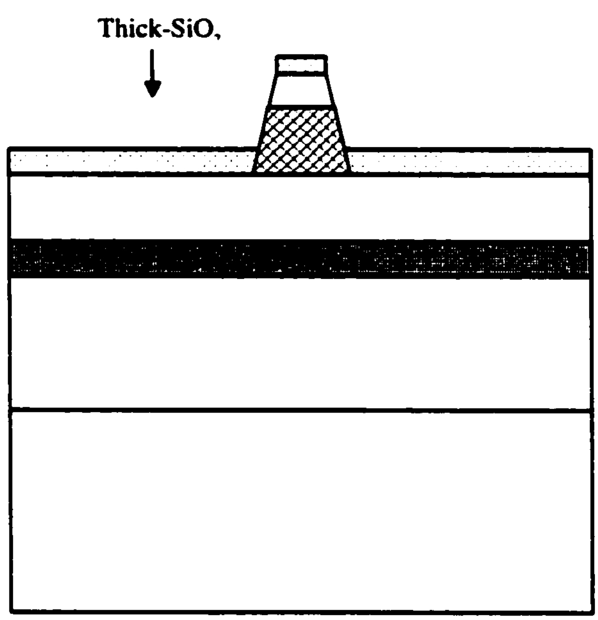

12) Thin the substrate using lapping machine to get about 160 – 180mm. Use 9μm- and then 3μm-abrasive for the last 50μm.

13) Clean the sample thoroughly for any remaining powder. The lapping JIG, the base and the rotating arm have to be cleaned as well. Any powder left on the samples and/or on the lapping machine will scratch the surface during polishing process.

14) Replace the lapping disc with polishing disc (diamond-impregnated carbon plate) and prepare the polishing solution.

15) Polish the substrate to get smooth surface by using polishing machine with polished powder. Observe with microscope to check the flatness of the surface every 5 minutes. It takes about 2 x 5 minutes to get fairly uniform surface.

16) Clean the samples from any residue from the polishing step using acetone, methanol and DI water. Air dry the samples after that. Make sure the polished surface is clean and smooth.

17) Stick the thinned (~ 150 μm) wafer on the thicker base (370 μm) for later processing. Wax need to be put thin enough so it will not spill on the base surface of the thin wafer but strong enough to make the bonding.

18) This laser base is then spinned with PR1827 at the speed of 4000 rpm for 30 seconds.

19) Prebake the base in the oven for 30 minutes at 90°C.

20) Using the new aligner (MJB-3) and Mask 3 (n-side opening), exposed the photoresist for 2 minutes and 30 seconds and developed for 5 minutes.

21) Check with a microscope to make sure that the developing time is complete and the area without PR is cleaned.

22) Without postbake, put the base in the e-beam evaporator chamber to deposit n-metal. The metal used are: Ge :: AuGe :: Ni :: Au = 200 Å :: 1000 Å :: 300 Å :: 2500 Å.

23) As soon as the samples have been taken out from the e-beam evaporator, put them in the PR stripper (1165 stripper) until the PR on the lift-off area has been moved up. Then placed the beaker with the samples in it inside the ultrasonic bath for 1 minute. Leave the samples in the 1165 for overnight to get good lift-off.

24) Detach the thin samples with the thick base by heated up the base and clean the samples from wax and any residue with acetone, methanol and DI water for 5 minutes each.

25) Anneal the sample for 100°C (for 1 minutes) and continue to 375°C (for 30 seconds). Make sure that the base was placed flat on the top of the hot plate in the annealing chamber so the thin wafer will get heated up uniformly.

26) Spin the thin wafer with photoresist (PR 1827) at speed of 4000 rpm for 30 seconds.

27) Prebake for 30 minutes at 90°C in the chamber.

28) Using Mask 4 (AR mask), expose the thin wafer for 2 minutes and 30 seconds using new aligner.

29) Develop the photoresist with MF321 for 5 minute.

30) Check with a microscope to make sure that the developing time is complete and the area without PR is cleaned.

31) Without postbake, put the base in the dielectric e-beam evaporator chamber to deposit AR-coating on the n-side. Pump the chamber down to get base pressure less than 2 x 10^{-6} Torr.

32) Once the base pressure is reached, heat up the samples to 200° C. The dielectrics used are Al_2O_3 :: Si :: Al_2O_3 = 180 Å :: 270 Å :: 1500 Å. Leave them cool down before the samples are taken out from the chamber.

33) As soon as the samples have been taken out from the dielectric e-beam evaporator, put them in the warm PR stripper (1165 stripper) until the PR on the lift-off area has been moved up. Then placed the beaker with the samples in it inside the ultrasonic bath for 1 minute.

34) Spin the thin wafer with photoresist (AZ5206) at speed of 4000 rpm for 30 seconds.

35) Prebake for 1 minutes on the hot plate at 105°C.

36) Using Mask 5 (contact opening), expose the thin wafer for 8 seconds using new aligner.

37) Develop the photoresist with MF327 for 45 seconds.

38) Check with a microscope to make sure that the developing time is complete and the opening are is cleaned.

39) Postbake the samples on the hot plate for 1 minutes at 105° C.

40) Etch SiO_2 with BOE for 75 seconds.

41) Clean the GaAs-cap with H_20 : H_2O_2 : NH_4OH = 485ml : 3.5ml : 8.5ml for 2 seconds.

42) Put back the thin wafer to the e-beam chamber for p-metal deposition. The gold will stick well to the GaAs and alloyed p-metal but not on the SiO_2. The metal used are: Ti :: Au :: Ti :: Pt :: Au = 40 Å :: 1000 Å :: 200 Å :: 200 Å :: 2500 Å.

43) Now samples are ready to be cut into bars. By using the scribber, cut the samples at the end of DBR.

44) Both facets are now ready to be coated. Use procedure 33) and 34) for each facets. Precaution need to be done during device mounting on the clipper so the sample facet is positioned correctly. The heater is needed to be checked that it works fine before the pump down continue.

Appendix C

Modeling Program of Distributed Feedback Reflector with Central Phaseshift

FINAL VERSION developed by Gunawan Witjaksono, which corrects all the errors from previous version and includes index depression and detuning into the consideration.

INPUT PARAMETERS:

Wave length $\lambda := 980 \cdot 10^{-7}$

Grating Period $\Lambda := \frac{980}{3.27} \cdot 10^{-7}$

Grating order $m := 2$

DFB length on the left side $L1 := 835 \cdot \Lambda$ $L1 = 0.02502$

DFB length on the right side $L2 := 835 \cdot \Lambda$ $L2 = 0.02502$

DBR length on the left side $l1 := 1669 \cdot \Lambda$ $l1 = 0.05002$

DFB length on the right side $l2 := l1$

COEFFICIENTS

Imaginary number $i := \sqrt{-1}$

wave vector $ko := 2 \cdot \frac{\pi}{\lambda}$

Propagation constant $\beta o := m \cdot \frac{\pi}{\Lambda}$

DEVICE PARAMETERS

DFB region: Coupling coefficient $\kappa_1 := -5.47 + 49.42 \cdot i$ $\kappa_3 := \kappa_1$

Correction factor $\zeta := 36.43 + 50.28 \cdot i$

Index depression due to current injection: $\delta dp := 36$

DFB region: Coupling coefficient $\kappa_2 := 2.75 + 30.46 \cdot i$ $\kappa_4 := \kappa_2$

Correction factor $\zeta d := -37.98 + 31.19 \cdot i$

Detuning due to index depression: $\alpha d := -15$

Detuning due background loss: $\delta b := 20$

Facet Reflection Coefficients: Left side $r_{AR} := 0$ Right side $r_{HR} := r_{AR}$

$R_{AR} := r_{AR}^{2}$ $R_{AR} = 0$ $R_{HR} := r_{HR}^{2}$ $R_{HR} = 0$

Phase Shifts Between Regions: Left phaseshift $\Phi_{AR} := \frac{0 \cdot \pi}{180}$ Right phaseshift $\Phi_{HR} := \frac{0 \cdot \pi}{180}$

Center phaseshift $\theta := \frac{\pi \cdot 180}{180}$

EQUATIONS :

$$\gamma(\kappa, \alpha o, \delta) := \sqrt{\kappa^{2} + (\alpha o - i \cdot \delta)^{2}}$$

MATRIX EQUATIONS:

Reflection

$$\mathrm{Fr}(r) := \begin{pmatrix} \frac{1}{1-r} & \frac{-r}{1-r} \\ \frac{-r}{1-r} & \frac{1}{1-r} \end{pmatrix} \qquad \mathrm{Fr}_{AR} := \mathrm{Fr}(r_{AR}) \qquad \mathrm{Fr}_{HR} := \mathrm{Fr}(r_{HR})$$

Phase shift

$$\mathrm{Fp}(\phi) := \begin{pmatrix} e^{-i\cdot\phi} & 0 \\ 0 & e^{i\cdot\phi} \end{pmatrix} \qquad \mathrm{Fp}_{AR} := \mathrm{Fp}(\phi_{AR}) \qquad \mathrm{Fp}_{HR} := \mathrm{Fp}(\phi_{HR})$$

Traveling waves:

$$\mathrm{Fdfb}(\kappa,\alpha o,\delta,L) := \begin{pmatrix} \cosh(\gamma(\kappa,\alpha o,\delta)\cdot L) + \frac{\alpha o - i\cdot\delta}{\gamma(\kappa,\alpha o,\delta)}\cdot\sinh(\gamma(\kappa,\alpha o,\delta)\cdot L) & \frac{-i\cdot\kappa}{\gamma(\kappa,\alpha o,\delta)}\cdot\sinh(\gamma(\kappa,\alpha o,\delta)\cdot L) \\ \frac{i\cdot\kappa}{\gamma(\kappa,\alpha o,\delta)}\cdot\sinh(\gamma(\kappa,\alpha o,\delta)\cdot L) & \cosh(\gamma(\kappa,\alpha o,\delta)\cdot L) - \frac{\alpha o - i\cdot\delta}{\gamma(\kappa,\alpha o,\delta)}\cdot\sinh(\gamma(\kappa,\alpha o,\delta)\cdot L) \end{pmatrix}$$

TRANSFER MATRIX FORMULATION:

$$F(\alpha_0,\delta) = Fr_{HR}Fp_{HR}F_{dfb}(\kappa_4,-\mathrm{Im}(\zeta_d)+\alpha_d,\mathrm{Re}(\zeta_d)+\delta+\delta_b,l_2)F_{dfb}(\kappa_3,-\mathrm{Im}(\zeta),\alpha_o,\mathrm{Re}(\zeta)+\delta-\delta_{dp},L_2)\cdot$$
$$Fp(\theta)F_{dfb}(\kappa_1,-\mathrm{Im}(\zeta),\alpha_o,\mathrm{Re}(\zeta)+\delta-\delta_{dp},L_1)F_{dfb}(\kappa_2,-\mathrm{Im}(\zeta_d)+\alpha_d,\mathrm{Re}(\zeta_d)+\delta+\delta_b,l_1)Fp_{AR}Fr_{AR}$$

LENGTH

DFB length $\quad L := L1 + L2 \qquad L = 0.05$

Total DBR length $\quad l := l1 + l2 \qquad l = 0.1$

Total grating length $\quad Ll := L + l \qquad Ll = 0.15$

CALCULATING AND PLOTING DFB MODES:

Define the plot region

$\mathrm{nmax} := 100 \qquad \mathrm{pmax} := 100 \qquad n\frac{8}{\mathrm{nmax}}$

$n := 0..\,\mathrm{nmax} \qquad p := 0..\,\mathrm{pmax}$

$$\alpha oL_n := \left(n\frac{10}{\mathrm{nmax}}\right) - 0 \qquad \delta L_p := p\frac{80}{\mathrm{pmax}} - 40$$

Solve for the modes:

$$A_{p,n} := \left(F\left(\frac{\alpha oL_n}{L},\frac{\delta L_p}{Ll}\right)_{1,1}\right)^{-1}$$

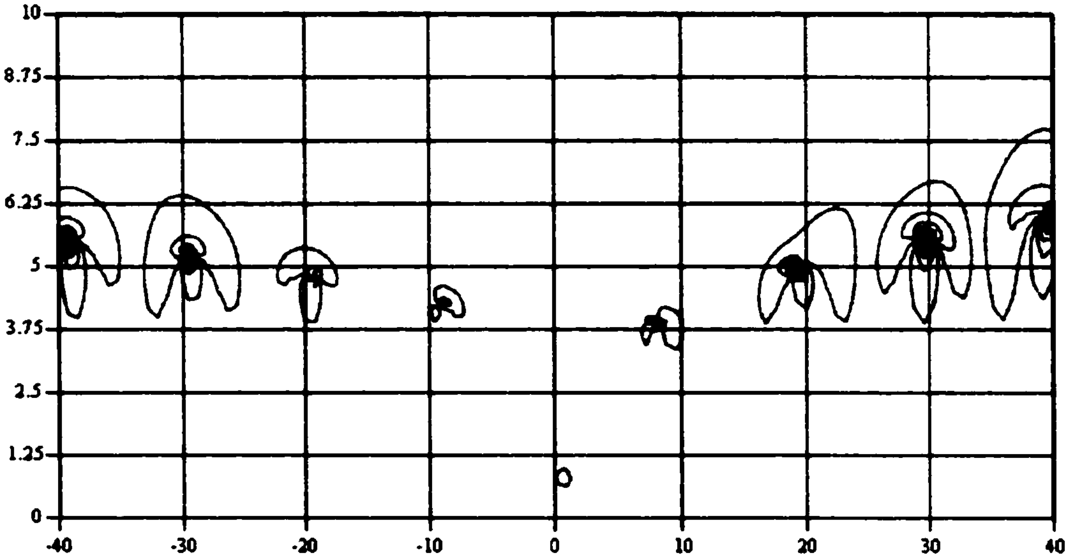

A

Mode solution

$\mathrm{oscmag}(\alpha o,\delta) := \left|F(\alpha o,\delta)_{1,1}\right|$ $\quad$ $\mathrm{oscphase}(\alpha o,\delta) := \arg\left(F(\alpha o,\delta)_{1,1}\right)$

$m := 0$

Guesses: $\alpha o := \frac{1}{L}$ $\quad$ $\delta := \frac{0}{Ll}$

Given $\quad \mathrm{oscmag}(\alpha o,\delta) = 0 \quad \mathrm{oscphase}(\alpha o,\delta) = m\cdot 2\cdot\pi \quad \begin{pmatrix}\alpha o\\ \delta\end{pmatrix} := \mathrm{Find}(\alpha o,\delta)$

Carrier absoprtion loss $\quad \alpha fc := 3$

Edge loss $\quad \alpha e := 0$

Field Loss $\quad \alpha o\cdot L = 0.74 \quad \alpha o = 14.795$

$L = 0.05$

Mode Deviation $\quad \delta\cdot Ll = 1.045 \quad \delta = 6.962$

$\kappa_1\cdot L = -0.274 + 2.473i$

Threshold gain: $\quad gt := 2\cdot\alpha o + \alpha fc + \alpha e$

$gt = 32.59$

Intensity Loss $\quad \alpha dfb := 2\cdot\alpha o \quad \alpha dfb = 29.59$

Wavelength Deviation $\quad \beta := \beta o + \delta \quad \beta = 2.097\times 10^{5}$

$neff := \frac{\beta}{ko} \quad neff = 3.27$

$\Delta\lambda := \frac{neff\cdot 2\cdot\pi}{\beta} - \frac{neff\cdot 2\cdot\pi}{\beta o} \quad \Delta\lambda = -3.254\times 10^{-9}$

$\lambda dfb := \frac{neff\cdot 2\cdot\pi}{\beta} \quad \lambda dfb = 9.8\times 10^{-5}$

Fabry-Perot Mirror Loss

$r := e^{-\alpha_o \cdot L}$ $r = 0.477$ $r^2 = 0.227$

$\frac{1}{L} \cdot \ln\left(\frac{1}{r_{AR} \cdot r_{HR}}\right) = ■$

RADIATION LOSSES:

DFB region: $\alpha surf := 97.69$

DBR region: $\alpha surd := 59.57$

Longitudinal Field Profile

$\delta d := (-\delta - \mathrm{Im}(i \cdot \zeta d)) - 1$

Parameters

$g1 := \mathrm{Re}(1 \cdot \alpha o - i \cdot \zeta)$ $\delta 1 := (-\delta - \mathrm{Im}(i \cdot \zeta)) - 1$ $gd := \mathrm{Re}(\alpha o - i \cdot \zeta d)$

$\alpha o = 14.795$ $\delta = 6.962$

$g1 = 65.075$ $\delta 1 = 43.392$

CALCULATING THE NEAR-FIELD PROFILE:

Boundary Conditions

$Sar := 1 + i \cdot 1$ $So := Sar \cdot e^{i \cdot \Phi_{AR}}$ $\alpha oo := \alpha d - \mathrm{Im}(\zeta d)$

$Rar := r_{AR} \cdot Sar$ $Ro := Rar \cdot e^{-i \cdot \Phi_{AR}}$ $\delta 0 := \delta + \delta b + \mathrm{Re}(\zeta d) \cdot 1$

Solutions to Coupled-Mode Equations on the grating region:

DBR region 1:

$\gamma 4 := \gamma(\kappa_4, \alpha oo, \delta 0)$ $s := \pi \frac{180}{180}$

$$R1(z) := \left(\cosh(\gamma 4 \cdot z) + \frac{\alpha oo - i \cdot \delta 0}{\gamma 4} \cdot \sinh(\gamma 4 \cdot z)\right) \cdot Rar + \frac{-i \cdot \kappa_4}{-\gamma 4} \cdot \sinh(\gamma 4 \cdot z) \cdot Sar$$

$$S1(z) := \frac{-i \cdot \kappa_4}{\gamma 4} \cdot \sinh(\gamma 4 \cdot z) \cdot Rar + \left(\cosh(\gamma 4 \cdot z) - \frac{\alpha oo - i \cdot \delta 0}{\gamma 4} \cdot \sinh(\gamma 4 \cdot z)\right) \cdot Sar$$

DFB region 1

$\delta := \delta + -\delta dp - 0 + \mathrm{Re}(\zeta) \cdot 1$

$Rdo := R1(l1)$ $\alpha o := \alpha o - \mathrm{Im}(\zeta)$

$Sdo := S1(l1)$ $\gamma 1 := \gamma(\kappa_1, \alpha o, \delta)$ $\alpha o = -35.485$

$$Rd(z) := \left(\cosh(\gamma 1 \cdot z) + \frac{\alpha o - i \cdot \delta}{\gamma 1} \cdot \sinh(\gamma 1 \cdot z)\right) \cdot Rdo + \frac{-i \cdot \kappa_1}{-\gamma 1} \cdot \sinh(\gamma 1 \cdot z) \cdot Sdo$$

$$Sd(z) := \frac{-i \cdot \kappa_1}{\gamma 1} \cdot \sinh(\gamma 1 \cdot z) \cdot Rdo + \left(\cosh(\gamma 1 \cdot z) - \frac{\alpha o - i \cdot \delta}{\gamma 1} \cdot \sinh(\gamma 1 \cdot z)\right) \cdot Sdo$$

DFB region 2

$Rm := Rd(L1) \cdot e^{-i \cdot \theta}$ $Rmp := R1(L1 + l1) \cdot e^{i \cdot \frac{\theta}{2}}$

$Sm := Sd(L1) \cdot e^{i \cdot \theta}$ $ur := e^{-i \cdot \theta}$ $us := e^{i \cdot \theta}$ $Smp := S1(L1 + l1) \cdot e^{i \cdot \frac{\theta}{2}}$

$$\gamma 3 := \gamma(\kappa_3, \alpha o, \delta)$$

$$S2(z) := q\left[\left(\cosh(\gamma 3 \cdot z) + \frac{\alpha o - i\cdot\delta}{-\gamma 3}\cdot\sinh(\gamma 3\cdot z)\right)\cdot Sm\cdot u + \frac{-i\cdot\kappa_3}{\gamma 3}\cdot\sinh(\gamma 3\cdot z)\cdot Rm\cdot u\right]$$

$$R2(z) := \left[\frac{-i\cdot\kappa_3}{-\gamma 3}\cdot\sinh(\gamma 3\cdot z)\cdot Sm + \left(1\cdot\cosh(\gamma 3\cdot z) + \frac{\alpha o - i\cdot\delta}{\gamma 3}\cdot\sinh(\gamma 3\cdot z)\cdot 1\right)\cdot Rm\right]$$

DBR region 2:

$$Rdm := R2(L2)$$

$$Sdm := S2(L2) \qquad \gamma 30 := \gamma(\kappa_2, \alpha oo, \delta 0)$$

$$Rd2(z) := u\left[\left(\cosh(\gamma 30\cdot z) + \frac{\alpha oo - i\cdot\delta 0}{-\gamma 30}\cdot\sinh(\gamma 30\cdot z)\right)\cdot Rdm + \frac{-i\cdot\kappa_2}{\gamma 30}\cdot\sinh(\gamma 30\cdot z)\cdot Sdm\right]$$

$$Sd2(z) := u\left[\frac{-i\cdot\kappa_2}{-\gamma 30}\cdot\sinh(\gamma 30\cdot z)\cdot Rdm + \left(\cosh(\gamma 30\cdot z) - \frac{\alpha oo - i\cdot\delta 0}{-\gamma 30}\cdot\sinh(\gamma 30\cdot z)\right)\cdot Sdm\right]$$

Verify the values (used to correct any problems

$\gamma 4 = 35.184 - 12.084i$

$\gamma 1 = 0.231 - 34.755i$

$\gamma 3 = 0.231 - 34.755i$

$\gamma 30 = 35.184 - 12.084i$

$R1(L1) = -0.993 - 0.695i$

$S1(L1) = 3.327 + 1.898i$

$Rm = 9.426 + 2.72i$

$Sm = -9.426 - 2.72i$

$Smm = \blacksquare$

$\delta 0 = -11.018$

Define the calculated region

$$z\theta := \theta\cdot\frac{180}{\pi}\cdot\frac{\Lambda}{360} \qquad z\theta = 1.498\times 10^{-5}$$

$$L := L1 + L2 + l1 + l2 + z\theta$$

$$Lz := L1 + L2 + l1 + z\theta$$

$$z\theta 2 := \frac{z\theta}{2}$$

Perform the calculation of the near field and guided field:

Left-going field of the guided field:

$$Sg(z) := \begin{cases} S1(z) & \text{if } z \le l1 \\ Sd(z - l1) & \text{if } l1 < z \le (L1 + l1) \\ Smp & \text{if } (L1 + l1) < z \le (L1 + l1 + z\theta 2) \\ Smp & \text{if } (L1 + l1 + z\theta 2) < z \le (L1 + l1 + z\theta) \\ S2[z - (L1 + l1 + z\theta)] & \text{if } (L1 + l1 + z\theta) < z \le [L1 + (l1 + z\theta) + L2] \\ Sd2[(L1 + L2 + l1) - z] & \text{otherwise} \end{cases}$$

Right-going field of the guided field:

$$Rg(z) := \begin{cases} R1(z) & \text{if } z \le l1 \\ Rd(z - l1) & \text{if } l1 < z \le (L1 + l1) \\ Rmp & \text{if } (L1 + l1) < z \le (L1 + l1 + z\theta2) \\ Rmp & \text{if } (L1 + l1 + z\theta2) < z \le (L1 + l1 + z\theta) \\ R2[z - (L1 + l1 + z\theta)] & \text{if } (L1 + l1 + z\theta) < z \le [L1 + (l1 + z\theta) + L2] \\ Rd2[(L1 + L2 + l1) + -z] & \text{otherwise} \end{cases}$$

Left-going field of the near field:

$$Sn(z) := \begin{cases} \left(\sqrt{\alpha surd}\cdot S1(z)\right) & \text{if } z < l1 \\ \left(\sqrt{\alpha surf}\cdot Sd(z - l1)\right) & \text{if } l1 \le z \le (L1 + l1) \\ \left[\sqrt{\alpha surf} S2[z - (L1 + l1)]\right] & \text{if } L1 + l1 < z < L1 + (l1) + L2 \\ \left[\sqrt{\alpha surd}\cdot Sd2[(L1 + L2 + l1) - z]\right] & \text{otherwise} \end{cases}$$

Right-going field of the near field:

$$Rn(z) := \begin{cases} \left(\sqrt{\alpha surd}\cdot R1(z)\right) & \text{if } z < l1 \\ \left(\sqrt{\alpha surf}\cdot Rd(z - l1)\right) & \text{if } l1 < z \le (L1 + l1) \\ \left[\sqrt{\alpha surf}\cdot R2[z - (L1 + l1)]\right] & \text{if } L1 + l1 < z < L1 + l1 + L2 \\ \left[\sqrt{\alpha surd}\cdot Rd2[(L1 + L2 + l1) + -z]\right] & \text{otherwise} \end{cases}$$

PLOTING THE NEAR-FIELD PROFILES:

Electric Field Equation

$$E1(z) := R1(z)\cdot e^{-i\cdot\beta_o\cdot z} + S1(z)\cdot e^{i\cdot\beta_o\cdot z}$$

$a := 0$ $b := L$

$z := a, a + .001 .. b$

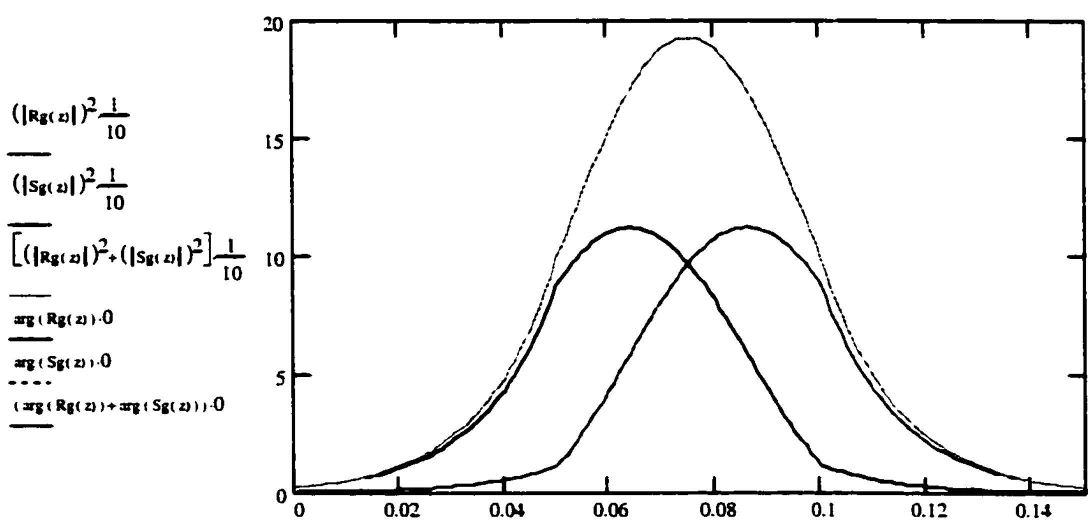

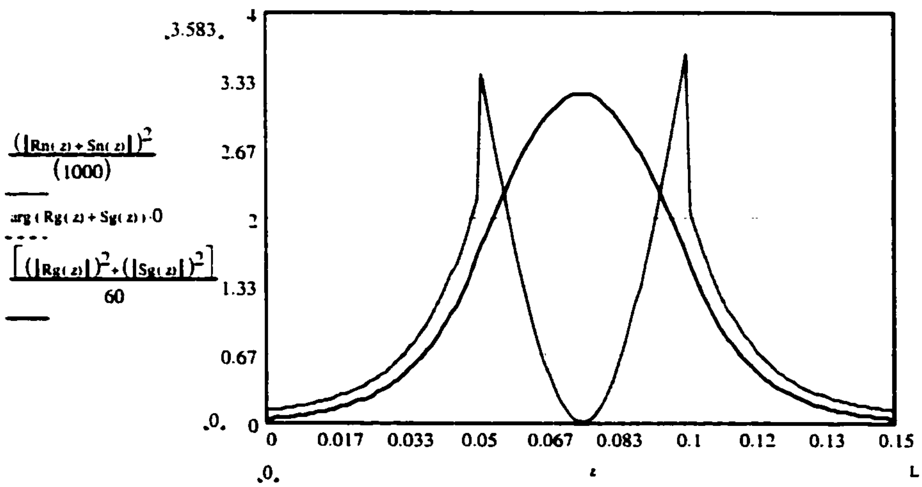

Calculating the uniformity of the near field:

$l1 = 0.05$

Point of the interest $nm := 0.075$ $nm = 0.075$

$nn := l1 + L1$ $nn = 0.075$

$c := l1$ $c = 0.05$

Near-field Uniformity $rh := \frac{[(|Rn(nm) + Sn(nm)|)^2]}{(|Rn(c) + Sn(c)|)^2}$ $(|Rn(nm) + Sn(nm)|)^2 = 0.014$

$(|Rn(c) + Sn(c)|)^2 = 2.485 \times 10^5$

$rh = 5.641 \times 10^{-8}$ $\frac{1}{rh} = 1.773 \times 10^7$

Guided-field Uniformity $rhg := \frac{[(|Rg(nn)|)^2 + (|Sg(nn)|)^2]}{(|Rg(l1)|)^2 + (|Sg(l1)|)^2}$ $(|Rg(nn)|)^2 + (|Sg(nn)|)^2 = 192.487$

$(|Rg(l1)|)^2 + (|Sg(l1)|)^2 = 98.507$

$\frac{1}{rhg} = 0.512$ $rhg = 1.954$

CALCULATE THE EFFICIENCY

Define the region:

$L := L1 + L2$ $LL := l1 + L$ $D := 10$

$LLL := LL + l2$

internal Efficiency: $ni := 1$ $ENear(z) := Rg(z) + Sg(z)$

For different coefficients between DFB and DBR

$$\frac{2\cdot ni\cdot\left|\int_0^{ll}\left[\alpha surd\left(\left|ENear(z)\right|\right)^2\right]dz\right| + ni\cdot\left|\int_{ll}^{LL}\left[\alpha surf\left(\left|ENear(z)\right|\right)^2\right]dz\right|}{\left[\left|\int_{ll}^{LL}\left(\left|Rg(z)\right|\right)^2 + \left(\left|Sg(z)\right|\right)^2 dz\right|\cdot(gt)\right]} = 0.507$$

CALCULATING THE FAR FIELD:

Calculate dan plot the far-field pattern:

$$\Psi(\theta) := \left[i\cdot\frac{\cos(\theta)}{\sqrt{1-\sin(\theta)^2}}\cdot\frac{\exp(-i\cdot ko\cdot D)}{\lambda\cdot D}\left(\left|\int_0^{LLL} ENear(z)\cdot\exp(i\cdot ko\cdot z\cdot\sin(\theta))\,dz\right|\right)\right]^2$$

$\theta := -0.01, -0.01 + 0.0001 .. 0.01$

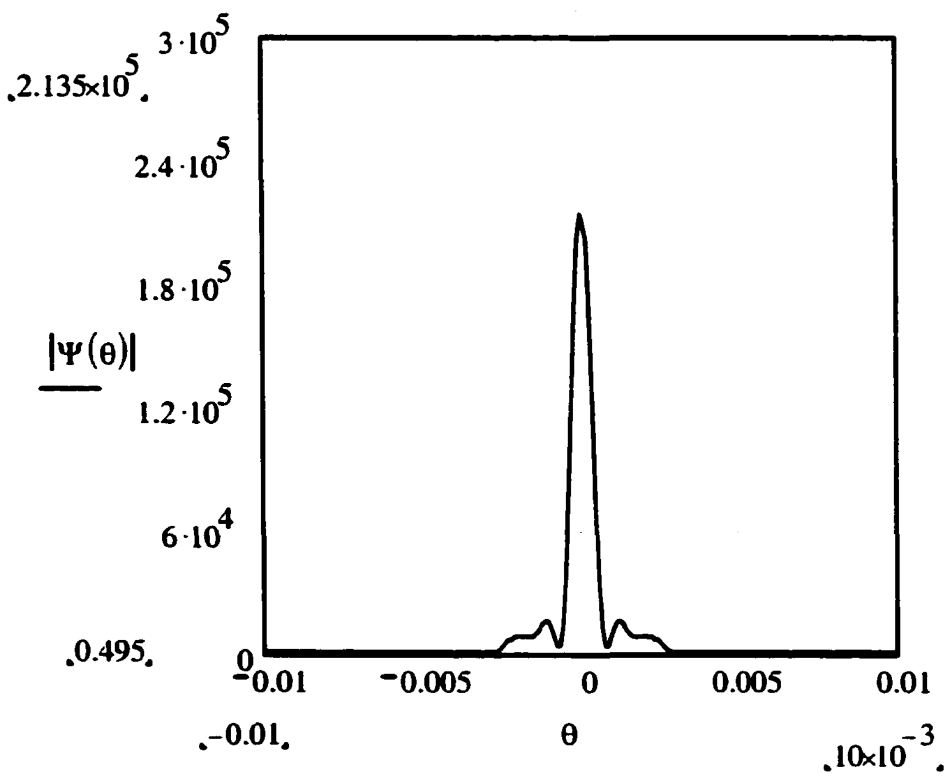

CALCULATE THE REFLECTIVITY BANDWIDTH:

$\alpha b1 := -0$

$\alpha b2 := -\mathrm{Im}(\zeta d)$

$r0 := 0 \qquad l2 := 12 \qquad \alpha b := \alpha d - 1\cdot \mathrm{Im}(\zeta d) \qquad \delta := \delta + 0$

$$rb := \frac{\left[\left[-i\cdot\kappa_2 + (\alpha b - i\cdot\delta)\cdot r0\right]\cdot\sinh\left(\gamma(\kappa_2,\alpha b,\delta)\cdot l2\right) + \gamma(\kappa_2,\alpha b,\delta)\cdot r0\cdot\cosh\left(\gamma(\kappa_2,\alpha b,\delta)\cdot l2\right)\right]}{\gamma(\kappa_2,\alpha b,\delta)\cdot\cosh\left(\gamma(\kappa_2,\alpha b,\delta)\cdot l2\right) - \left[(\alpha b - i\cdot\delta) - i\cdot\kappa_2\cdot r0\right]\cdot\sinh\left(\gamma(\kappa_2,\alpha b,\delta)\cdot l2\right)}$$

$rb = 0.343 - 0.105i$

$|rb| = 0.358 \qquad (|rb|)^2 = 0.128$

Get the plot of reflectivity bandwidth:

$\gamma(\kappa_2,\alpha o,\delta) = 22.722 + 15.231i$

$\alpha b = -46.19$

$\delta = 7.392$

$\alpha b = -46.19$

$$rb(\lambda d) := \frac{\left[\left[-i\cdot\kappa_2 + \left[\alpha b - i\left(2\cdot\pi\frac{\lambda d}{0.98\cdot 10^4\cdot\Lambda}\right)\right]\cdot r0\right]\cdot\sinh\left(\gamma\left(\kappa_2,\alpha b,2\cdot\pi\frac{\lambda d}{0.98\cdot 10^4\cdot\Lambda}\right)\cdot l2\right) + \gamma\left(\kappa_2,\alpha b,2\cdot\pi\frac{\lambda d}{0.98\cdot 10^4\cdot\Lambda}\right)\cdot r0\cdot\cosh\left(\gamma\left(\kappa_2,\alpha b,2\cdot\pi\frac{\lambda d}{0.98\cdot 10^4\cdot\Lambda}\right)\cdot l2\right)\right]}{\gamma\left(\kappa_2,\alpha b,2\cdot\pi\frac{\lambda d}{0.98\cdot 10^4\cdot\Lambda}\right)\cdot\cosh\left(\gamma\left(\kappa_2,\alpha b,2\cdot\pi\frac{\lambda d}{0.98\cdot 10^4\cdot\Lambda}\right)\cdot l2\right) - \left[\left[\alpha b - i\left(2\cdot\pi\frac{\lambda d}{0.98\cdot 10^4\cdot\Lambda}\right)\right] - i\cdot\kappa_2\cdot r0\right]\cdot\sinh\left(\gamma\left(\kappa_2,\alpha b,2\cdot\pi\frac{\lambda d}{0.98\cdot 10^4\cdot\Lambda}\right)\cdot l2\right)}$$

$gd = 45.985 \qquad \delta l = 43.392 \qquad gl = 65.075$

$$m(\lambda d) := 2\cdot\pi\frac{\lambda d}{0.98\cdot 10^{-4}\cdot\Lambda}$$

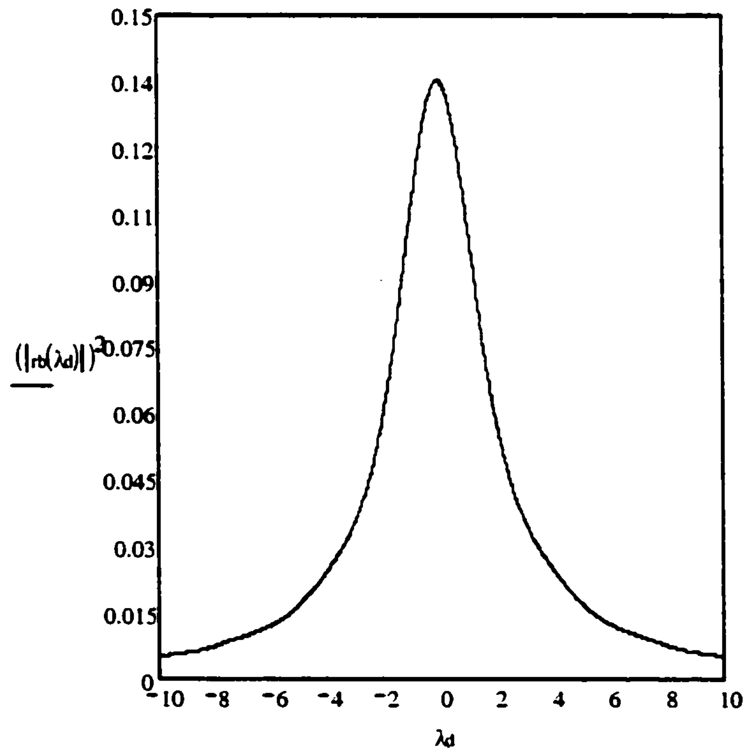

wavelength shift as a function of detuning:

$$\lambda d(\delta r) := \Lambda \cdot \left(0.98 \cdot 10^{-4} \cdot \frac{\delta r}{2 \cdot \pi}\right)$$

detuning as a function of wavelength shift:

$$\delta d(\lambda d) := 2 \cdot \pi \cdot \frac{\lambda d}{\Lambda \cdot 0.98 \cdot 10^{4}}$$

$\alpha oo = -46.19$ $Rar = 0$ $Sar = 1 + i$ $\delta 0 = -11.018$ $m(2) = 4.279 \times 10^{9}$

$\Lambda := 1.0$

$R1a(z) := (-i \cdot 1 \cdot \tanh(\gamma 4 \cdot z))$

$\delta dp = 36$

$r := \frac{Rdo}{Sdo}$

$\lambda d := -7, -7 + 0.1 .. 7$

$$\delta d(\lambda d) := 2 \cdot \pi \cdot \frac{\lambda d}{\Lambda \cdot 0.98 \cdot 10^{4}}$$

$\delta = 7.392$

$r = -0.353 - 0.058i$

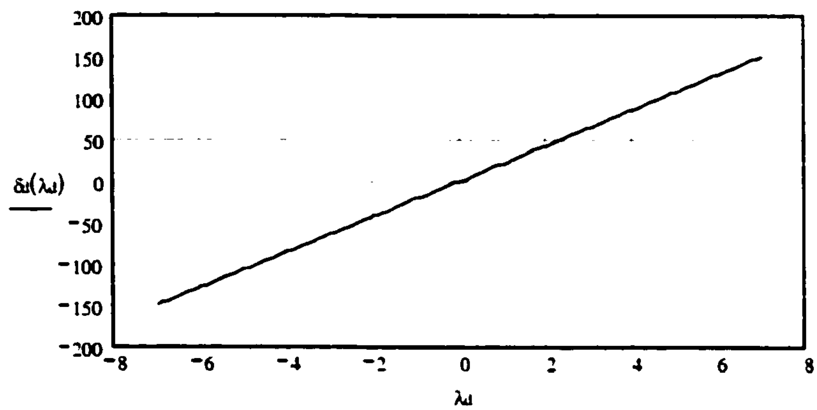

$\sqrt{\kappa_1^2 + (\alpha o - i \cdot \delta)^2} = 0.231 - 34.755i$

$\gamma 1 = 0.231 - 34.755i$

$Sd(L1) = 9.426 + 2.72i$

$Sm = -9.426 - 2.72i$

$r := \frac{Sd2(12)}{Rd2(12)}$ $r = -0.356 - 0.067i$